Turbulence Transport in High-Speed Particle-Laden Flows

by

Archana Sridhar

A dissertation submitted in partial fulfillment
of the requirements for the degree of
Doctor of Philosophy
(Aerospace Engineering and Scientific Computing)
in the University of Michigan
2025

Doctoral Committee:

Associate Professor Jesse Capecelatro, Chair
Professor Eric Johnsen
Professor Krishnan Mahesh
Professor Venkat Raman

Archana Sridhar
arsridha@umich.edu
ORCID iD: 0000-0003-2263-4963

DEDICATION

To my mom.

ACKNOWLEDGEMENTS

I would like to begin by expressing my deepest gratitude and respect to my PhD advisor, Jesse Capecelatro, who has been far more than a mentor. I feel incredibly privileged and lucky to have worked under his guidance. In moments of uncertainty and challenge, he has served as a lighthouse helping me navigate the often turbulent waters of research. I sincerely hope that I have absorbed even a fraction of the many admirable qualities he has. His encouragement and willingness to provide every resource and support have been instrumental to my growth and success. Special thanks to my committee—Dr. Venkat Raman for teaching me the basics of turbulence, Dr. Eric Johnsen for his comments and questions during presentations and practice talks, and Dr. Krishnan Mahesh for feedback and suggestions.

I would like to thank Prof. Rodney Fox for his valuable suggestions during the development and implementation of the PTKE model. I also appreciate the contributions of my collaborators at Sandia, Dr. Kyle Daniel and Dr. Justin Wagner, and at Purdue, Dr. Ryan Houim and Dr. Jacob Posey, for their efforts on particle dispersal. I am also grateful to Dr. Raymond Fontenot from CFDRC for both the initial PTKE research and more recent efforts involving scalar transport and modeling.

My mother is truly my bedrock-her support and resilience have shaped every aspect of my journey. My two wonderful sisters, Aparna and Anupama, have always motivated me to stay focused and set a positive example (nothing pushes me forward quite like being an older sibling). I would also like to acknowledge my father, whose financial support enabled me to pursue my studies here at the University of Michigan. Special thanks go to my cousin Srikanth, who stepped up to be my most respected big brother, and his wife Sarayu, and their wonderful daughter Baby D.

Heartfelt gratitude to my research group: Meet, for always lending his ears for constant research and personal rants; Sathvik, for random coffee breaks and thoughtful discussions; Rebecca, for personal advice; Ashray, for keeping things lively; Dr. Mehdi, Dr. Abhilash, Dr. Jack, and Dr. Deepak, for their immense wisdom and advice; Luc, for our conversations; Max, for his band performances; Ana, for introducing me to Brazilian culture and our newest members Jaehyeon, Ian and Niranjan.

So many others from Autolab deserve a mention: Baudouin, for supporting me leading up to this defense, as well as our One Piece discussions. Apoorva, my dear friend, for all the snacks, coffee, and mental health walks in Gallup park breaks we took together. Bjorn, for our conference hangouts; Zhiwen, for random hallway encouragement; and Parth, for your experimental anecdotes. My Aero friends from GeMA and my prelims study partner Shivank, special thanks.

There are two close friends who have stayed with me for the past six and a half years here in Michigan. I was fortunate to meet my previous roommate, Yashaswini, who has been there for me since day one and has supported me through every stage of this journey—I am truly grateful for her support. To my friend Bhargav, I truly cannot thank you enough for all the help, encouragement and food you have provided me along the way. To my previous roommate Navya, whose optimism and dedication inspired me daily, I genuinely enjoyed those early morning gym sessions together. My tennis friends Puneeth and Akash stood by me through challenging tournaments, injuries, and recovery. To my junior PhD friend Pratyush and his cohort, thank you for all those memorable nights of ping pong and barbecues. I am also grateful to the many others who have helped me become who I am today: cousin Anusha, Niva, Poojita, Niresh, Sanjeev, Hari, and Owais-thank you for your support and friendship.

I would like to recognize the support of the MICDE Graduate Fellowship. I would like to acknowledge the computing resources and assistance provided by Advanced Research Computing at the University of Michigan. I would also like to thank the resources provided by the NASA High-End Computing (HEC) Program through the NASA Advanced Supercomputing (NAS) Division at Ames Research Center. This work used Expanse clusters at UCSD through allocations from the ACCESS program, which is supported by U.S. National Science Foundation grants #2138259, #2138286, #2138307, #2137603, and #2138296. A portion of this thesis work was supported by the NASA SBIR contract no. 80NSSC20C0243, contract no. HDTRA125P0006 and Sandia contract no. SAND2023-07818O.

TABLE OF CONTENTS

List of Figures

List of Tables

ABSTRACT

High-speed shock-induced flow phenomena occur in a wide range of applications such as pulse detonation engines, volcanic eruptions, coal dust explosions and plume-surface interactions during spacecraft landings. These flows are multiphase involving strong interactions between the gas-phase and the particles. Turbulence transport and compressibility effects constitute complex physics in these multiphase flow interactions. While there has been significant effort and progress in modeling single-phase flows in the incompressible and compressible regimes, as well as multiphase incompressible flows, much less work has been done in modeling the microscale physics in multiphase turbulent flows at finite Mach numbers. Modeling challenges arise due to strong shock–particle–turbulence coupling, along with varying particle concentrations from dilute to dense, disparate particle diameter size ratios, and local instabilities.

The objective of this work is to leverage high-fidelity numerical simulations to delineate key physics associated with multiphase turbulence and guide the development of subgrid-scale models. To isolate shock–particle–turbulence interactions, we perform three-dimensional, particle-resolved simulations of a planar shock propagating through a suspension of stationary, monodisperse particles. The passage of the shock gives rise to unsteady wakes within the suspension (*pseudo-turbulence*). Numerical simulations are conducted using a high-order finite difference framework with low-dissipative, energy-preserving and shock-capturing properties. A ghost-point immersed boundary method is used to enforce no-slip, adiabatic boundary conditions at the surface of the particles. A budget for the pseudo-turbulent kinetic energy (PTKE) is derived from first-principles revealing the production due to drag and viscous dissipation to be the main generation/dissipation mechanisms. In-

creased compressibility effects due to increased shock Mach numbers are noted to reduce the overall magnitude of the PTKE budget terms. An energy spectrum analysis of the streamwise gas-phase fluctuations reveals an inertial subrange that begins at the scale of the interparticle spacing, follows a $-5/3$ scaling (similar to single-phase incompressible flow) and steepens to -3 at higher wave numbers. A Helmholtz decomposition of the velocity field reveals that the solenoidal component accounts for the majority of the fluctuations, while the dilatational component is small. A two-equation model for PTKE and its dissipation is proposed and implemented within a hyperbolic Eulerian-based two-fluid model and shows excellent agreement with the particle-resolved simulations.

The applications mentioned above typically involve polydisperse particle distributions. Wide size distributions are challenging to simulate within a particle-resolved framework due to computational constraints. In this work, we propose a coupled framework that combines the ghost-point immersed boundary method with the volume-filtered Euler–Lagrange framework, enabling the simulation of bidisperse particles with diameter size ratios on the order of $\mathcal{O}(10 - 100)$. This approach is utilized to investigate shock-induced size segregation in bidisperse particle suspensions. Hydrodynamic drag is the major contributing factor to size segregation, while the wakes (pseudo-turbulence) entrain particles, inhibiting segregation.

This thesis advances the understanding of turbulence and particle dispersion in multiphase compressible flows through highly resolved simulations spanning a wide range of shock Mach numbers $(1.2 - 3)$, particle volume fractions $(0.1 - 0.3)$ and bidisperse particle size ratios $(20 - 60)$. The results shed light on the PTKE transport, distribution of energy across length scales, effects of compressibility on turbulence production, and particle dispersion. The proposed model serves as closure for general application in coarse-grained simulation methods for particle-laden compressible flows.

CHAPTER 1

Introduction

The interaction of a shock wave with a suspension of solid particles is a complex compressible multiphase flow phenomenon observed in a multitude of natural and industrial applications. Some examples are found in volcanic eruptions [23, 69] and supernovae explosions [54, 86]. On the industrial front, applications such as heterogeneous detonations [151], pulsed-detonation engines [20, 113], and plume-surface interactions [14, 90, 103] during the powered descent of a lander module in interplanetary environments, exhibit such conditions.

These flows span a wide range of length and time scales. The interplay of compressibility effects and turbulence, in addition to strong coupling between the gas and the disperse phase, give rise to complex microscale physics. Furthermore, many applications involve chemical reactions, leading to heterogeneous burning rates within a particle suspensions. Over the past few decades, there has been significant effort and progress in modeling both single-phase and multiphase turbulence in the incompressible limits, as well as compressible (single-phase) turbulence. Much less work has been done for particle-laden compressible flows.

The objective of this work is to advance the understanding of the underlying physics governing such flows and to develop new models based on insights gleaned from high-fidelity simulations of shock–particle interactions. This introduction provides a brief overview of the above-stated applications, and establishes context for the technical studies detailed in the upcoming chapters.

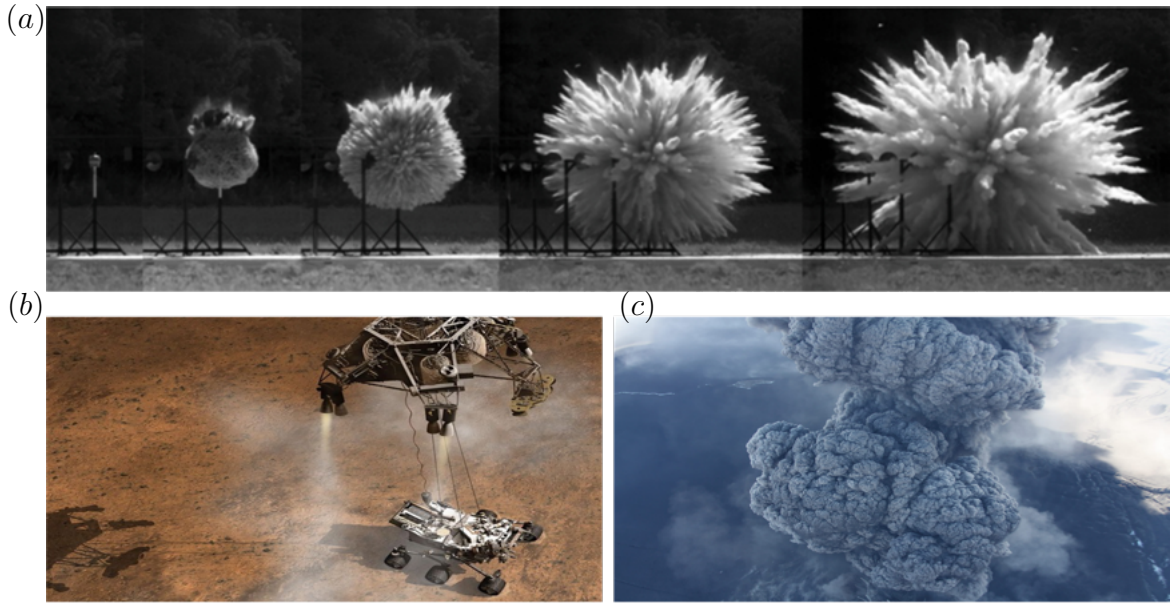

Figure 1.1: High-speed multiphase flows: (Top) Explosive dispersal of a packed bed of sand particles contained within a glass sphere [151]. (Bottom left) PSI during the landing of Curiosity rover on the Martian surface. Image Credit: NASA/JPL-Caltech. (Bottom right) A volcanic eruption comprising of hot gases and ash.

1.1 Motivating examples

Amongst several applications that exhibit shock–particle–turbulence flow phenomena, three examples that motivate the work in this thesis include detonations [43], volcanic eruptions [69], and plume-surface interactions (see Fig. 1.1). Each of these scenarios is characterized by high-speed flow dynamics in the presence of shock waves, significant compressibility effects, localized regions of turbulence, mixing, and dispersal of particles. In each, open questions remain regarding the accurate modeling and prediction of these flows, especially in the context of turbulence transport and its role on mixing and particle dispersion. This thesis is dedicated to advancing our understanding of the physics governing turbulence transport in such complex multiphase environments.

Figure 1.1(a) illustrates explosive dispersal of suspended sand particles [44]. The sand particles are suspended in a glass sphere and on detonation, a radially propagating shock wave is generated. When this detonation wave reaches the explosive charge surface, a blast

wave is transmitted into the air, with an expansion wave reflecting inwards; the expansion across solid particles leads to particle dispersion [45]. In this explosive process, the flow conditions range from close-packed (dense) flow within the charge to moderately-dense fluidized particulates within the expanding (dispersing) particles, to dilute flows at distances further out. Reaction-onset mechanisms are different for these different flow conditions and strongly depend on the concentration of the dispersed (fuel) phase and particle sizes [124]. Chemical reactions within the suspension affect particle ejecta dynamics [124, 151]. Finally, shock-driven multiphase instabilities (SDMI) can occur during shock impacting a particle cloud that induce particle dispersion in the form of jetting. [2, 43]. Accurately modeling and understanding this flow physics is essential for predicting and mitigating the impact of blast waves on nearby structures and environments [45]. The role of turbulence in modeling detonation experiments remains an open question. Developing computational frameworks that effectively incorporate turbulence effects is thus a critical objective for the computational study of explosive dispersal in detonation experiments [43].

In the event of landing on Lunar or Martian surfaces, spacecrafts use powered descent for slowing down. During the descent, exhaust plumes of the spacecraft interacts with the planetary regolith resulting in erosion of loosely packed surface particles [14, 77, 98, 103]. The phenomenon of this jet plume impinging on the surface regolith is referred to as plume-surface interactions (PSI) (illustrated in Fig. 1.1(b)). The consequences of PSI–erosion, ejecta, and cratering of regolith–are generally undesired due to the damage to onboard electronics in previous missions [89, 90, 103], and restricting visibility for seamless maneuver of the spacecrafts. PSI spans a wide range of flow regimes, from continuum flow within the plume to rarefied environments outside the plume. PSI is also characterized by two-phase flow with interphase coupling, which will be explained in the later sections. Additional phenomenon of plate shocks, wall shocks and stagnation bubbles characterize this flow [77]. As the plume interacts with the regolith, it generates cratering which leads to a recirculating turbulent zone [14, 77].

Another prominent example of multiphase flow is observed in pyroclastic density currents (PDCs), which arise from volcanic eruptions (Fig.1.1(c)). PDCs are turbulent, fast-moving mixtures of volcanic ash, rock fragments, and hot gases that travel downslope along a volcano [34, 69]. PDCs are generally categorized into dilute, turbulent upper layer governed by gas-particle drag, turbulent mixing and entrainment and a granular basal layer dominated by interparticle collisions, clustering and frictional forces [3, 8, 34, 69]. General numerical efforts for the study of PDCs [11, 12, 34, 35, 91] involve using a multi-fluid approach for the gas and disperse phase, which implies heavy reliance on subgrid scale closure models. Dufek & Bergantz implemented a two-equation transport model to capture microscale turbulence and its dissipation developed by Simonin [122]. However, this model was developed for incompressible, dilute conditions and fundamental uncertainties still exist, in how turbulence is generated, transported and dissipated in PDCs, including the modification of turbulence due to the influence of polydispersity, and clustering in PDCs [69].

The applications discussed above involve turbulent mixing that is influenced by both particles and compressibility. There is still a significant gap in our understanding of how turbulence operates in multiphase compressible flows and a dirth of accurate subgrid models in these limits. This thesis aims to deepen our understanding of turbulence transport in particle-laden compressible flows and to propose new models that can be applied to real-world scenarios.

1.2 Flow physics

1.2.1 Single-phase incompressible flows

Turbulence in single-phase flow is a well-studied phenomenon. An important feature of turbulent flows is the irregularity or the randomness in a flow field [104]. A velocity field u can be decomposed into a mean quantity and a fluctuating (turbulent) quantity via a

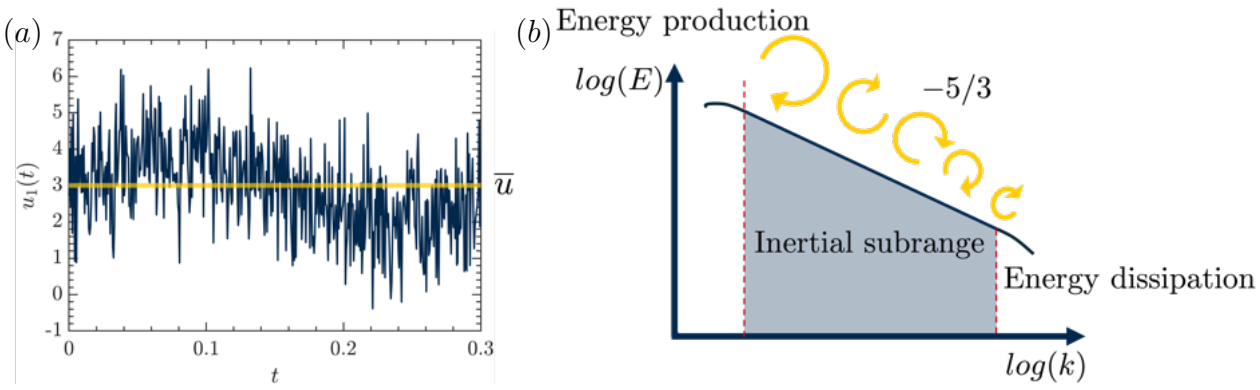

Figure 1.2: Illustration of a (a) random velocity field with the average $\overline{u}$ overlaid. (b) the energy cascade process of turbulence in single-phase flows.

Reynolds decomposition [108, 109], given by

$$u_i(x,t) = \bar{u}_i(x) + u_i'(x,t), \tag{1.1}$$

where $\bar{.}$ indicates the Reynolds- or time-averaged quantity and $.'$ the corresponding fluctuations. Figure 1.2(a) illustrates the time history of a random velocity $u(x,t)$ on the centerline of a turbulent jet. The Reynolds-average velocity $\bar{u}$ is shown by the straight line and is invariant with time, while the fluctuations in u are significant.

Based on this Reynolds decomposition, a set of Reynolds Averaged Navier–Stokes (RANS) equations was proposed [109] to describe turbulent flows. The RANS equation for $\overline{u}$ in incompressible flows is given by,

$$\frac{\partial \overline{u_i}}{\partial t} + \overline{u_j}\frac{\partial \overline{u_i}}{\partial x_j} = -\frac{1}{\rho}\frac{\partial \overline{p}}{\partial x_i} + \nu\frac{\partial^2 \overline{u_i}}{\partial x_j^2} - \frac{\partial \overline{u_i' u_j'}}{\partial x_j}, \tag{1.2}$$

where the $\overline{p}$ is a Reynolds-averaged pressure, ν is the kinematic viscosity, and $\overline{u_i' u_j'}$ is the Reynolds stress tensor–a term arising from averaging the non-linear convective term hat requires a closure model.

Richardson [110] postulated that turbulence is composed of eddies of different sizes. His hypothesis is that eddies of the largest sizes are unstable and break up into smaller eddies

until eventually, they are dissipated at the smallest of scales. The smallest relevant length scale corresponds to the Kolmogorov length scale η and is defined as,

$$\eta = \left(\frac{\nu^3}{\epsilon}\right)^{1/4}, \tag{1.3}$$

where ϵ is the energy dissipation. The classical theory of Kolmogorov [60, 104] extended this and suggests that there exists an energy production range, inertial subrange where energy scales according to $-5/3$ (shown in Fig. 1.2(b)), and finally, the dissipation range. This theory holds for homogeneous incompressible flows. In multi-component flows with scalars, the Batchelor scale η_B [5] defined as,

$$\eta_B = \frac{\eta}{\sqrt{Sc}}, \tag{1.4}$$

where Sc is the Schmidt number (defined in later sections). The Batchelor length scale is an important scale which describes the fluctuations in scalar concentration and controls mixing due to mass diffusivity.

Turbulent kinetic energy (TKE) is the energy associated with the fluctuating velocity and is defined as $k = \overline{u_i' u_i'}/2$. This is the trace of the Reynolds stress mentioned in (1.2). The budget for TKE describes the energy balance in turbulent flows. The budget reveals the production due to shear in the mean flow, the transport, and TKE dissipation by viscous forces (dissipation). Classical turbulence theory was originally formulated for incompressible flows, and as a result, it cannot be directly applied to scenarios involving significant compressibility effects.

1.2.2 Single-phase compressible flows

Compressible turbulence is further complicated by variations in pressure and density fields. Studies through the 1990s [13, 66, 117, 118, 143] focused on the effects of compressibility on

turbulence generation and production through configurations of homogeneous isotropic turbulence, turbulent mixing layers, and grid-generated turbulence experiments. The turbulent Mach number, M_t, is a key quantity for characterizing the effects of compressibility, defined as

$$M_t = \frac{\sqrt{u_i' u_i'}}{c}, \tag{1.5}$$

where c is the speed of sound. For values of $M_t \leq 0.3$, a large scale separation exists between acoustics and turbulence. This results in a nearly incompressible flow called the quasi-isentropic regime. For higher values of M_t (i.e. $0.3 < M_t \leq 0.6$), dilatational effects are significant, leading to a nonlinear subsonic regime. The flows considered in the present study predominantly fall within this regime.

Since the 1970s, numerous studies have investigated the role of compressibility in the development of turbulent mixing layers and the generation of turbulent kinetic energy [10, 13, 118]. Sarkar et al. [118] derived a budget for the Reynolds stress in compressible flows, given (in Einstein notation) by,

$$\partial_t(\overline{\rho}\widetilde{u_i'' u_j''}) + (\overline{\rho}\widetilde{u}_k\widetilde{u_i'' u_j''})_{,k} = P_{ij} - T_{ijk,k} + \Pi_{ij} - \overline{\rho}\epsilon_{ij} - \overline{u_i''}\overline{p}_{,j} - \overline{u_j''}\overline{p}_{,i} + \overline{u_i''}\overline{\sigma}_{jk,k} + \overline{u_j''}\overline{\sigma}_{ik,k}, \tag{1.6}$$

where

$$P_{ij} = -\overline{\rho}(\widetilde{u_i'' u_k''}\widetilde{u}_{j,k} + \widetilde{u_j'' u_k''}\widetilde{u}_{i,k}), \tag{1.7}$$

$$T_{ijk} = \overline{\rho}\widetilde{u_i'' u_j'' u_k''} + (\overline{p' u_i'}\delta_{jk} + \overline{p' u_j'}\delta_{ik}) - (\overline{u_i'' \sigma_{jk}'} + \overline{u_j' \sigma_{ik}'}), \tag{1.8}$$

$$\Pi_{ij} = \overline{p' u_{i,j}'} + \overline{p' u_{j,i}'}, \tag{1.9}$$

$$\overline{\rho}\epsilon_{ij} = \overline{\sigma_{ik}' u_{j,k}'} + \overline{\sigma_{jk}' u_{i,k}'}, \tag{1.10}$$

where σ is the viscous stress. $\widetilde{.} = \overline{\rho.}/\overline{\rho}$ is a Favre-averaged quantity and $.''$ denotes the fluctuation associated with this average. P_{ij} represents the production due to mean shear, T_{ijk} accounts for diffusive transport, Π_{ij} denotes the pressure-dilatation correlation and $\overline{\rho}\epsilon_{ij}$

is the viscous dissipation term.

Sarkar et al. [118] and Zeman [150] examined the effects of dilatational dissipation, ϵ_d, finding that its increase with M_t leads to a reduction in turbulent kinetic energy, thereby decreasing turbulent mixing. They suggested that the suppression of the growth rate is linked to increased ϵ_d from shocklets. They also developed a mathematical model to incorporate this effect into Reynolds stress closure models. However, Sarkar [117] later showed, using direct numerical simulations of turbulent homogeneous shear flow, that the reduction of TKE is primarily due to decreased turbulence production, rather than directly caused by dilatational dissipation. Subsequent studies by Vreman et al. [143] and Pantano & Sarkar [97] corroborated this finding, showing that dilatational dissipation is negligible. Instead, the reduced growth rate of turbulence is linked to diminished pressure fluctuations and, consequently, lower turbulence production resulting from a reduction in the pressure-strain term.

Kida & Orszag [59] were among the first to analyze the kinetic energy spectrum in forced compressible turbulence, observing that its scaling of -5/3 is largely independent of Mach number. Donzis & Jagannathan [30] also found that the turbulent kinetic energy spectrum in compressible isotropic turbulence follows a $-5/3$ power law in the inertial range for $0.1 \leq M_t \leq 0.6$, consistent with the classical Kolmogorov scaling for incompressible flows [60]. Further insights into compressibility scaling emerge from a Helmholtz decomposition of the velocity field u into its solenoidal component u_s and dilatational component u_d [30, 59, 115, 146, 147]. Compressibility effects are typically attributed to u_d, and both [30] and [146] observed that the majority of turbulent kinetic energy resides in the solenoidal component, with u_d increasing with M_t. However, all of these studies have focused on single-phase compressible turbulent flows in the absence of particles.

1.2.3 Multiphase incompressible flows

Multiphase flows consist of a gas phase and a dispersed phase. A key parameter defining the concentration of the dispersed phase within the gas phase is the particle volume fraction

(Φ_p). It is defined as the ratio of the volume occupied by the solid particles (V_p) to the total volume (V) as,

$$\Phi_p = \frac{V_p}{V}. \tag{1.11}$$

As the introduction briefly hinted, the particle volume fraction classifies a multiphase problem into three regimes: dilute, moderately dense, and granular [4, 37]. In dilute flows ($\Phi_p < 0.001$), the fluid phase effects the dynamics of the particles, but the reverse is not true. Particle-particle collisions can also be neglected, thus making the flow one-way coupled.

In moderately dense regimes, the presence of particles substantially influences the gas-phase mass, momentum, and energy balances. At this stage, two-way coupling—where not only does the gas affect particle behavior, but particles also exert significant feedback on the gas—becomes important. Four-way coupling incorporates interparticle collision effects. As the particle volume fraction approaches unity, frictional forces between particles grow increasingly significant. In this thesis, the particle suspension has concentrations in the moderately dense regime with particle volume fractions ranging from 0.1 to 0.3.

The particle Reynolds number is defined using the particle diameter and slip velocity as,

$$Re_p = \frac{|u_i - v_i| d_p}{\nu}. \tag{1.12}$$

where $|u_i - v_i|$ is the slip velocity between the particle velocity (v_i) and the gas (u_i). The particle Reynolds number plays a crucial role in determining the amount of turbulence generated or dissipated by particles. At moderate Re_p, the flow separates to form a recirculating eddy in the particle wake. For $Re_p > 280$, the wake of an isolated particle becomes time-dependent and begins to shed vortices, and becomes fully turbulent at $Re_p > 500$.

The particle response time τ_p represents the time it takes for a particle to respond to changes in the flow in the Stokes limit, given by

$$\tau_p = \frac{\rho_p d_p^2}{18 \rho \nu}, \tag{1.13}$$

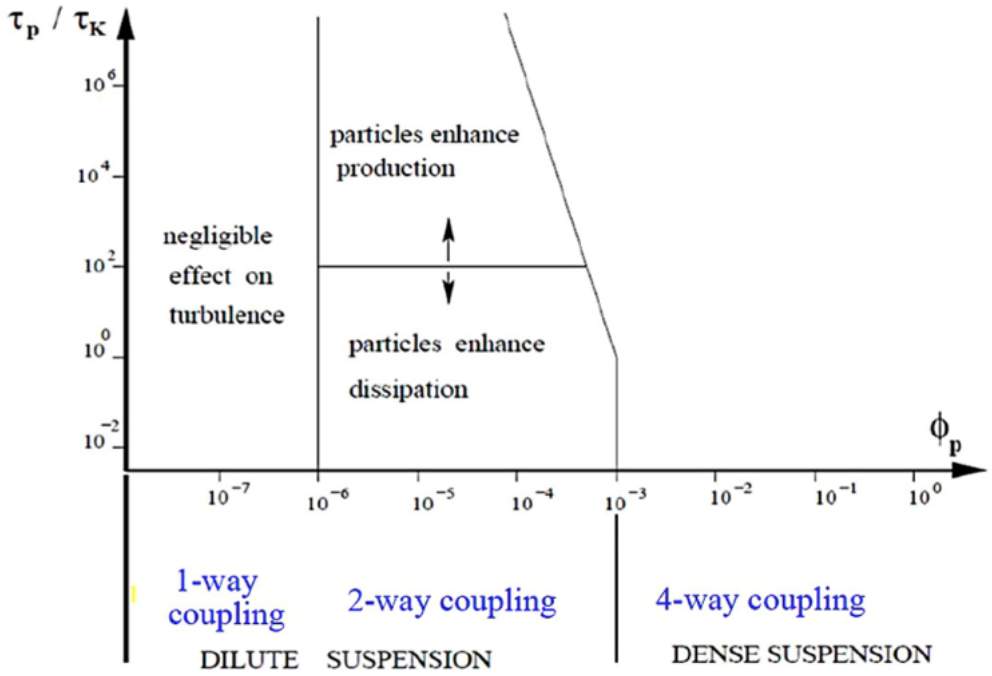

Figure 1.3: Classification map for particle-laden turbulent flows [36, 37, 130]

where ρ_p is the particle density. The ratio of the particle time scale to the fluid scale leads to the Stokes number,

$$St = \frac{\tau_p}{\tau_f}, \tag{1.14}$$

where τ_f is the characteristic timescale of the fluid. In homogeneous turbulence, $\tau_f = \sqrt{\nu/\epsilon}$. The Stokes number defines how inertial particles are, with small $St \ll 1$ characterizing tracer particles and intermediate St giving rise to clustering (preferential concentration) due to the ability of particles to cross fluid streamlines.

Figure 1.3 summarizes the flow regimes in incompressible flows [36, 37] based on the particle volume fraction and the Stokes number. Values of $\Phi_p < 10^{-6}$ imply one-way coupling, where particles have negligible effect on turbulence. For $10^{-6} < \Phi_p < 10^{-3}$, particles modify flow through drag or heat transfer, termed two-way coupling. For volume fractions higher than 10^{-3}, particle–particle interactions (collisions and wake-wake interactions) necessitate four-way coupling. The demarcation line between two-way and four-way coupling shifts to lower Φ_p at $St = 0.7$.

Multiphase turbulence is different from classic single-phase turbulent flows. Fluid velocity fluctuations induced by particle wakes are referred to as pseudo-turbulence [63, 75], a term also applied to bubble-induced turbulence (BIT) in liquid flows [111]. Lance & Batatille [63] first demonstrated that a homogeneous swarm of bubbles generates pseudo-turbulence with a spectral subrange exhibiting a -3 power law. They showed that at statistically steady state, this spectral scaling results from a balance between viscous dissipation and energy production due to drag forces from rising bubbles. Similar scaling has since been observed in other bubbly flows [82–84, 111]. Subsequent experimental studies coupling BIT with shear-induced turbulence have found that the spectra of liquid velocity fluctuations follow a -3 scaling at small wave numbers, transitioning to a $-5/3$ scaling at higher wave numbers, suggesting a single-phase signature is preserved at the smallest scales [111]. Numerical simulations of gas–particle turbulent channel flow reveal that two-way coupling between the phases results in reduction in fluid-phase turbulent kinetic energy at the scale of individual particles, while a broadband reduction over all scales is observed at moderate to high mass loading [17].

Over the past few decades, turbulence models have evolved to incorporate the effects of particles [39, 71, 138]. A production term must be included to account for generation of turbulence through drag. A dissipation time scale is often employed based on the slip velocity between the phases and particle diameter (d_p), given by $\tau = d_p/|v_p - u|$. The use of two-equation transport models for gas–solid flows dates back to the work of Elghobashi [38], who derived a rigorous set of equations for dilute concentrations of particles in incompressible flow using a two-fluid approach. Since then, models have been proposed for denser regimes in shear turbulence [70]. Crowe et al. [26] provided a review of numerical models for turbulent kinetic energy in two-phase flows. However, these models are limited to *intrinsic turbulence* whereby the carrier-phase turbulence would exist even in the absence of particles, as opposed to pseudo-turbulence that is entirely generated by the particle phase. Mehrabadi et al. [75] more recently developed an algebraic model for pseudo-turbulent kinetic energy (PTKE)

based on particle-resolved simulation data for incompressible homogeneous gas solid flows in the range $0.1 \leq \alpha_p \leq 0.5$, and $Re_p \leq 300$ as,

$$\frac{k}{E} = 2\alpha_p + 2.5\alpha_p\alpha^3 \exp(-\alpha_p {Re_p}^{1/2}), \tag{1.15}$$

where α_p and α are the local particle and gas phase volume fractions respectively. A limitation of this model is that PTKE can only be predicted in regions of finite volume fraction. Also, in the limit of large Re_p, this model shows that the normalized TKE scales linearly with α_p.

1.2.4 Multiphase compressible flows

Very few canonical flow configurations exist that isolate the physics of particle-laden compressible flows. In this work, we focus on a particle-laden shock tube. This canonical setup provides a means of analyzing the fundamental behavior of multiphase compressible flows and has been investigated both numerically [79, 80, 93, 95, 121] and experimentally [28, 29, 68, 144]. Figure 1.4 presents a schematic of this configuration at initial time ($t = 0$) and at later stages ($t > 0$). In this system, a suspension of solid particles is subjected to an incident planar shock wave. Upon encountering the suspension, the shock splits: a transmitted shock travels downstream, generating gas-phase fluctuations via particle wakes, while the initial interaction at the upstream edge leads to the formation of multiple shocklets that eventually coalesce into a reflected shock propagating upstream. Notably, at the downstream edge of the suspension, localized regions of supersonic flow are observed as a result of sudden changes in area caused by variations in particle volume fraction, similar to an expanding nozzle [121, 136].

The shock Mach number M_s is defined as,

$$M_s = \frac{u_s}{c}, \tag{1.16}$$

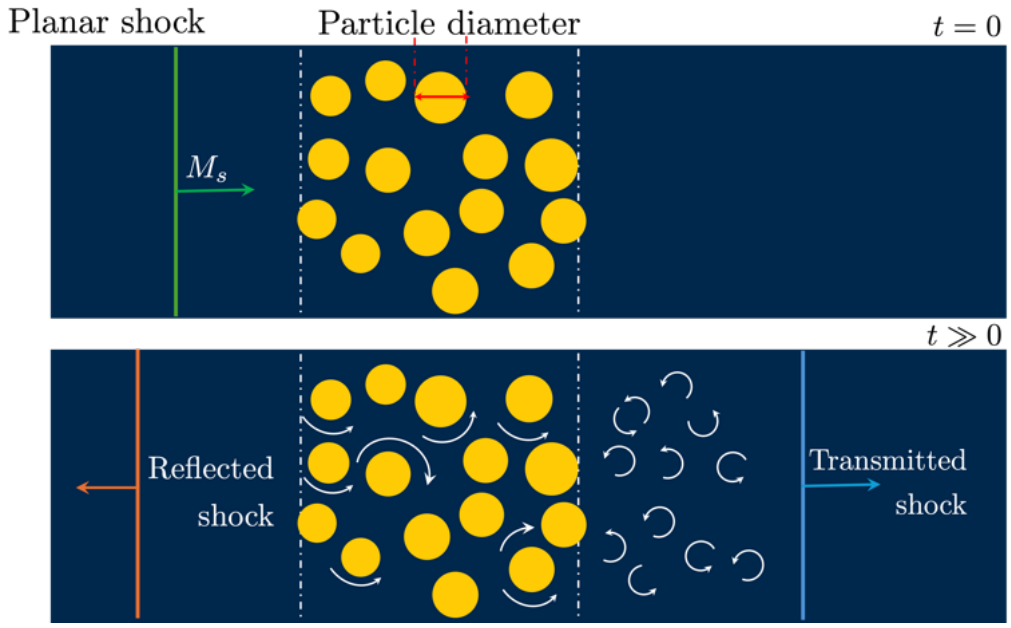

Figure 1.4: Schematic of a particle-laden shock tube. Yellow circles indicate the dispersed phase. Particle wakes and subsequent turbulence are shown as white arrows.

where u_s is the speed of the shock wave. It characterizes the degree of compressibility of the fluid. The high-speed nature of these flows leads to the formation of compressible structures after interacting with an impinging surface, such as shocklets within the suspension.

Figure 1.5 shows an updated regime map of Fig. 1.3, accounting for the effects of compressibility [18]. Higher the M_s, greater the influence of the particles on the shock structures. Figure 1.6 shows the numerical simulation of a shock interacting with bidisperse particles. Multiple shocklets formed within the interstitial spaces of this moderately-dense particle suspension. In high-speed flows, the emergence of bow shocks around individual particles and reflected shocks from neighboring particles complicates this picture.

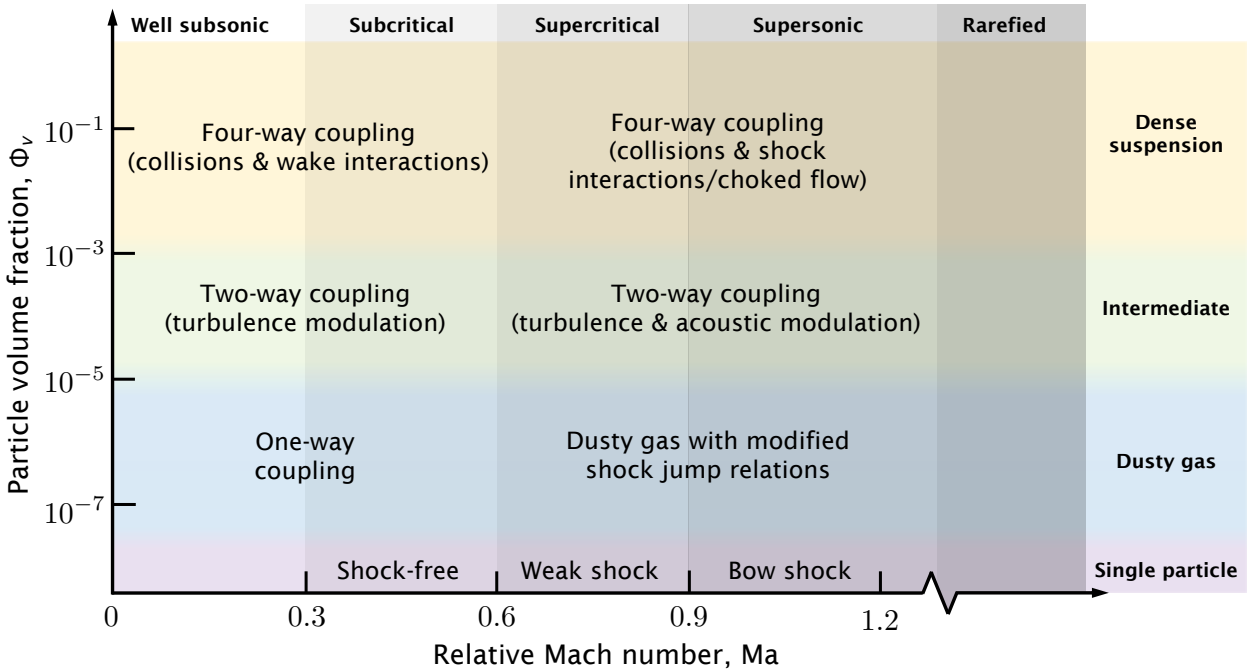

Figure 1.5: Different regimes characterizing fluid-particle interactions in high Reynolds number flows. The present review is primarily concerned with gas-particle flows ($\rho_p/\rho \gg 1$) in the continuum regime ($M_s/Re_p \ll 1$). One-way coupling is applicable to incompressible and subsonic (shock-free) flows at low volume fractions. At higher Mach numbers but still low volume fractions, particles are capable of modifying shock structures. At higher volume fractions and low Mach numbers, momentum exchange between the phases is capable of enhancing or attenuating gas-phase turbulence. Dense suspensions in high Mach number flows correspond to explosive dispersal of particles with strong shock-particle-turbulence interactions. This figure has been adapted from [18]

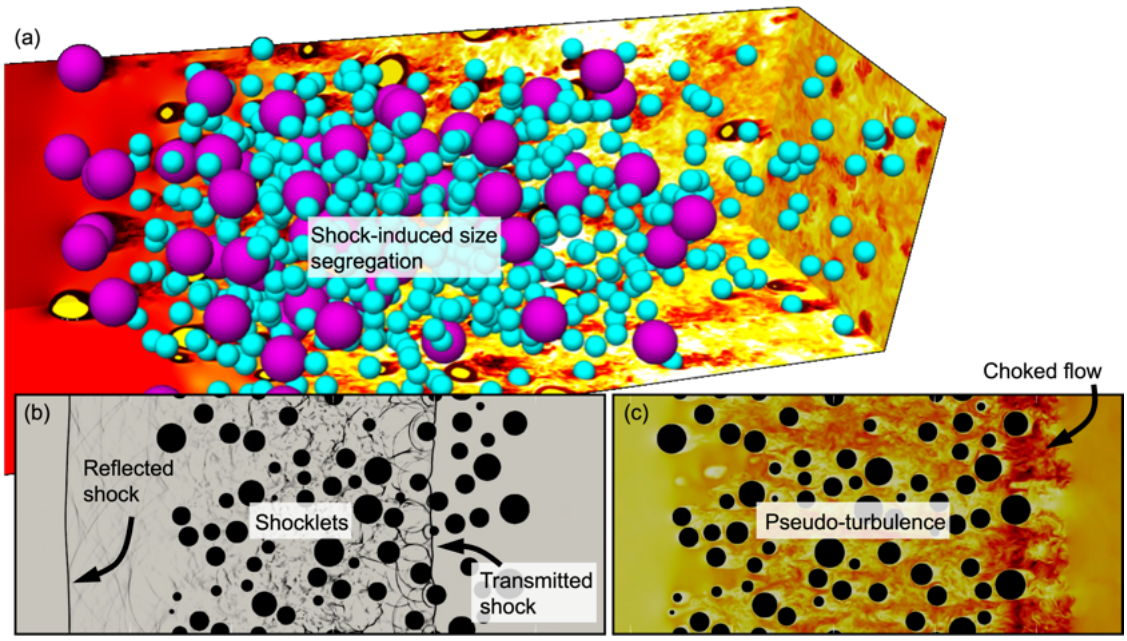

Figure 1.6: Particle-resolved simulations of a $M_s = 1.66$ shock interacting with a particle curtain with an initial volume fraction $\Phi_p = 0.21$. (a) Bidisperse distribution of particles after the shock traverses the curtain. (b) Numerical schlieren at an early time when the shock is still within the curtain. (c) Contour of local Mach number shortly after the shock passes the curtain. Adapted from [18]

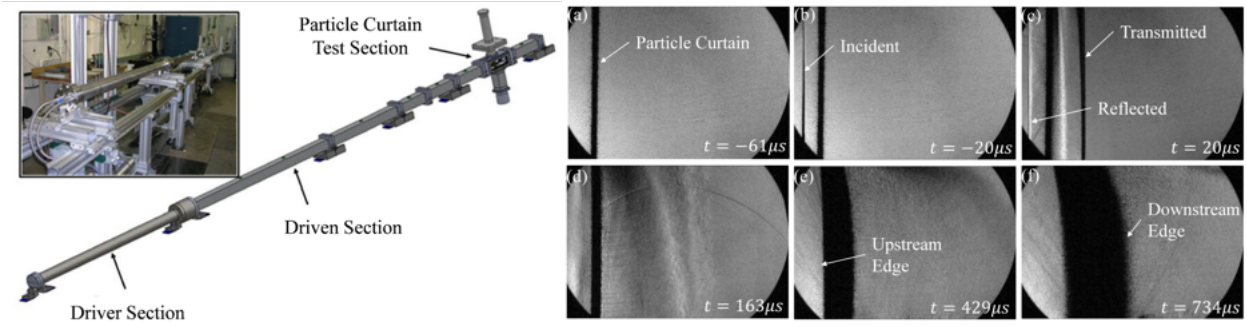

Figure 1.7: (a) Schematic and photograph of the Sandia multiphase shock tube [144] (b) Schlieren imaging of a shock wave interaction with a stainless steel particle curtain. [28]

1.3 Existing literature on shock–particle interactions

1.3.1 Experimental efforts

Numerous experimental investigations of compressible gas-solid flows using shock tube setups have been reported in the literature. In 1998, Rogue et al. [112] conducted experiments on shock-induced fluidization of densely packed particle beds and noted the formation of a reflected shock wave that traveled upstream, which was absent in dilute particle-laden flows. Their study presented data on pressure histories and the dispersal of the particle bed following shock impingement. However, the mechanisms governing particle dispersal in moderately dense suspensions with volume fractions $\Phi_p < 0.4$ remained unclear. To gain insight into this, Wagner et al. [144] built a multiphase shock tube (MST) facility at Sandia to provide the unique capabilities necessary to study moderately dense suspensions impacted by a shock. Figure 1.7(a) shows a schematic of the multiphase shock tube, which consists of a driver section supplied by a high pressure Nitrogen system, a driven section with ambient air and a diaphragm that ruptures to produce shock waves. Figure 1.7(b) shows the Schlieren results of an experimental run for $\Phi_p = 0.17$. The passage of the shock establishes a favorable pressure gradient across the curtain, causing particles at the downstream edge to move faster than the upstream, which results in its overall expansion [29, 144].

A multitude of experiments have been performed using the MST [28, 29, 68, 144] for a range of parameters–Φ_p, M_s, ρ_p, and the initial curtain thickness δ_0. It was found that higher the M_s, faster the curtain spread. Experiments by Theofanus et al. [135] suggest faster spread with increasing Φ_p and lower δ_0. Daniel et al. [28] recently proposed a scaling based on the pressure behind the shock wave reflecting off an idealized solid boundary, which successfully collapsed experimental data [68, 135, 144], expressed as

$$\frac{x}{\delta_0} \propto \left(\Phi_p^{0.25} \frac{\sqrt{\rho_0} u_{ind} t}{\sqrt{\rho_p} \delta_0} \right)^2 . \tag{1.17}$$

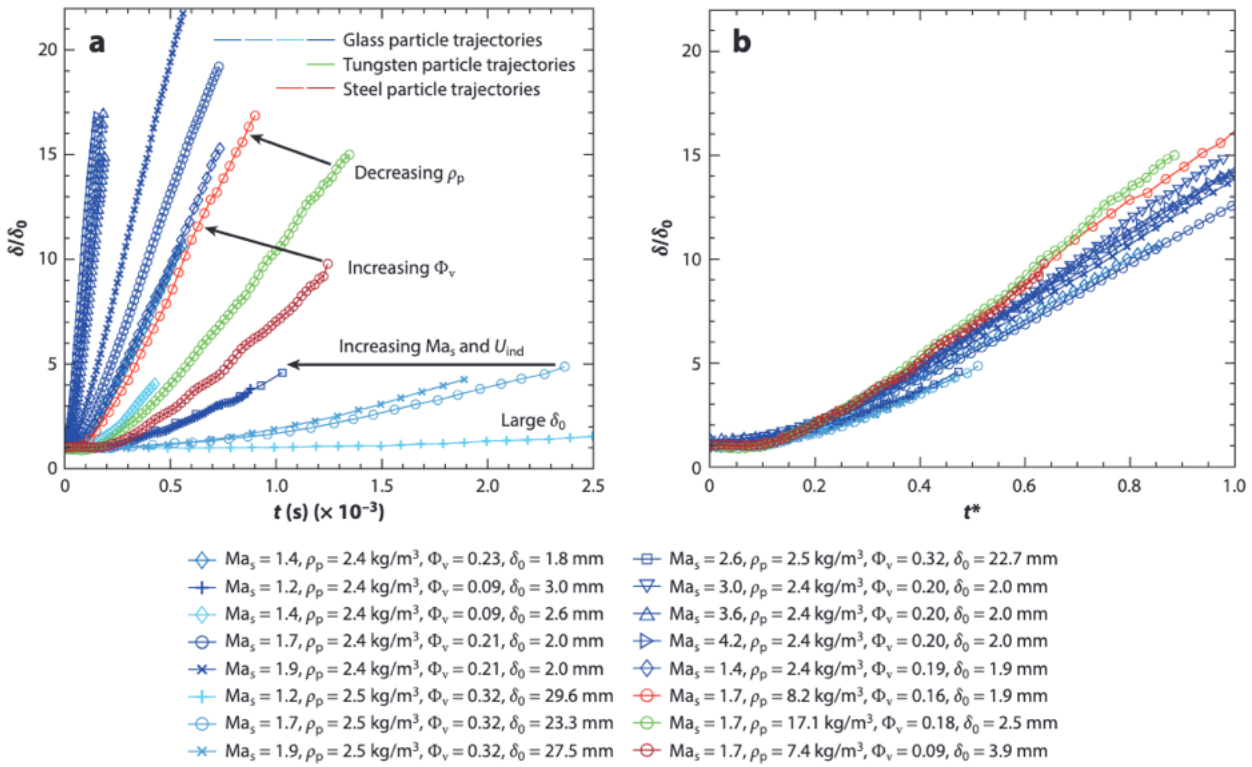

Figure 1.8: Comparison of historical particle curtain spread data. (a) Non-dimensional spread δ/δ_0 versus time, and (b) δ/δ_0 versus t_*. Glass particle trajectories are shown in blue, tungsten in green, and steel in red. Adapted from [18].

Figure 1.8 highlights the spreading of the curtain with various parameters in (a) and the collapsed spread in (b) using the scaling law of Daniel et al. [28]. Despite progress, several questions still remain for shock-induced particle flows. Polydispersity in the suspension and its effect on size segregation between particles is currently still unknown. Additionally, such experiments remain limited in their ability to quantify turbulence within the suspension and whether that might have an effect on the particle curtain dispersal. While large-scale quantities such as pressure drop across the curtain and particle curtain spread can be determined through experiments, the analysis of microscale features such as wakes and turbulence requires computational approaches.

1.3.2 Numerical studies

Three distinct approaches exist to perform numerical simulations of multiphase compressible flows. Euler–Euler [40, 52] and Euler–Lagrange [16, 121] methods have been gaining promise for simulating these types of flows but rely heavily on unclosed terms that account for physics at the particle scale. Both of these frameworks utilize averaging or filtering techniques over a control volume to employ resolutions higher than the particle size, which inevitably results in unclosed terms that require modeling. The majority of these models have been developed for incompressible flows, and only very recently have particle-resolved direct numerical simulations (PR-DNS), which apply grid spacing smaller than the particle diameter so that drag does not rely on models but is computed from the resolved stresses, of compressible multiphase come online.

For large-scale system modeling ($\mathcal{O}(10^8)$), the method of Euler–Euler or two-fluid model (TFM) is more appropriate. The equations are derived from kinetic theory [9, 39, 41]. Fox [9, 41] and Houim & Oran [52] developed compressible frameworks using TFM for multiphase flows and validated against data from experiments. They validated the model against experimental data for shock-induced particle dispersal. In the context of shock–particle interactions, the model accuracy, however is strongly dependent on the definition of particle edges. Furthermore, TFM heavily relies on correlations for interphase drag and heat exchange. More recently, Boniou & Fox [9] presented results of one-dimensional Euler–Euler simulations for the shock-curtain configuration and cite the need for three-dimensional results and inclusion of polydispersity.

Euler–Lagrange (EL) methods involve tracking the particles individually as Lagrangian quantities. The interface between the gas and the dispersed phase is not fully resolved, and thus relies on correlations developed from PR-DNS or experiments for the interphase momentum and energy exchange [16, 98, 121]. Ling et al. [68] performed Euler-Lagrange simulations and validated results against experimental data for particle curtain spreads, and pressure measurements [144], varying key parameters of M_s, Φ_p, and d_p, and achieved

good results. Shallcross et al.[121] derived a volume-filtered Euler–Lagrange formulation for compressible multiphase flows and showed that PTKE systematically contributed to reduced local gas-phase pressure and consequently, increased the local Mach number. They proposed a transport model for PTKE with an algebraic model for dissipation. They showed good agreement with PR-DNS results, although the results were found to be sensitive to the dissipation model.

Particle-resolved direct numerical simulations (PR-DNS), restrict overall number of particles to $\mathcal{O}(10^3)$ [79, 80, 95, 96]. PR-DNS studies have only recently started to emerge [79, 80, 93, 95, 96, 105]. Regele et al. [106] were one of the first to perform numerical studies of a shock passing through cylindrical particles using two-dimensional simulations. Their results demonstrated that the strength of the fluctuations was of the order of mean velocity. Subsequently, Hosseinzadeh et al. [50] conducted viscous simulations and found that this magnitude of fluctuations or pseudo-turbulence contributed to a significant portion (up to 50%) of the total energy. Mehta et al. [80, 81] successfully performed fully resolved three-dimensional inviscid simulations of monodispersed spherical particles. They reported that the random distribution of the particles significantly altered the force history of each particle compared to that of an isolated particle. Osnes et al. [93, 95, 96] first conducted extensive particle-resolved three-dimensional studied evaluating viscous effects, and sensitivity of the fluctuations to parameters of interest (mainly M_s, Φ_p, and Re_p). Osnes et al. [95] proposed an algebraic model proportional for the streamwise component of PTKE. They note that the particle wakes and fluctuations are generated non-instantaneously after the shock wave passes over a particle and the model does not account for this time-delay. Finally, the algebraic models developed by Mehrabadi et al. [75](Eq. (1.15)) and Osnes et al. [95] predict PTKE to be zero, in the absence of particles.

There remains a need for PR-DNS of viscous shock–particle interactions to generate comprehensive data sets and support the development of robust closure models for use in Euler–Euler and Euler–Lagrange approaches. This constitutes one of the principal objectives

of the current study.

1.4 Objectives

Understanding of shock–particle–turbulence interactions remains limited, despite ongoing experimental and numerical investigations. In this work, we utilize a high-fidelity computational framework to explore the underlying mechanisms of multiphase turbulence and the influences of compressibility. The primary objective is to understand the microscale physics through high-fidelity PR-DNS data, which in turn is used to inform the development of state-of-the-art models for predicting turbulence in multiphase flows. Furthermore, we assess the effects of polydispersity and introduce a tractable framework capable of efficiently capturing the dynamics of size segregation for particles with large size ratios. While this work centers on the shock tube problem, the methodologies and insights offered herein are broadly applicable to compressible multiphase flows. The objectives of this thesis are listed below:

1. Develop a tractable framework to enable the simulation of bidisperse particles with large size ratios for size segregation, and support particle-resolved simulations to quantify particle-induced turbulence.

2. Quantify the specific mechanisms governing production, transport, and dissipation of turbulence with a focus on understanding how M_s and Φ_p influence turbulence characteristics. Additionally, we aim to provide insights into turbulence transport across scales and assess the effects of the multiphase nature of the flow and compressibility.

3. Propose a model for PTKE and perform a-posteriori validation using coarse-grained Euler-Euler simulations.

4. Conduct a systematic parametric analysis to evaluate the effects of Mach number (M_s), volume fraction (Φ_p), and the particle size ratio (D/d) on size segregation dynamics.

1.5 Organization

The thesis is divided into four chapters. The majority of Chapters 2– 5 has contributions from manuscripts that have already been published.

1. Chapter 2 details the development and application of a high-fidelity numerical framework for simulating compressible flows containing bidisperse particles with large size ratios. The volume-filtered Navier-Stokes equations are discretized using a class of high-order low-dissipative finite difference operators with energy-preserving properties. No-slip, adiabatic boundary conditions are enforced at the surface of large particles (with diameters significantly larger than the local grid spacing) using a ghost-point immersed boundary method. Two-way coupling between the gas phase and small particles (with diameters proportional to the grid spacing) is accounted for through volumetric source terms for interphase momentum and energy exchange. A simple and efficient approach for collision detection between small and large particles is proposed. A portion of this work was published in *Acta Mechanica Sinica* [127].

2. Chapter 3 investigates the fundamental mechanisms underlying wake-induced gas-phase velocity fluctuations—commonly referred to as pseudo-turbulence—generated when planar shocks interact with stationary particle suspensions. Leveraging detailed three-dimensional particle-resolved simulations, this chapter seeks to quantify the evolution and budget of pseudo-turbulent kinetic energy (PTKE), providing insight into its generation, transport, and dissipation. Additionally, it examines anisotropy of PTKE, and energy spectra elucidating how turbulent characteristics change across different length scales. To advance predictive modeling, a two-equation model for PTKE and its dissipation is proposed, and is tested a-posteriori within a one-dimensional Euler-Euler framework. Good agreement with PR-DNS is achieved. The research outcomes from this chapter under production for publishing in *Journal of Fluid Mechanics* [128].

3. The developed IBM/EL framework is applied to simulations of planar shocks interact-

ing with bidisperse distributions of particles with size ratios of approximately thirty in Chapter 4. Particle dispersion and size segregation are reported, along with one-dimensional quantities of PTKE and volume fraction profiles, and a simple analytical model for size segregation is proposed. This work was published in *Acta Mechanica Sinica* [127].

4. In Chapter 5, the sensitivity of particle-induced size segregation to parameters of interest are evaluated. New scaling laws are proposed for particle suspension spread and size segregation ratio. A portion of this chapter is published in the *AIAA Journal* [126].

5. Chapter 6 summarizes the study's key findings, conclusions, and outlines directions for future research. Additionally, this chapter provides an overview of ongoing investigations into passive scalar transport and discusses current simulation efforts that extend the scope of the research.

CHAPTER 2

A Hybrid Volume–Filtered Euler–Lagrange/IBM Framework For Bidisperse Particle-Laden Compressible Flows

Note: A portion of this chapter is published in *Acta Mechanica Sinica* [127]. Data and figures have been used with all co-authors' consent.

2.1 Abstract

In this chapter, a novel framework for simulating viscous compressible flows in the presence of bidisperse solid particles with large size ratios is proposed. The volume-filtered Navier–Stokes equations are discretized using a class of high-order low-dissipative finite difference operators with energy-preserving properties. No-slip, adiabatic boundary conditions are enforced at the surface of large particles (with diameters significantly larger than the local grid spacing) using a ghost-point immersed boundary method. Two-way coupling between the gas phase and small particles (with diameters proportional to the grid spacing) is accounted for through volumetric source terms for interphase momentum and energy exchange. A simple and efficient approach for collision detection between small and large particles is proposed.

2.2 Introduction

Particle dispersal in high-speed flows is a complex phenomenon common to various natural processes, such as volcanic eruptions [69, 140] and supernovae explosions. Engineering applications include mining safety from coal-dust explosions [51, 116, 152], heterogeneous detonation blasts [151], and plume-surface interactions during planetary and lunar landings [77]. These applications often involve highly compressible flows characterized by shocks, fluid instabilities, turbulence, and chemical reactions. Moreover, strong coupling exists between the gas phase and solid particles, which exhibit a wide range of sizes, densities, and concentrations, ranging from dilute to dense regimes. A deeper understanding of the underlying physics is necessary to mitigate the detrimental effects of particle dispersal and enhance safety measures in the stated applications.

Particle-laden flows are often polydisperse, leading to size segregation in fluidized systems. While certain applications benefit from particle separation, size segregation can impede mixing processes. Hydrodynamic forces acting on particles of different sizes result in varied slip velocities. These slip velocity differences generate net momentum disparities between particle classes, contributing to size segregation [7, 74, 76]. Collisions between particles of different sizes cause net momentum transfer, referred to as a particle-particle drag force [32, 76], which is another crucial factor influencing size segregation. In dense suspensions, frequent collisions significantly reduce the relative velocity between particle classes, thereby decreasing segregation. The interplay between hydrodynamically induced slip velocity and the particle-particle drag force dictates the system's overall behavior and segregation [76].

Bidisperse systems made up of large particles with diameter D and smaller particles with diameter d represent the most fundamental polydisperse configuration. Analysis of segregation and the dominant mechanisms at play provides a basis for understanding and modeling more complex configurations [7, 32, 76]. Previous studies on bidisperse flows focused on homogeneous suspensions [76] and fluidized beds [16]. Studies of particle segregation in compressible flows are rare. Beetstra et al. [7] performed simulations of incompressible flow

over monodisperse and bidisperse particles using a Lattice Boltzmann method for particle diameter ratios $D/d = 1$ to 4. They proposed a nonlinear drag law that is a function of particle diameter ratio and it was later verified to hold up to a $D/d = 10$ by Sarkar et al. [119]. Capecelatro and Wagner [18] presented qualitative results of shock-induced size segregation with particle size ratio $D/d = 2$, highlighting localized gas-phase fluctuations due to the presence of particles (termed pseudo-turbulence). More recently, Sridhar and Capecelatro [125] investigated the effects of varying particle volume fraction, shock Mach number, and diameter size ratios $D/d \in [12, 40]$ on size segregation and proposed scaling laws for two-dimensional flow configurations. The segregation rate was observed to increase with particle volume fraction and post-shock velocity and decrease with D/d. This paper presents the framework in greater detail and extends our previous work to three-dimensional configurations for the case of shock-induced size segregation and dispersal.

Immersed boundary methods (IBM) are a popular choice for particle-resolved simulations. It was originally proposed by Peskin [101] for biological incompressible flows. Mohd-Yusof [88] proposed a ghost-point method for the simulations with rigid boundaries that was later extended to compressible flows by Chaudhuri et al [21], which we adopt in the present work. Several other techniques exist, such as cut-cell [24, 53, 107] and characteristic-based volume penalization [78, 120]. Cheng and Wachs [22] used an IBM/Lattice Boltzmann method to simulate flow past stationary bidisperse spheres and concluded that the average force on large particles is much larger than the small ones for the size ratios considered. Mehta et al. [78] proposed a numerical framework for freely evolving particles using a characteristic-based volume penalization method with adaptive wavelet collocation for local mesh refinement, accounting for collisions using a hard-sphere model. Theofanous et al. [136] performed particle-resolved simulations to study shock dispersal of dilute particle clouds. They observed a flow choking phenomenon at the downstream edge of the particle cloud where the local volume fraction suddenly drops. This choking behavior was followed by significant supersonic expansion, resulting in high particle acceleration.

Accurately capturing hydrodynamic forces and collisions in systems with particles of large size ratios remains a significant challenge for numerical simulations. Particle-resolved numerical simulations provide the most comprehensive framework, capturing all relevant scales of motion in multiphase systems [134]. However, the computational cost of resolving fluid boundary layers on both the largest and smallest particles is prohibitive. Consequently, existing methods are generally limited to small particle size ratios (with $D/d < 5$) and a small number of particles [7, 22, 74, 76].

In this work, we propose a hybrid approach that resolves fluid stresses on the surfaces of large particles using IBM, while small particles are tracked using an Euler–Lagrange approach that relies on drag and heat transfer models. Special care is taken to efficiently handle collision detection between particles of varying size.

2.3 Numerical framework

This section outlines the mathematical framework and numerical methods to simulate the interaction of shock waves with suspensions of particles that vary significantly in size. A ghost-point IBM approach is used to enforce the boundary conditions at the surface of large particles. Small particles are accounted for using a volume-filtered Euler–Lagrange approach. The framework is implemented within `jCODE` [15], a high-order multiphase flow solver.

2.3.1 Gas-phase description

The gas phase is governed by the volume-filtered viscous-compressible Navier–Stokes equations [121]. Small particles modify the gas-phase equations through a local volume fraction and interphase exchange source terms. Conservation of mass is expressed as

$$\frac{\partial \alpha\rho}{\partial t} + \nabla \cdot (\alpha\rho \boldsymbol{u}) = 0, \tag{2.1}$$

where α, ρ, and $\boldsymbol{u}$ are the gas-phase volume fraction, density and velocity, respectively. The momentum equation is given by

$$\frac{\partial \alpha \rho \boldsymbol{u}}{\partial t} + \nabla \cdot (\alpha \rho \boldsymbol{u} \otimes \boldsymbol{u}) = \alpha \nabla \cdot (\boldsymbol{\tau} - p\mathbb{I}) + \boldsymbol{\mathcal{F}}, \tag{2.2}$$

where $\mathbb{I}$ is the identity matrix, p is pressure, and $\boldsymbol{\tau}$ is the viscous stress tensor. The total energy (internal and kinetic) is governed by

$$\frac{\partial \alpha \rho E}{\partial t} + \nabla \cdot (\alpha \boldsymbol{u}\{\rho E + p\} - \alpha \boldsymbol{u} \cdot \boldsymbol{\tau}) = -\alpha \nabla \cdot \boldsymbol{q} \tag{2.3}$$

$$- (p\mathbb{I} - \boldsymbol{\tau}) : \nabla(\alpha_p \boldsymbol{u}_p) + \boldsymbol{u}_p \cdot \boldsymbol{\mathcal{F}} + \mathcal{Q}, \tag{2.4}$$

where $\boldsymbol{u}_p$ is the local velocity of small particles (in an Eulerian frame), and E is the total energy. $\boldsymbol{\mathcal{F}}$ and $\mathcal{Q}$ are sub-filtered interphase exchange terms that will be made explicit in § 2.4.1.

The non-dimensional viscous stress tensor is defined as

$$\boldsymbol{\tau} = \frac{\mu(\nabla \boldsymbol{u} + \nabla \boldsymbol{u}^T)}{Re_c} + \frac{\lambda \nabla \cdot \boldsymbol{u}}{Re_c}, \tag{2.5}$$

and the heat flux is $\boldsymbol{q} = -\mu \nabla T/(Re_c Pr)$ The thermodynamic pressure p and temperature T are given by the equation of state for an ideal gas in non-dimensional form as

$$p = (\gamma - 1)(\rho E - \rho \boldsymbol{u} \cdot \boldsymbol{u}/2); \qquad T = \frac{\gamma p}{(\gamma - 1)\rho}. \tag{2.6}$$

We briefly note that the pseudo-turbulent Reynolds stress (i.e., unresolved gas-phase velocity fluctuations induced by particles) should appear in the volume-filtered equations (2.2), (2.3) and pressure in (2.6) [121], but is neglected here since the majority of pseudo-turbulence is generated by wakes of large particles that are resolved in the present framework.

2.3.2 Discretization

The spatial derivatives are approximated using narrow-stencil finite difference operators D_i that satisfy summation by parts (SBP) property [129], given by

$$PD + (PD)^{\mathrm{T}} = \mathrm{diag}[-1, 0, \ldots, 0, 1]^{\mathrm{T}}, \tag{2.7}$$

where P is a symmetric positive-definite matrix and $D \in \mathbb{R}^{N\times N}$. This leads to $2s-$order centered-difference stencils at interior points and $s-$order accurate biased stencils near boundaries, with $s+1$ global accuracy. We employ a sixth-order formulation in the domain interior, and third-order, one-sided operators at the boundary. To evaluate second and mixed derivatives, first derivative operators are applied consecutively, necessitating the use of artificial dissipation to damp the highest wavenumber components supported by the grid. To this end, high-order accurate SBP dissipation operators are used to provide artificial dissipation [72].

Kinetic energy preservation is achieved through skew-symmetric type splitting of the inviscid fluxes [102] extended to include the effect of volume fraction from the small particles, which provides nonlinear stability at low Mach number. The convective fluxes appearing in Eqs. (2.1)–(2.3) are expressed in split form as

$$\nabla \cdot (\alpha\rho\boldsymbol{u}\varphi) = \frac{1}{2}\nabla \cdot (\alpha\rho\boldsymbol{u}\varphi) + \frac{1}{2}\varphi\nabla \cdot (\alpha\rho\boldsymbol{u}) + \frac{1}{2}\alpha\rho\boldsymbol{u} \cdot \nabla\varphi, \tag{2.8}$$

where φ is a generic transported scalar, which is unity for the continuity equation, u_j for the momentum equation, and $E + p/\rho$ for the total energy equation.

2.3.3 Boundary treatment

The SBP scheme is combined with the simultaneous approximation treatment (SAT) at the domain boundaries to facilitate an energy estimate [19, 92]. This is achieved by enforcing the

desired boundary conditions weakly by adding a penalty term to the right-hand-side of the governing equations. Non-reflecting characteristic boundary conditions and no-penetration free-slip walls are considered in the present work. Following the notation in [132, 133], the SAT treatment applied to the left boundary in one direction (with analogous treatment applied to the right boundary and the other two directions), is given by

$$\frac{\partial \boldsymbol{Q}}{\partial t} = R(\boldsymbol{Q}) + \sigma^I P^{-1} E_1 A^+ \left(\boldsymbol{Q} - \boldsymbol{Q}_b\right) - \sigma^V P^{-1} E_1 \left(\boldsymbol{F}^V - \boldsymbol{F}_b^V\right), \tag{2.9}$$

where $\boldsymbol{Q} = [\alpha\rho,\ \alpha\rho\boldsymbol{u},\ \alpha\rho E]^\mathsf{T}$ is the vector of conserved variables, $R(\boldsymbol{Q})$ is the right-hand side of the compressible flow equations, σ^I and σ^V are inviscid and viscous penalty parameters, respectively, and $\boldsymbol{F}^V$ contain the viscous fluxes appearing in Eqs. (2.1)–(2.3). $E_1 = [1,\ 0,\ \ldots,\ 0]^\mathsf{T}$ ensures the penalty is only applied at the domain boundary, and A^+ is the Roe matrix that selects the incoming characteristics. Setting $\sigma^I \leq -1/2$ and $\sigma^V = -1$ ensures numerical stability (with opposite signs for the right boundary) [132, 133].

The boundary data are supplied through a stationary target solution in the vector $\boldsymbol{Q}_b(\boldsymbol{x})$ and $\boldsymbol{F}_b^V(\boldsymbol{Q}_b)$. The specific form used to enforce far-field non-reflecting characteristic boundary conditions and no-penetration free-slip walls are given in [142]. In addition, an absorbing sponge region [42] is applied at the domain boundary to prevent unphysical acoustic reflections by adding a damping term of the form $\Psi(\boldsymbol{x})\left[\boldsymbol{Q}(\boldsymbol{x},t) - \boldsymbol{Q}_b(\boldsymbol{x})\right]$ to the right-hand side of the conservation equations.

2.3.4 Shock capturing

Localized artificial diffusivity is used as a means of shock capturing following the 'LAD-D2-0' formulation in Kawai et al. [57]. Here, the bulk viscosity and thermal conductivity are augmented according to $\mu_b = \mu_f + \mu^*$ and $\kappa = \kappa_f + \kappa^*$, where f subscripts and asterisks denote fluid and artificial transport coefficients, respectively. The artificial dissipation terms

take the form

$$\beta^* = C_\beta \overline{\rho f_{sw} |\nabla^4 \theta|} \Delta x^6, \quad \kappa^* = C_\kappa \overline{\frac{\rho c}{T} |\nabla^4 e|} \Delta x^5, \tag{2.10}$$

where Δx is the (uniform) local grid spacing, $\theta = \nabla \cdot \boldsymbol{u}$, $e = \frac{1}{\gamma - 1} \frac{p}{\rho}$, $C_\beta = 1$, and $C_\kappa = 0.01$. The overbar denotes a truncated 9-point Gaussian filter [25]. Fourth derivatives are approximated via a sixth-order compact (Padè) finite-difference operator [65]. To limit the artificial bulk viscosity to regions of high compression (shocks), we employ the sensor originally proposed by Ducros et al. [33] and later improved by Hendrickson et al. [49], given by $f_{sw} = \min\left(\frac{4}{3} H(-\theta) \times \frac{\theta^2}{\theta^2 + \Omega^2 + \epsilon}, 1\right)$, where H is the Heaviside function, $\epsilon - 10^{-32}$ is a small positive constant to prevent division by zero, and $\Omega = \max\left(|\nabla \times \boldsymbol{u}|, 0.05c/\Delta x\right)$ is a frequency scale that ensures the sensor goes to zero where vorticity is negligible.

The equations are advanced in time using a standard fourth-order Runge–Kutta scheme, resulting in the usual Courant–Friedrichs–Lewy (CFL) restrictions on the simulation time step Δt. The CFL is taken as the maximum between the acoustic CFL, $\mathrm{CFL}_a = \max\left(|\boldsymbol{u}| + c\right) \Delta t / \Delta x$ and the viscous CFL, $\mathrm{CFL}_v = \max\left(2\mu, \lambda, \kappa\right) \Delta t / \Delta x^2$. Note that in the presence of strong discontinuities, the artificial diffusion terms in λ and κ may induce a severe time-step restriction. To avoid introducing unphysical discontinuities near the interface of large particles, μ^* and κ^* are defined at every grid point within the domain (fluid and particle), but values inside the solid phase are not used when computing CFL_v.

2.4 Particle-phase equations

2.4.1 Treatment of small particles

We consider n 'small' particles with diameter d, mass m_p, volume v, and density ρ_p. The particle equations of motion are given by

$$\frac{\mathrm{d}\boldsymbol{x}_p^{(i)}}{\mathrm{d}t} = \boldsymbol{v}_p^{(i)}, \tag{2.11}$$

and,

$$m_p \frac{\mathrm{d}\boldsymbol{v}_p^{(i)}}{\mathrm{d}t} = v\nabla\cdot(p\mathbb{I}-\boldsymbol{\tau}) + \boldsymbol{F}_{\mathrm{drag}}^{(i)} + \boldsymbol{F}_{\mathrm{col}}^{(i)}, \tag{2.12}$$

where $\boldsymbol{x}_p^{(i)}$ and $\boldsymbol{v}_p^{(i)}$ are the position and translational velocity of particle i, respectively. The drag force is given by

$$\frac{\boldsymbol{F}_{\mathrm{drag}}^{(i)}}{m_p} = \frac{F_d}{\tau_p}\alpha(\boldsymbol{u}-\boldsymbol{v}_p^{(i)}), \tag{2.13}$$

where $\tau_p = \rho_p d^2/(18\mu)$ is the particle response time and $F_d = F_d(\alpha_p,\ \mathrm{Re}_p^{(i)},\ \mathrm{Ma}_p^{(i)})$ is the drag correlation of Osnes et. al. [94] that accounts for the local particle volume fraction $\alpha_p = 1-\alpha$, particle Reynolds number based on the slip velocity $\mathrm{Re}_p^{(i)} = \rho|\boldsymbol{u}-\boldsymbol{v}_p^{(i)}|d/\mu$, and particle Mach number $\mathrm{Ma}_p^{(i)} = |\boldsymbol{u}-\boldsymbol{v}_p^{(i)}|/c$. $\boldsymbol{F}_{\mathrm{col}}^{(i)}$ is the collision force that accounts for the contact between small and large particles and will be described in §. 2.5.

The rotational motion of small particles is given by

$$I_p \frac{\mathrm{d}\boldsymbol{\omega}_p^{(i)}}{\mathrm{d}t} = \boldsymbol{T}_h^{(i)} + \boldsymbol{T}_{\mathrm{col}}^{(i)}, \tag{2.14}$$

where $\boldsymbol{\omega}_p^{(i)}$ is the angular velocity of particle i and $I_p = m_p d^2/10$ is the particle's moment of inertia. The hydrodynamic torque is modeled according to $\boldsymbol{T}_h^{(i)} = \pi\mu d^3(\nabla\times\boldsymbol{u}/2-\boldsymbol{\omega}_p^{(i)})$. The collisional torque is $\boldsymbol{T}_{\mathrm{col}}^{(i)} = \sum_{j\neq i}(d\ \boldsymbol{n}\ \times \boldsymbol{F}_{\mathrm{col}}^{(j\to i)})/2$. The evolution of particle temperature is

$$m_p C_{p,p} \frac{\mathrm{d}T_p^{(i)}}{\mathrm{d}t} = Q^{(i)}, \tag{2.15}$$

where $T_p^{(i)}$ is the temperature of the i-th particle, $C_{p,p}$ is the particle heat capacity, and the interphase heat exchange term is given by

$$\frac{Q^{(i)}}{m_p C_{p,p}} = \frac{1}{3}\frac{C_p}{C_{p,p}}\frac{\mathrm{Nu}}{\mathrm{Pr}}\frac{1}{\tau_p}(T-T_p^{(i)}), \tag{2.16}$$

where Nu is the Nusselt number defined according to the correlation by Gunn [46].

Two-way coupling between the gas phase and small particles appears through the volume

fraction α, momentum exchange $\boldsymbol{\mathcal{F}}$, and heat exchange $\mathcal{Q}$ (refer to Eqs. (2.1), (2.2), (2.3)). The gas-phase volume fraction is computed according to

$$\alpha(\boldsymbol{x}) = 1 - \sum_{i=1}^{n} \mathcal{G}(|\boldsymbol{x} - \boldsymbol{x}_p^{(i)}|)\ v, \tag{2.17}$$

where $\mathcal{G}$ is a filter kernel taken to be an approximation of a Gaussian with characteristic size $\delta_f = 6d$. Similarly, interphase exchange due to drag and its corresponding work on the gas are given by

$$\boldsymbol{\mathcal{F}} = -\sum_{i=1}^{n} \mathcal{G}(|\boldsymbol{x} - \boldsymbol{x}_p^{(i)}|)\boldsymbol{F}_{\text{drag}}^{(i)}, \tag{2.18}$$

and

$$\boldsymbol{u}_p \cdot \boldsymbol{\mathcal{F}} = -\sum_{i=1}^{n} \mathcal{G}(|\boldsymbol{x} - \boldsymbol{x}_p^{(i)}|)\boldsymbol{v}_{\boldsymbol{p}}^{(i)} \cdot \boldsymbol{F}_{\text{drag}}^{(i)}. \tag{2.19}$$

Finally, the heat exchange term is transferred to the grid according to

$$\mathcal{Q} = -\sum_{i=1}^{n} \mathcal{G}(|\boldsymbol{x} - \boldsymbol{x}_p^{(i)}|)Q^{(i)}. \tag{2.20}$$

Eqs. (2.17)–(2.20) are solved efficiently following the two-step filtering approach of Capecelatro and Desjardins [16]. First, particle data is sent to the neighboring grid points via trilinear extrapolation. The solution is then smoothed using the same truncated 9-point Gaussian filter employed in shock capturing. Validation of the this current implementation of the volume-filtered Euler–Lagrange equations can be found in our previous work [98].

2.4.2 Treatment of large particles using IBM

The simulations contain N 'large' particles of diameter D, density ρ_p, and mass M_p with translational and rotational motion governed by

$$\frac{\mathrm{d}\boldsymbol{X}_p^{(i)}}{\mathrm{d}t} = \boldsymbol{V}_p^{(i)}, \tag{2.21}$$

$$M_p \frac{\mathrm{d}\boldsymbol{V}_p^{(i)}}{\mathrm{d}t} = \iint_{\partial \mathcal{V}_p^{(i)}} (-p\mathbb{I} + \boldsymbol{\tau}) \cdot \boldsymbol{n} \, \mathrm{d}A + \boldsymbol{F}_{\mathrm{col}}^{(i)}, \tag{2.22}$$

and

$$I_p \frac{\mathrm{d}\boldsymbol{\Omega}_p^{(i)}}{\mathrm{d}t} = \iint_{\partial \mathcal{V}_p^{(i)}} \boldsymbol{r} \times (\{-p\mathbb{I} + \boldsymbol{\tau}\} \cdot \boldsymbol{n}) \, \mathrm{d}A + \boldsymbol{T}_{\mathrm{col}}^{(i)}, \tag{2.23}$$

where $\boldsymbol{n}$ is the unit normal vector outward from the particle surface, $\partial \mathcal{V}_p^{(i)}$, and $\boldsymbol{r} = \boldsymbol{x} - \boldsymbol{X}_p^{(i)}$ is the position vector. Here, $\boldsymbol{X}_p^{(i)}$, $\boldsymbol{V}_p^{(i)}$, and $\boldsymbol{\Omega}_p^{(i)}$ are the position, translational, and rotational velocity corresponding to the i-th large particle, respectively. $\boldsymbol{F}_{\mathrm{col}}^{(i)}$ and $\boldsymbol{T}_{\mathrm{col}}^{(i)}$ represent the force and torque acting on the particle due to collisions, respectively, which will described in §. 2.5.

Following Mehta et al. [78], the hydrodynamic force and torque exerted by the gas phase acting on the i-th particle in Eqs. (2.22) and (2.23) can be calculated using the divergence theorem to transform the surface integral to a volume integrals as

$$\iint_{\partial \mathcal{V}_p^{(i)}} (-p\mathbb{I} + \boldsymbol{\tau}) \cdot \boldsymbol{n} \, \mathrm{d}A = \iiint_{\mathcal{V}_p^{(i)}} \nabla \cdot (-p\mathbb{I} + \boldsymbol{\tau}) \, \mathrm{d}V \approx \sum_{k \in \mathcal{V}_p^{(i)}} \nabla \cdot (-p\mathbb{I} + \boldsymbol{\tau}) \, \Delta V_k, \tag{2.24}$$

and

$$\begin{aligned} \iint_{\partial \mathcal{V}_p^{(i)}} \boldsymbol{r} \times (\{-p\mathbb{I} + \boldsymbol{\tau}\} \cdot \boldsymbol{n}) \, \mathrm{d}A &= \iiint_{\mathcal{V}_p^{(i)}} \nabla \cdot (\boldsymbol{r} \times \{-p\mathbb{I} + \boldsymbol{\tau}\}) \, \mathrm{d}V \\ &\approx \sum_{k \in \mathcal{V}_p^{(i)}} \nabla \cdot (\boldsymbol{r} \times \{-p\mathbb{I} + \boldsymbol{\tau}\}) \, \Delta V_k, \end{aligned} \tag{2.25}$$

where the volume integrals are approximated as summations over all k grid points located within the particle volume and $\Delta V_k = \Delta x^3$ is the local grid volume. Validation of this treatment of surface forces for computing shock-induced drag over a sphere can be found in our previous work [58, 120].

The particle equations of motion are solved simultaneously with the fluid equations via the same fourth-order Runge–Kutta time integration scheme. To avoid numerical instabilities, the simulation timestep is restricted such that the IBM interface cannot move more than

Δx per timestep, i.e., $\Delta t < \Delta x / \max(\boldsymbol{V}_p^{(i)})$.

No-slip, adiabatic boundary conditions are enforced at the surface of each large particle. The fluid velocity of an infinitesimal segment at the particle surface is

$$\boldsymbol{u}|_{\partial \mathcal{V}_p^{(i)}} = \boldsymbol{V}_p^{(i)} + \boldsymbol{\Omega}_p^{(i)} \times \boldsymbol{r}. \tag{2.26}$$

The adiabatic boundary condition is defined as

$$\left.\frac{\partial T}{\partial n}\right|_{\partial \mathcal{V}_p^{(i)}} = 0. \tag{2.27}$$

A Neumann boundary condition is applied to pressure by projecting the pressure gradient onto the surface-normal direction and ignoring the viscous terms [139], given by

$$\left.\frac{\partial p}{\partial n}\right|_{\partial \mathcal{V}_p^{(i)}} = -\rho \frac{\mathrm{d}\boldsymbol{V}_p^{(i)}}{\mathrm{d}t} \cdot \boldsymbol{n}. \tag{2.28}$$

The gas-phase density at the surface of the particle can then be obtained from the ideal gas law (2.6).

The boundary conditions are implemented on the Cartesian grid via a ghost-point IBM approach. At the beginning of each Runge–Kutta sub-step, a signed-distance levelset function is prescribed analytically according to

$$\mathbb{G}(\boldsymbol{x}, t) = \min_i \left(\|\boldsymbol{x} - \boldsymbol{X}_p^{(i)}\| - \frac{D}{2} \right). \tag{2.29}$$

A brute-force approach to solving (2.29) requires every grid point to loop through every large particle, resulting in $\mathcal{O}(N_g N)$ operations, where N_g is the number of grid points and N is the number of large particles. To accelerate the computation of the level set function, we leverage the underlying parallel decomposition. Specifically, we decompose the computational grid into multiple subdomains (each subdomain owned by a unique processor) using a three-

dimensional Cartesian topology. Each grid point only loops through particles residing within its subdomain and adjacent subdomains.

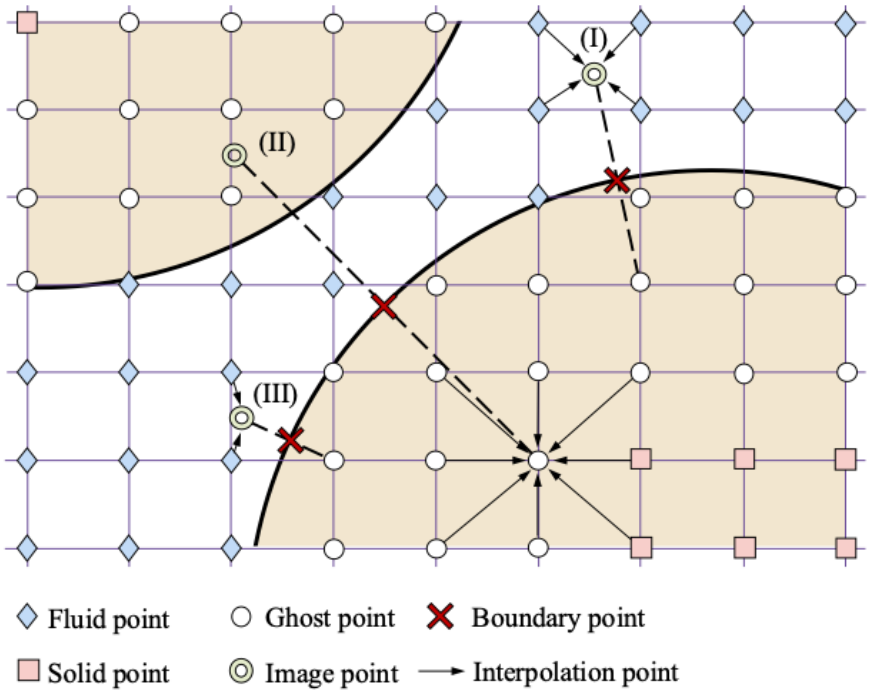

Figure 2.1: Schematic showing the ghost-point immersed boundary method highlighting the location of ghost points (GP), image points (IP), and boundary points (BP). Location of interpolation points for (I) IP located within the fluid away from the interface; (II) IP located within a neighboring particle; and (III) IP located near the particle's interface [127].

The levelset function is then used to identify grid points corresponding to ghost points (GP), image points (IP), and boundary points (BP) (see Fig. 2.1). Ghost points are defined as the grid points that reside within a large particle ($\mathbb{G} < 0$) whose stencil size extends to the fluid ($\mathbb{G} > 0$). Since we use a 6th-order centered finite difference scheme with a stencil size $n_{st} = 7$, grid points within $n_o = \lceil n_{st}/2 \rceil = 4$ points from the interface are tagged as ghost points. Thus, for any grid index i, j, k with $\mathbb{G}_{i,j,k} < 0$, a ghost point is identified when $\mathbb{G}_{i\pm n_o, j\pm n_o, k\pm n_o} > 0$. Image points are mirrored across the interface according to

$$\text{IP} = \text{GP} + 2l\boldsymbol{n}, \tag{2.30}$$

where $l = |\mathbb{G}|$ is the length between the ghost point and the surface of the immersed bound-

ary, so that the length between GP and its associated IP is $2l$, and $\boldsymbol{n} = \nabla\mathbb{G}/||\nabla\mathbb{G}||$ is the outward-facing normal.

Unlike ghost points that coincide with the fluid grid, image points do not. Here, we use the interpolation scheme proposed by Chaudhuri et al. [21] to evaluate fluid properties at image points. If an image point is located near the surface of the immersed boundary, grid points located within the solid are excluded from the interpolation weights, as depicted in scenario (III) in Fig. 2.1. If the image point resides with the volume of another large particle (scenario (II) in Fig. 2.1), the value at the ghost point is taken as an average of its surrounding grid points.

At the end of each Runge–Kutta sub-step, values at the ghost points are overwritten to enforce appropriate boundary conditions at the surface of each particle. The no-slip boundary condition (2.26) is discretized according to,

$$(\boldsymbol{u}_{\mathrm{GP}} + \boldsymbol{u}_{\mathrm{IP}})/2 = \boldsymbol{V}_p^{(i)} + \boldsymbol{\Omega}_p^{(i)} \times \boldsymbol{r}, \tag{2.31}$$

and thus the velocity at the ghost point is set to $\boldsymbol{u}_{\mathrm{GP}} = 2(\boldsymbol{V}_p^{(i)} + \boldsymbol{\Omega}_p^{(i)} \times \boldsymbol{r}) - \boldsymbol{u}_{\mathrm{IP}}$, where $\boldsymbol{u}_{\mathrm{IP}}$ is the gas-phase velocity interpolated to the image point. The adiabatic boundary condition (2.32) is given by

$$\frac{T_{\mathrm{GP}} - T_{\mathrm{IP}}}{2l} = 0, \tag{2.32}$$

and thus $T_{\mathrm{GP}} = T_{\mathrm{IP}}$. The pressure condition (2.34) is expressed as

$$\frac{p_{\mathrm{GP}} - p_{\mathrm{IP}}}{2l} = -\rho_{\mathrm{GP}} \frac{\mathrm{d}\boldsymbol{V}_p^{(i)}}{\mathrm{d}t} \cdot \boldsymbol{n}. \tag{2.33}$$

Rewriting ρ_{GP} in terms of temperature and pressure at the ghost point using the ideal gas law (2.6) and rearranging, yields

$$p_{\mathrm{GP}} = p_{\mathrm{IP}} \Bigg/ \left(1 - \frac{2l\gamma}{(\gamma - 1)T_{\mathrm{IP}}} \frac{\mathrm{d}\boldsymbol{V}_p^{(i)}}{\mathrm{d}t} \cdot \boldsymbol{n}\right). \tag{2.34}$$

When large particles are stationary, the pressure boundary condition simplifies to $p_{GP} = p_{IP}$, which represents a zero gradient condition.

The conserved variables at the ghost points, $[\alpha\rho, \alpha\rho\boldsymbol{u}, \alpha\rho E]_{GP}$, are then reconstructed using the local volume fraction α_{GP} along with Eq. (2.6). Since small particles cannot exist within large particles, $\alpha_{GP} = 1$ at most ghost points. However, $\alpha_{GP} < 1$ near the immersed boundary surface, where the filter size encroaches upon the large particle from the small particle's position, as described by Eq. (2.17). Failure to accurately reconstruct the conserved variables within the volume of large particles, using the local gas-phase volume fraction associated with small particles, can lead to spurious oscillations.

2.5 Collisions

Algorithm 1: Pseudocode for collision detection between N large particles

for $i = 1$ **to** N **do**
    for $j = i + 1$ **to** N **do**
        Compute overlap, δ_{ij}
        if $\delta_{ij} > 0$ **then**
            Compute forces on particle i: $\boldsymbol{f}^{\text{col}}_{n,i\to j}$ and $\boldsymbol{f}^{\text{col}}_{t,i\to j}$ via Eqs. (2.35) and (2.37)
            Compute forces on particle j: $\boldsymbol{f}^{\text{col}}_{n,j\to i} = -\boldsymbol{f}^{\text{col}}_{n,i\to j}$ and $\boldsymbol{f}^{\text{col}}_{t,j\to i} = -\boldsymbol{f}^{\text{col}}_{t,i\to j}$

Algorithm 2: Pseudocode for collision detection between n small particles and N large particles

for $j = 1$ **to** N **do**
    $ID(\boldsymbol{x}) = j$ **if** $\|\boldsymbol{x} - \boldsymbol{X}_p^{(j)}\| \leq D/2 + \Delta x$
for $i = 1$ **to** n **do**
    Interpolate $\mathbb{G}(\boldsymbol{x})$ to particle i
    if $|\mathbb{G}(\boldsymbol{x})| < d/2$ **then**
        Interpolate $ID(\boldsymbol{x})$ to particle i
        Compute forces on particle i: $\boldsymbol{f}^{\text{col}}_{n,i\to j}$ and $\boldsymbol{f}^{\text{col}}_{t,i\to j}$ via Eqs. (2.35) and (2.37)
        Compute forces on particle j: $\boldsymbol{f}^{\text{col}}_{n,j\to i} = -\boldsymbol{f}^{\text{col}}_{n,i\to j}$ and $\boldsymbol{f}^{\text{col}}_{t,j\to i} = -\boldsymbol{f}^{\text{col}}_{t,i\to j}$

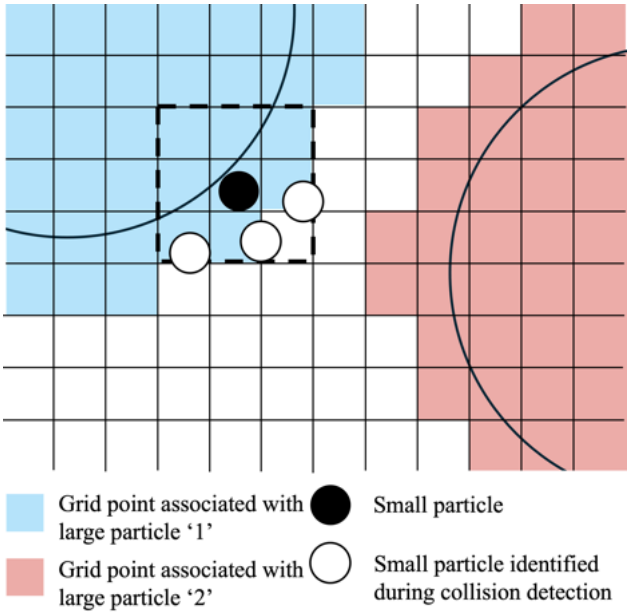

Figure 2.2: Schematic showing the collision detection scheme between a small particle (black) and other small particles (white) and a large particle (blue) [127]

Particle collisions are handled using a soft-sphere collision model originally proposed by Cundall and Strack [27]. On contact between two particles i and j, a repulsive force is created as,

$$\boldsymbol{f}_{n,j\to i}^{\text{col}} = \begin{cases} -k\delta_{ij}\boldsymbol{n}_{ij} - \eta\boldsymbol{u}_{ij,n} & \text{if } \delta_{ij} > 0 \\ 0 & \text{else,} \end{cases} \tag{2.35}$$

where k and η are the spring stiffness and damping parameter, respectively, and $\delta_{ij} = r_i + r_j - d_{ij}$ is the overlap. Here, d_{ij} is the distance between particle centers and r_i and r_j are the particle radii ($r_i = d/2$ for small particles and $r_i = D/2$ for large particles). $\boldsymbol{u}_{ij,n} = (\boldsymbol{u}_{ij} \cdot \boldsymbol{n}_{ij})\boldsymbol{n}_{ij}$ is the normal relative velocity, where $\boldsymbol{n}_{ij}$ is the unit normal vector from particle i to particle j and $\boldsymbol{u}_{ij} = \boldsymbol{u}_i - \boldsymbol{u}_j$ with $\boldsymbol{u}_i = \boldsymbol{v}_p^{(i)}$ for small particles and $\boldsymbol{u}_i = \boldsymbol{V}_p^{(i)}$ for large particles. The damping parameter is a function of a coefficient of restitution $0 < e < 1$ and an effective mass $m_{ij} = (1/m_i + 1/m_j)^{-1}$, expressed as

$$\eta = -2\ln e \frac{\sqrt{m_{ij}k}}{\pi^2 + (\ln e)^2}. \tag{2.36}$$

The spring stiffness is related to the collision time τ_{col} according to $k = m_{ij}/\tau_{\text{col}}^2(\pi^2 + \ln e^2)$. Following [16], we choose a value of $\tau_{\text{col}} = 20\Delta t$ to sufficiently resolve collisions. Tangential collisions are accounted for via Coulomb's law of friction, given by

$$\boldsymbol{f}_{t,j\to i}^{\text{col}} = -\mu_f |\boldsymbol{f}_{n,j\to i}^{\text{col}}| \boldsymbol{t}_{ij}, \tag{2.37}$$

where $\boldsymbol{u}_{ij,t} = \boldsymbol{u}_{ij} - \boldsymbol{u}_{ij,n}$ is the tangential velocity, μ_f is the coefficient of friction, and the tangential unit vector is $\boldsymbol{t}_{ij} = \boldsymbol{u}_{ij,t}/|\boldsymbol{u}_{ij,t}|$. A coefficient of friction of $\mu_f = 0.1$ and a coefficient of restitution of $e = 0.85$ are used in this study. Finally, $\boldsymbol{F}_{\text{col}}^{(i)}$ from Eq. (2.12) is computed by adding the contribution due to the normal and tangential contact forces as $\boldsymbol{F}_{\text{col}}^{(i)} = \sum_j (\boldsymbol{f}_{n,j\to i}^{\text{col}} + \boldsymbol{f}_{t,j\to i}^{\text{col}})$.

A brute force approach for contact detection involves each particle looping through every other particle, resulting in $\mathcal{O}\left((N+n)^2\right)$ operations, which is prohibitively expensive. To avoid this, collision detection between two small particles is handled using an efficient nearest-neighbor detection algorithm that utilizes the underlying gas-phase mesh [16]. An array containing the number of particles residing within each grid cell and their indices are stored at the beginning of each time step. Then, small particles check overlap with other small particles in adjacent cells (see Fig. 2.2). This results in $\mathcal{O}(n \log n)$ computations. More details on the algorithm and parallel implementation can be found in [16].

To address collisions between large particles, we cannot employ the same nearest-neighbor detection method used for small particles since large particles span multiple grid points and may also span multiple processors. To avoid $\mathcal{O}(N^2)$ operations, a straightforward approach is considered where each large particle only iterates through other large particles it hasn't yet contacted. This results in $\mathcal{O}(N \log N)$ operations. Since large particles are few hundreds in number and all processors have access to IBM information, two simple loops are sufficient to detect contact (see Algorithm 1).

Collision detection between large and small particles requires special care. We propose an efficient solution that scales like $\mathcal{O}(n + N)$ in Algorithm 2. At the beginning of each time step, large particles transfer a unique ID to the grid points in its vicinity, extending Δx beyond their diameter (see Fig. 2.2). During the collision routine, the signed-distance levelset, $\mathbb{G}$, is interpolated to the location of each small particle to determine their distance with large particles. If overlap is detected, the ID is interpolated from the grid to the small particle. Consequently, the small particle acquires information about which large particle it is in contact with, and collisions are handled per Eqs. (2.35) and (2.37).

2.6 Conclusion

In this chapter, we presented a numerical framework that couples Lagrangian particle tracking with a ghost-point IBM to simulate bidisperse particle-laden compressible flows with large size ratios. The gas phase is governed by the volume- filtered Navier-Stokes equations, discretized using a high-order, energy-stable finite difference scheme. No-slip, adiabatic boundary conditions are enforced at the surfaces of large particles, while an Euler-Lagrange method is applied to small particles, with interphase coupling handled via drag and heat transfer. Collisions are accounted for using a soft-sphere model. An efficient contact detection algorithm is proposed for collisions between small and large particles that makes use of the underlying signed-distance levelset function.

CHAPTER 3

Turbulence Transport During Shock-Particle Interactions

Note: A version of this chapter is under production for publication in the *Journal of Fluid Mechanics* [128]. Data and figures have been used with all co-authors' consent.

3.1 Abstract

This study employs three-dimensional particle-resolved simulations of planar shocks passing through a suspension of stationary solid particles to study wake-induced gas-phase velocity fluctuations, termed pseudo-turbulence. Strong coupling through interphase momentum and energy exchange generates unsteady wakes and shocklets in the interstitial space between particles. A Helmholtz decomposition of the velocity field shows that the majority of pseudo-turbulence is contained in the solenoidal component from particle wakes, whereas the dilatational component corresponds to the downstream edge of the particle curtain where the flow chokes. One-dimensional phase-averaged statistics of pseudo-turbulent kinetic energy (PTKE) are quantified at various stages of flow development. Reduction in PTKE is observed with increasing shock Mach number due to decreased production, consistent with single-phase compressible turbulence. The anisotropy in Reynolds stresses is found to be relatively constant through the curtain and consistent over all the conditions simulated. Analysis of the budget of PTKE shows that the majority of turbulence is produced through

drag and balanced by viscous dissipation. The energy spectra of the streamwise gas-phase velocity fluctuations reveal an inertial subrange that begins at the mean interparticle spacing and decays with a power law of $-5/3$ and steepens to -3 at scales much smaller than the particle diameter. A two-equation model is proposed for PTKE and its dissipation. The model is implemented within a hyperbolic Eulerian-based two-fluid model and shows excellent agreement with the particle-resolved simulations.

3.2 Introduction

High-speed flows through particulate media occur in diverse applications, such as detonation blasts [151], volcanic eruptions [23, 69], coal-dust explosions [116, 152], pulsed-detonation engines [20, 113], and plume-surface interactions during interplanetary landings [14, 90, 103]. In these examples, turbulence plays a crucial role in governing processes like reactant mixing and particle dispersion. However, the nature of this turbulence is distinct from both single-phase compressible turbulence and low-speed multiphase turbulence, posing a challenge to the accuracy of existing models.

Compressibility effects in turbulent flows are often characterized using the turbulent Mach number [56, 114]. For values of $M_t \leq 0.3$, large scale separation exists between acoustics and turbulence. This results in a nearly incompressible flow called the quasi-isentropic regime. For higher values of M_t (i.e. $0.3 < M_t \leq 0.6$), dilatational effects are significant, leading to a nonlinear subsonic regime. The flows considered in the present study predominantly fall within this regime.

Since the 1970s, numerous studies have investigated the role of compressibility in the development of turbulent mixing layers and the generation of turbulent kinetic energy [10, 13, 118]. Early work by Sarkar et al. [118] and Zeman [150] examined the effects of dilatational dissipation, ϵ_d, finding that its increase with M_t leads to a reduction in turbulent kinetic energy, thereby decreasing turbulent mixing. They suggested that the suppression of growth

rate is linked to increased ϵ_d due to shocklets. They developed a mathematical model to incorporate this effect into Reynolds stress closure models. However, Sarkar [117] later showed, using direct numerical simulations of turbulent homogeneous shear flow, that the reduction of turbulent kinetic energy is primarily due to decreased turbulence production, rather than directly caused by dilatational dissipation. Subsequent studies by Vreman [143] and Pantano & Sarkar [97] corroborated this finding, showing that dilatational dissipation is negligible. Instead, the reduced growth rate of turbulence is linked to diminished pressure fluctuations and, consequently, lower turbulence production resulting from a reduction in the pressure-strain term.

Kida & Orszag[59] were among the first to analyze the kinetic energy spectrum in forced compressible turbulence, observing that its scaling is largely independent of Mach number. Donzis & Jagannathan [30] also found that the turbulent kinetic energy spectrum in compressible isotropic turbulence follows a $-5/3$ power law in the inertial range for $0.1 \leq M_t \leq 0.6$, consistent with the classical Kolmogorov scaling for incompressible flows [60]. Further insights into compressibility scaling emerge from a Helmholtz decomposition of the velocity field $\boldsymbol{u}$ into its solenoidal component $\boldsymbol{u}_s$ and dilatational component $\boldsymbol{u}_d$ [30, 59, 115, 146, 147]. Compressibility effects are typically attributed to $\boldsymbol{u}_d$, and both Donzis & Jagannathan [30] and Wang et al. [146] observed that the majority of turbulent kinetic energy resides in the solenoidal component, with $\boldsymbol{u}_d$ increasing with M_t. However, all of these studies have focused on single-phase compressible turbulent flows in the absence of particles.

In multiphase flows, interphase coupling introduces additional complexity that significantly influences energy transfer and turbulence characteristics. Fluid velocity fluctuations induced by particle wakes are referred to as pseudo-turbulence [63, 75], a term also applied to bubble-induced turbulence (BIT) in liquid flows [111]. Lance & Bataille [63] first demonstrated that a homogeneous swarm of bubbles generates pseudo-turbulence with a spectral subrange exhibiting a -3 power law. They showed that at statistically steady state, this

spectral scaling results from a balance between viscous dissipation and energy production due to drag forces from rising bubbles. Similar scaling has since been observed in other bubbly flows [82–84, 111]. Subsequent experimental studies coupling BIT with shear-induced turbulence have found that the spectra of liquid velocity fluctuations follow a -3 scaling at small wave numbers, transitioning to a $-5/3$ scaling at higher wave numbers, suggesting a single-phase signature is preserved at the smallest scales [111]. Numerical simulations of gas–particle turbulent channel flow reveal that two-way coupling between the phases results in reduction in fluid-phase turbulent kinetic energy at the scale of individual particles, while a broadband reduction over all scales is observed at moderate to high mass loading [17].

Over the past few decades, turbulence models have evolved to incorporate the effects of particles [39, 71, 138]. A production term must be included to account for generation of turbulence through drag. A dissipation time scale is often employed based on the relative velocity between the phases (u_r) and particle diameter (d_p), given by $\tau = d_p/u_r$. The use of two-equation transport models for gas–solid flows dates back to the work of [38], who derived a rigorous set of equations for dilute concentrations of particles in incompressible flow using a two-fluid approach. Since then, models have been proposed for denser regimes in shear turbulence [70]. Crowe et al. [26] provided a review of numerical models for turbulent kinetic energy in two-phase flows. However, these models are limited to *intrinsic turbulence* whereby the carrier-phase turbulence would exist even in the absence of particles, as opposed to pseudo-turbulence that is entirely generated by the particle phase. Mehrabadi et al. [75] recently developed an algebraic model for pseudo-turbulent kinetic energy (PTKE) based on particle-resolved simulation data that depends on the slip Reynolds number and particle volume fraction. A limitation of algebraic models is that PTKE can only be predicted in regions of finite volume fraction. In cases where turbulence is generated within a suspension of particles and advects downstream into the surrounding gas, transport equations for PTKE are more appropriate [121].

Particle-laden compressible flows challenge numerical models due to the strong coupling

between shock waves, particles, and turbulence over a wide range of scales. Using particle-resolved simulations of compressible homogeneous flows past random arrays of particles, Khalloufi & Capecelatro [58] found that both M_t and PTKE increase with particle volume fraction for a fixed free-stream Mach number. Experimental and numerical studies of particle-laden underexpanded jets have demonstrated significant modification of shock structures due to the two-way coupling between the gas and particles even at low volume fractions where one-way coupling would be deemed appropriate for single-phase flow [98, 123]. Two-dimensional particle-resolved simulations of shock–particle curtain interactions revealed PTKE magnitudes comparable to the resolved kinetic energy [50, 105]. In three-dimensional inviscid simulations, Mehta et al. [79] reported velocity fluctuations reaching up to 50% of the kinetic energy based on the mean flow, with increasing velocity fluctuations observed at higher shock Mach numbers, M_s, and particle volume fractions, Φ_p. It should be noted that shock-driven multiphase flows in radial configurations are prone to instabilities not captured in the planar geometries considered in the aforementioned studies [73, 85]. However, because turbulence transport occurs on much shorter time scales than particle dispersal or instability growth, such effects are not relevant to the present focus on gas-phase turbulence.

Models for PTKE in compressible gas–particle flows have only recently begun to emerge. Osnes et al. [95] proposed an algebraic model for PTKE based on particle-resolved simulations of shock–particle interactions that depends on the mean flow speed and particle volume fraction. Shallcross et al. [121] proposed a one-equation model for PTKE containing a production term due to drag and an algebraic closure for dissipation. The dissipation model employs a time scale based on the particle diameter and local slip velocity–consistent with that used in BIT models [71]–augmented with a blending function to account for regions devoid of particles. However, the results were found to be highly sensitive to the closure applied to dissipation, limiting its applicability.

Building on these efforts, the present study aims to advance understanding of turbulence transport in compressible gas–particle flows, particularly at moderate volume fractions and

Mach numbers. The paper is organized as follows. In § 3.3, the simulation configuration is presented. Simulation results are provided in § 3.4, starting with a qualitative assessment of the flow, followed by one-dimensional phase-averaged statistics of the gas-phase velocity. The budget of PTKE is presented next, revealing key production and dissipation mechanisms. The energy spectra within the particle curtain is then presented and separate contributions from solenoidal and dilatational components highlight the sources of PTKE. In § 3.5, a two-equation turbulence model for PTKE and its dissipation is proposed and implemented within a hyperbolic two-fluid model. Results from § 3.4 are used to guide closure. An a-posteriori analysis is performed and first- and second-order statistics are compared.

3.3 Simulation setup and methods

3.3.1 Flow configuration

To isolate shock–particle–turbulence interactions, we perform three-dimensional, particle-resolved simulations of a planar shock propagating through a suspension of stationary, monodisperse particles. The assumption of frozen particles is justified, as the acoustic time scale is several orders of magnitude shorter than the particle response time for the high density ratios ($\rho_p/\rho > 10^3$) typical of gas–solid flows [67]. The simulations are designed to emulate the multiphase shock-tube experiments of Wagner et al. [144]. Figure 3.1 shows a volume rendering of the gas-phase velocity magnitude within the simulation domain at a moment when the shock has advanced significantly beyond the curtain and exited the domain. The velocity increases across the particle curtain with maximum values at the downstream curtain edge where the flow chokes due to the sudden change in volume fraction.

Particles with diameter $D = 115$ μm and density $\rho_p = 2520$ kg/m^3 are randomly distributed within a curtain of thickness $L = 2$ mm ($L = 17.4D$). A minimum of two grid points is maintained between particle surfaces. A planar shock is initially placed at a non-dimensional length of $x = 5.5D$ with the flow direction parallel to the x-axis. The

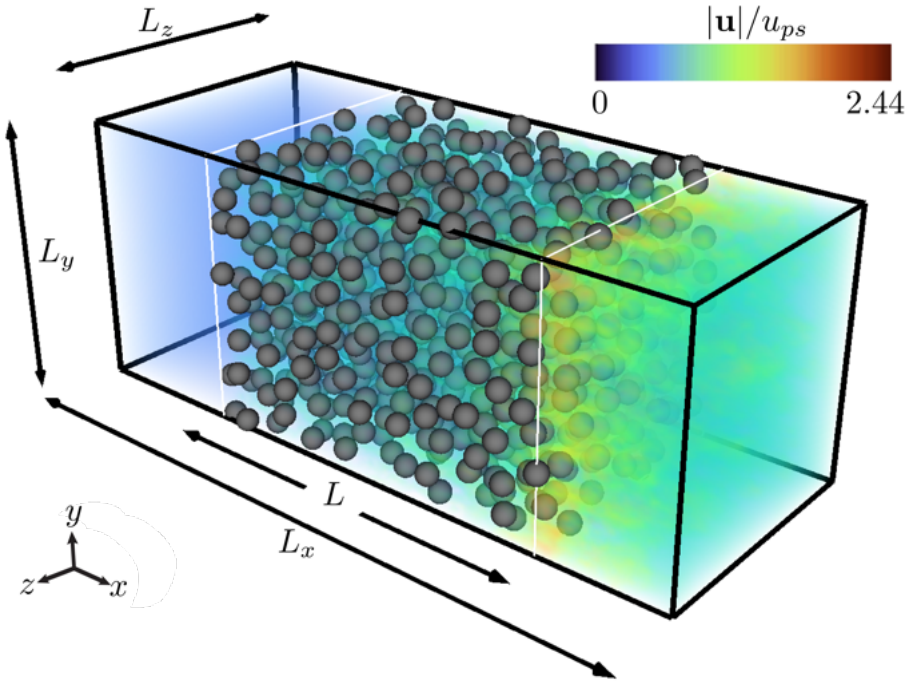

Figure 3.1: The simulation domain showing particle position and a volume rendering of the gas-phase velocity magnitude after the shock has passed the curtain ($t/\tau_L = 2$) with $\Phi_p = 0.2$ and $M_s = 1.66$.

upstream edge of the curtain is placed at $x = 7D$. Periodic boundary conditions are imposed in the two spanwise (y and z) directions. The domain size for all but one case is $[L_x \times L_y \times L_z] = [30 \times 12 \times 12]D$. L_y and L_z were chosen based on a domain size independence study summarized in The domain is discretized with uniform grid spacing $\Delta x = D/40$, corresponding to $[1201 \times 480 \times 480]$ grid points.

The pre-shock gas-phase density is $\rho_\infty = 0.987$ kg/m^3, pressure $P_\infty = 82.7$ kPa, sound speed $c_\infty = 343$ m/s and velocity $u_\infty = 0$ m/s. Post-shock properties, denoted by the subscript ps, are obtained via the Rankine–Hugoniot conditions. The shock Mach number is defined as $M_s = u_s/c_\infty$, where u_s is the shock speed. A reference time-scale based on the distance (in terms of particle curtain length) that the shock travels is defined as $\tau_L = L/u_s$. The particle Reynolds number based on post-shock properties is defined as $\mathrm{Re}_{ps} = \rho_{ps} u_{ps} D/\mu_{ps}$, where μ_{ps} is the gas-phase viscosity at temperature T_{ps}. The number of particles N_p within the curtain is determined from the average volume fraction, Φ_p. A summary of

the cases considered in this study is given in Table 3.1. Cases $1-9$ represent different combinations of M_s and Φ_p. Case 10 exhibits a longer domain length to study turbulence transport downstream of the particle curtain.

Case No.	M_s	Φ_p	Re_{ps}	N_p	L_x/D	L_y/D
1	1.2	0.1	813	467	30	12
2	1.2	0.2	813	935	30	12
3	1.2	0.3	813	1402	30	12
4	1.66	0.1	3251	467	30	12
5	1.66	0.2	3251	935	30	12
6	1.66	0.3	3251	1402	30	12
7	2.1	0.1	5591	467	30	12
8	2.1	0.2	5591	935	30	12
9	2.1	0.3	5591	1402	30	12
10	1.66	0.3	3251	1402	58	12

Table 3.1: Parameters for the various runs used in this study.

3.3.2 Numerics

The simulations are performed using the compressible multiphase flow solver `jCODE` [15]. The viscous compressible Navier–Stokes equations govern the gas-phase physics, so essentially setting $\alpha = 1$ in § 2.3.1 and the interphase terms to zero gives the microscale equations. Chapter 2 also provides more information on the discretization, boundary treatment, and shock capturing. The particles in this study, are simulated as monodisperse spheres using the immersed boundary method explained in § 2.4.2. No-slip, adiabatic boundary conditions are enforced at the particle surface. The only difference here is that the particles are considered stationary, so equations of motion for IBM particles are neglected. The equations are advanced in time using a standard fourth-order Runge–Kutta scheme, with a constant Courant–Friedrichs–Lewy (CFL) number of 0.8. The framework was validated in our previous study [58], demonstrating that 40 grid points across the particle diameter is sufficient to capture drag and PTKE. An assessment of the domain size and sensitivity to random particle placement is reported in the Appendix of this Chapter.

3.4 Results

3.4.1 Flow visualization

Instantaneous snapshots of the flow field corresponding to Case 5 ($M_s = 1.66, \Phi_p = 0.2$) at $t/\tau_L = 0.5$, 1, and 2 are presented in Fig. 3.2. A two-dimensional slice in the $x-y$ plane shows the local gas-phase Mach number and numerical Schlieren in the vicinity of the particles. The incident shock travels in the positive x direction and impinges the particle curtain located at x_0 at time $t = 0$. Upon impact, the shock splits into a weaker transmitted shock that penetrates the curtain, as shown in Fig. 3.2(a). At the upstream edge of the curtain, the arrival of the shock generates multiple shocklets at the surface of each particle, which coalesce into a reflected shock wave. Shock–particle interactions are seen to generate significant fluctuations in the gas-phase velocity. Contour lines of $M = 1$ (shown in purple) demarcate local supersonic regions. In Fig. 3.2(b), the shock has nearly reached the downstream curtain edge, and the local supersonic regions move downstream with the flow. Figure 3.2(c) shows that the flow has stabilized with both the transmitted and reflected shocks having exited the domain boundaries. The particles restrict the area of the transmitted shock, causing the gas phase to choke near the downstream edge of the curtain due to the abrupt change in volume fraction, followed by a supersonic expansion. Velocity fluctuations induced by the particles advect downstream from the curtain and dissipate, akin to grid-generated turbulence.

3.4.2 Averaging equations

The flows under consideration are unsteady and statistically homogeneous in the two spanwise directions. Averaged quantities depend solely on one spatial dimension (x) and time. Due to the presence of particles and gas-phase density variations, special attention must be given to the averaging process. To facilitate statistical phase-averaging, an indicator function

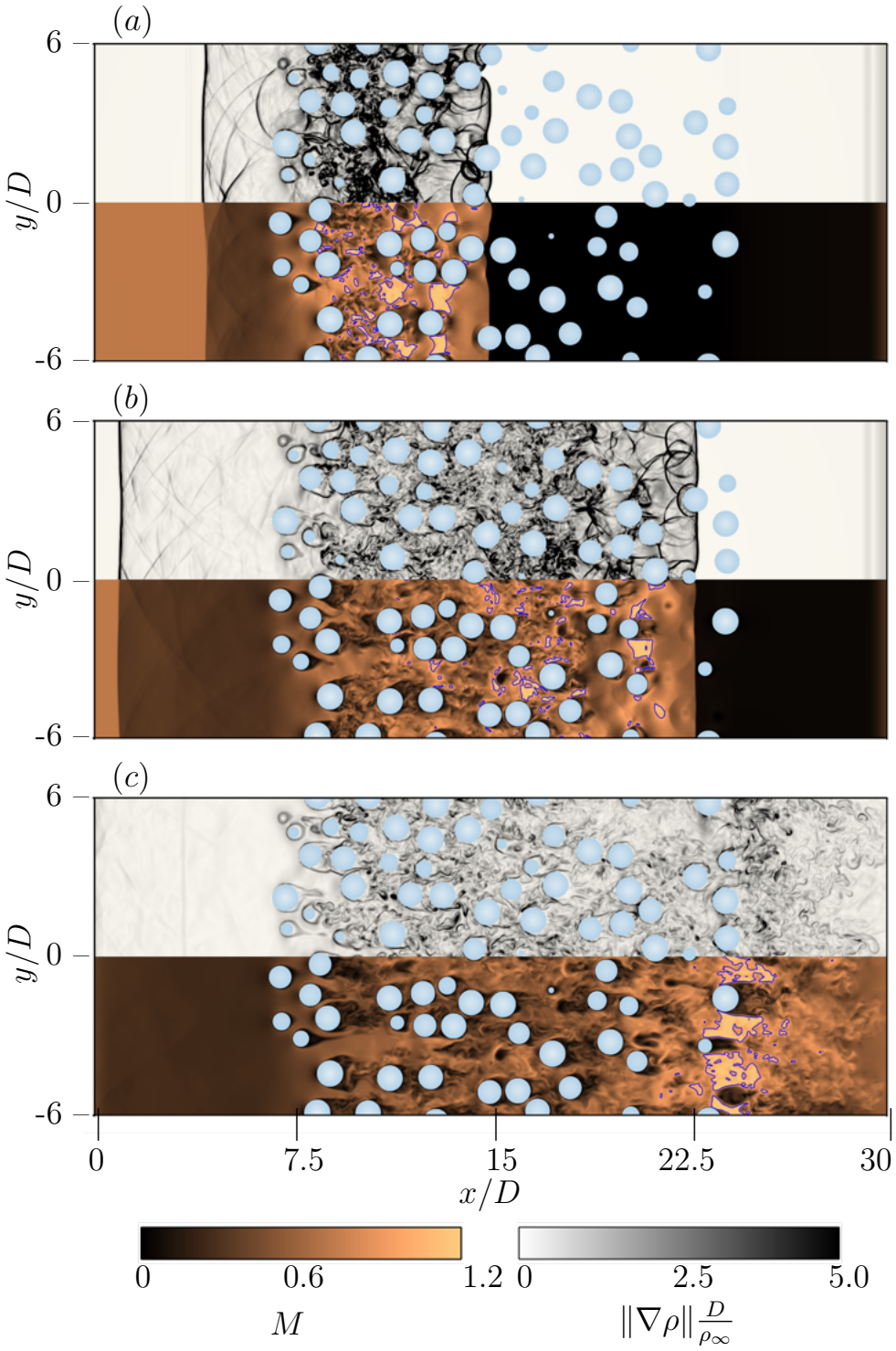

Figure 3.2: Two-dimensional planes showing Schlieren (top half of each plot) and local Mach number $M = \|\boldsymbol{u}\|/c$ (bottom half) at (a) $t/\tau_L = 0.5$, (b) $t/\tau_L = 1$ and (c) $t/\tau_L = 2$ for $M_s = 1.66$ and $\Phi_p = 0.2$. Contour lines of $M = 1$ shown in purple. Blue circles depict particle cross sections.

is defined as

$$\mathcal{I}(\boldsymbol{x}) = \begin{cases} 1 & \text{if } \boldsymbol{x} \in \text{gas phase}, \\ 0 & \text{if } \boldsymbol{x} \in \text{particle}. \end{cases} \tag{3.1}$$

Spatial averages are taken as integrals over $y-z$ slices. The integration of the indicator function yields a volume fraction α (or area fraction in this case) that depends solely on x (time is omitted since the particles being stationary), given by

$$\alpha_g(x) = \langle \mathcal{I} \rangle \equiv \frac{1}{L_y L_z} \int_{L_y} \int_{L_z} \mathcal{I} \, \mathrm{d}y \, \mathrm{d}z, \tag{3.2}$$

where angled brackets denote a spatial average. Two other important averaging operations that will be used throughout this study are phase averages and density-weighted (Favre) averages. If $\psi(\boldsymbol{x}, t)$ represents a random field variable, these averages are defined as

$$\begin{aligned} &\text{Spatial-average: } \langle \psi \rangle(x,t) \equiv \frac{1}{L_y L_z} \int_{L_y} \int_{L_z} \psi \, \mathrm{d}y \, \mathrm{d}z, \\ &\text{Phase-average: } \overline{\psi}(x,t) \equiv \frac{\langle \mathcal{I}\psi \rangle}{\langle \mathcal{I} \rangle} \equiv \frac{\langle \mathcal{I}\psi \rangle}{\alpha_g}, \\ &\text{Favre-average: } \widetilde{\psi}(x,t) \equiv \frac{\langle \mathcal{I}\rho\psi \rangle}{\langle \mathcal{I}\rho \rangle} \equiv \frac{\overline{\rho\psi}}{\overline{\rho}}. \end{aligned} \tag{3.3}$$

Spatial averages and phase averages are related via $\langle \mathcal{I}\psi \rangle = \alpha_g \overline{\psi}$ and similarly $\overline{\rho\psi} = \overline{\rho}\widetilde{\psi}$. A field variable can be decomposed into its phase-average and a fluctuating quantity as $\psi = \overline{\psi} + \psi'$. Similarly, the Favre decomposition is $\psi = \widetilde{\psi} + \psi''$.

3.4.3 Mean velocity, fluctuations and anisotropy

The Favre-averaged gas-phase velocity, $\widetilde{u}$, as a function of the streamwise direction at three different time instances ($t/\tau_L = 0.5$, 1, and 2) is shown in Fig. 3.3. The abrupt drop in velocity observed at early times ($t/\tau_L = 0.5$ and 1) marks the location of the transmitted shock. The flow decelerates significantly as it approaches the particle curtain due to drag, with greater reduction in velocity relative to the post-shock velocity at higher volume frac-

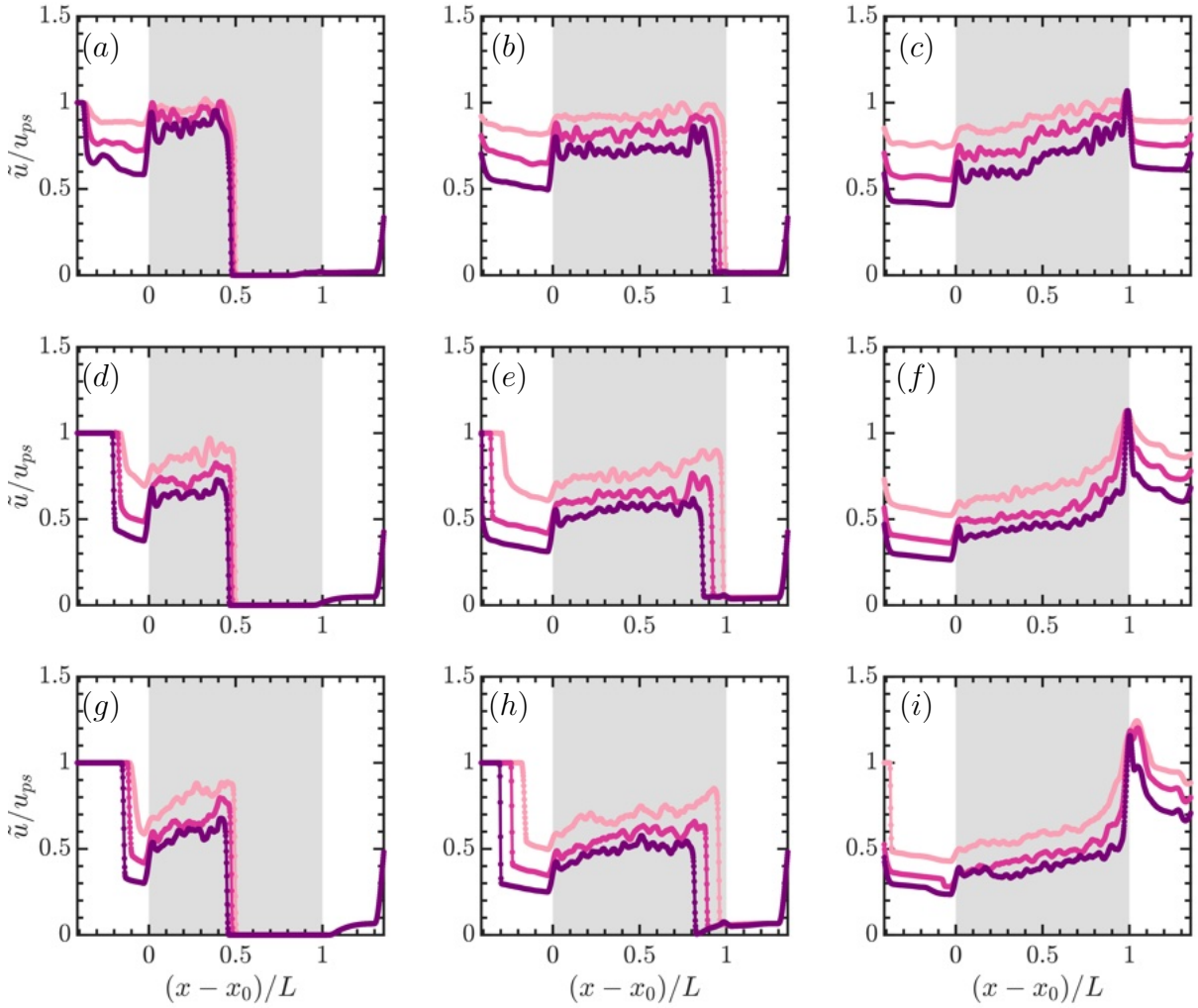

Figure 3.3: Mean gas-phase velocity profiles. Darker lines indicate higher volume fractions: $\Phi_p = 0.1$ (light pink), $\Phi_p = 0.2$ (pink), $\Phi_p = 0.3$ (purple). $t/\tau_L = 0.5$ (left), $t/\tau_L = 1$ (middle) and $t/\tau_L = 2$ (right). (a)–(c) $M_s = 1.2$, (d)–(f) $M_s = 1.66$, (g)–(i) $M_s = 2.1$. The gray-shaded region indicates the location of the particle curtain.

tions. The flow then accelerates as it traverses the curtain. At the latest time ($t/\tau_L = 2$), a sharp increase in $\widetilde{u}$ at the downstream edge of the curtain is seen across all cases, indicating a region of choked flow transitioning to supersonic velocities. Similar trends in the velocity field have been reported previously [e.g. 80, 95, 136]. Mehta et al.[80] obtained an analytical solution of the Riemann problem for a duct with a sudden change in cross-sectional area as a simpler means of predicting the flow through a particle curtain. The solution was found to compare well with inviscid simulations of shock–particle interactions, though it is unable to predict the choking behavior leading to supersonic velocities observed here.

The amplitude and speed of the reflected shocks, indicated by the abrupt increase in velocity upstream of the particle curtain, increase with Φ_p. The transmitted shock travels faster through the curtain at lower Φ_p where the flow is less obstructed. For a given volume fraction, the magnitude of $\widetilde{u}$ decreases with increasing M_s, and the flow-expansion region at the downstream edge rises sharply with increasing M_s.

The root-mean-square (rms) gas-phase velocity fluctuations in the streamwise direction is defined as $u^2_{\text{rms}} = \widetilde{u''u''}$. Due to symmetry, the spanwise fluctuations are taken as $v^2_{\text{rms}} = (\widetilde{v''v''} + \widetilde{w''w''})/2$. Figure 3.4 shows these components at $t/\tau_L = 1$ and 2. All values are normalized by the post-shock kinetic energy, u^2_{ps}. Velocity fluctuations originate almost immediately within the particle curtain. The magnitude of the streamwise fluctuations are nearly twice the spanwise components. The fluctuations are higher at initial times, shortly after the shock passes over the particles. The maximum velocity fluctuations occur at the downstream edge where the flow chokes. Overall, the fluctuations decrease in magnitude with increasing M_s. This reduction can be attributed to an increase in compressibility effects with higher M_s. The precise dissipation mechanisms will be quantified in § 3.4.4, where individual terms of the PTKE budget are reported.

It is interesting to note that the normalized fluctuations are nearly invariant with volume fraction except for the lowest shock Mach number case at early times (see Fig. 3.4(a)). Previous studies by Mehta et al. [79] observed an increase in velocity fluctuations with Φ_p.

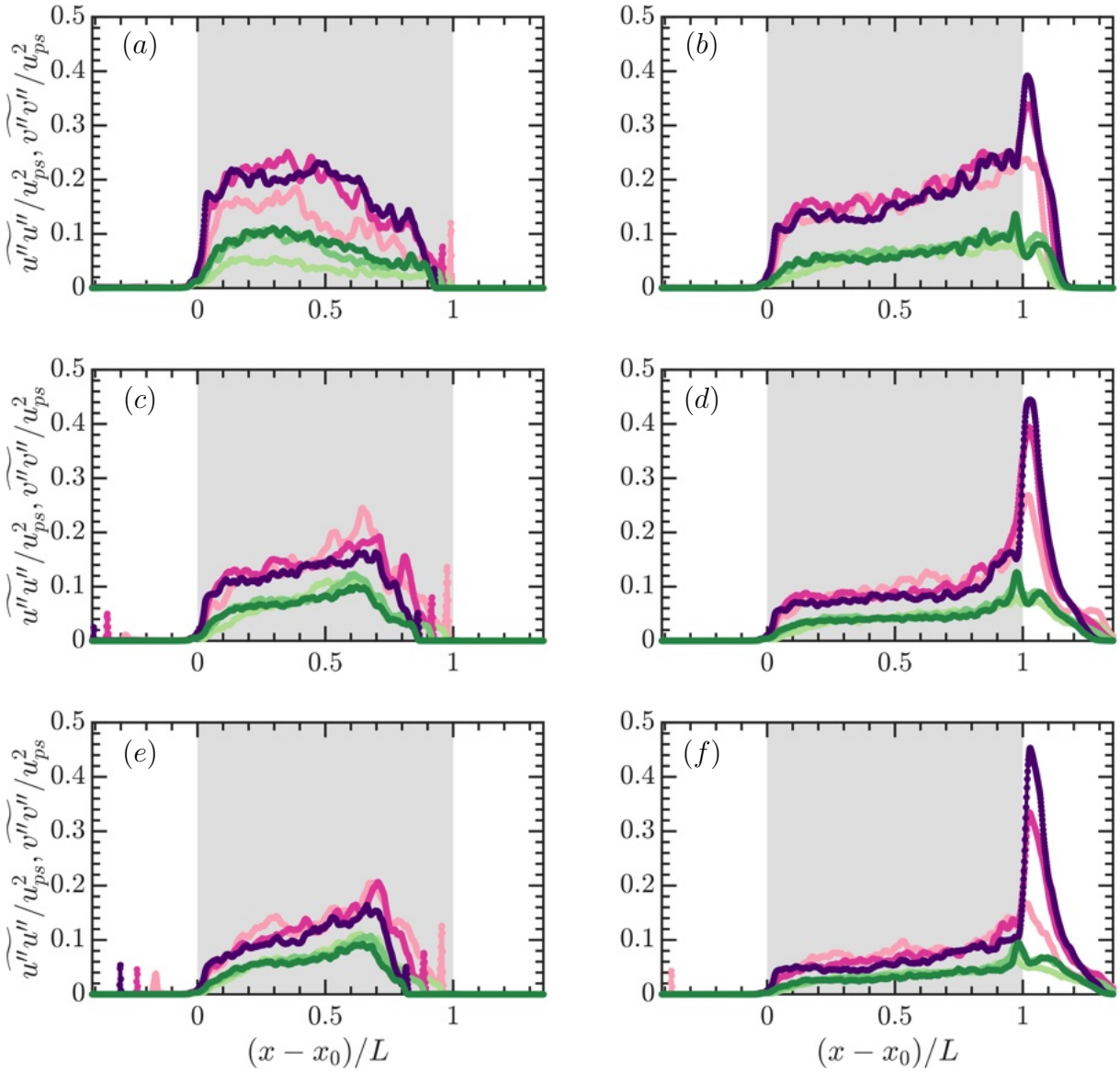

Figure 3.4: Velocity fluctuations at $t/\tau_L = 1$ (left) and $t/\tau_L = 2$ (right). (a, b) $M_s = 1.2$, (c, d) $M_s = 1.66$ and (e, f) $M_s = 2.1$. Streamwise fluctuations u^2_{rms} (pink/purple), spanwise fluctuations v^2_{rms} (shades of green). $\Phi_p = 0.1$ (light shade), $\Phi_p = 0.1$ (intermediate shade), $\Phi_p = 0.3$ (dark shade).

However, we only observe significant variation due to Φ_p at the downstream edge of the curtain. In this region, the streamwise fluctuations increase by approximately a factor of four, yet the spanwise fluctuations remain unaffected.

To better quantify the level of anisotropy, we define the gas-phase anisotropy tensor as

$$b_{ij} = \frac{R_{ij}}{2k_g} - \frac{\delta_{ij}}{3}, \tag{3.4}$$

where $R_{ij} = \widetilde{u_i'' u_j''}$ is the pseudo-turbulent Reynolds stress, $k_g = \widetilde{u_i'' u_i''}/2$ (repeated indices imply summation) is the PTKE and δ_{ij} is the Dirac delta function. The streamwise component b_{11} is dominant compared with the components perpendicular to the flow direction b_{22} and b_{33}. The cross-correlation of velocity fluctuations, b_{12}, is often negligible in gas–solid flows [75]. Due to symmetry in the flow, only b_{11} and b_{22} are reported.

All nine cases are overlaid in Fig. 3.5 at $t/\tau_L = 2$ with each line style representing a distinct volume fraction and each shade of color representing a distinct shock Mach number. A strong degree of anisotropy is observed. Interestingly, the level of anisotropy remains approximately constant across the curtain, with $b_{11} \approx 0.2$ and $b_{22} \approx -0.1$ for all cases, regardless of Φ_p and M_s. Variations are noted only near the curtain edges, where the streamwise component becomes even more dominant. Upstream of the curtain, the anisotropy tensor becomes ill-defined as k_g is zero due to lack of a turbulence production mechanism. The level of anisotropy suggests that approximately 50% of PTKE is partitioned in $\widetilde{u''u''}$ and 25% in $\widetilde{v''v''}$ and $\widetilde{w''w''}$.

PTKE advects and decays downstream of the particle curtain. Case 10 extends $3L$ downstream of the particle curtain to examine this behavior in greater detail. Figure 3.6 shows the rms velocity components at $t/\tau_L = 5$, where the flow reaches a steady state. It can be seen that the flow remains anisotropic beyond the curtain and eventually the fluctuations completely decay. This is analogous to grid-generated turbulence [6, 62, 87]. According to Batchelor [6], the decay of turbulence intensity downstream of a grid (or screen) with mesh

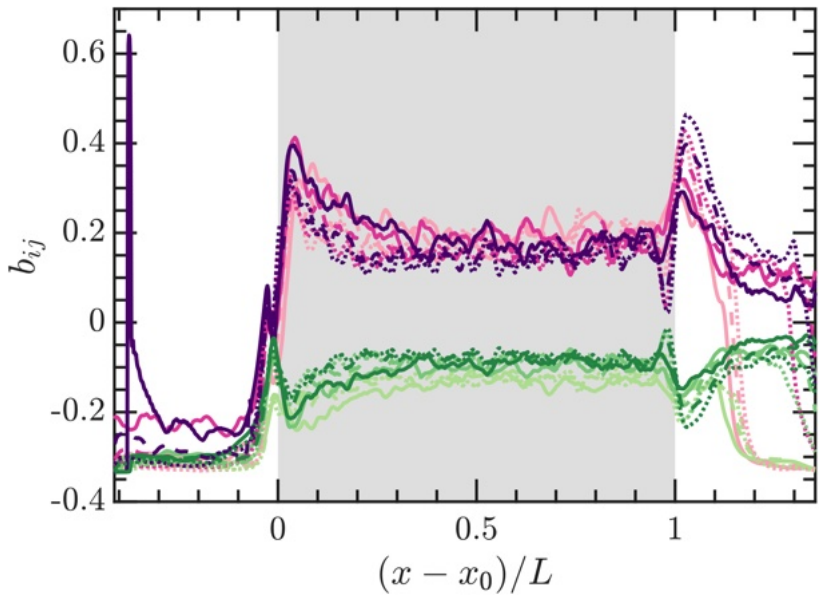

Figure 3.5: Components of the Reynolds stress anisotropy tensor for cases 1–9 at $t/\tau_L = 2$. $\Phi_p = 0.1$ (—), $\Phi_p = 0.2$ (- - -), and $\Phi_p = 0.3$ (·····). Parallel component b_{11} (light pink, pink, purple) and perpendicular component b_{22} (light green, green, dark green) for $M_s = 1.2$, 1.66 and 2.1 (light to dark).

width ΔM follows a power law, given by

$$\left(\frac{u_{\text{rms}}}{u_0}\right)^2 = A\left(\frac{x - x_L}{\Delta M}\right)^n \tag{3.5}$$

where u_0 is the velocity of the gas phase at a point of virtual origin of turbulence x_0 and A is an empirical constant. An analogy can be drawn to our shock-particle configuration by setting the mesh width to the average interparticle spacing, λ, which can be defined as

$$\lambda = D\left(\frac{\pi}{6\Phi_p}\right)^{1/3}. \tag{3.6}$$

Additionally, we set the point of origin of turbulence decay to the location of the downstream curtain edge, $x_L = x_0 + L$, and consider the velocity at this point $u_L = \tilde{u}(x{=}x_L; t{=}5\tau_L)$ when normalizing the turbulence intensity.

Figure 3.6(a) shows the decay of streamwise and spanwise components of rms velocities as a function of the downstream distance normalized by λ. The inset illustrates this decay

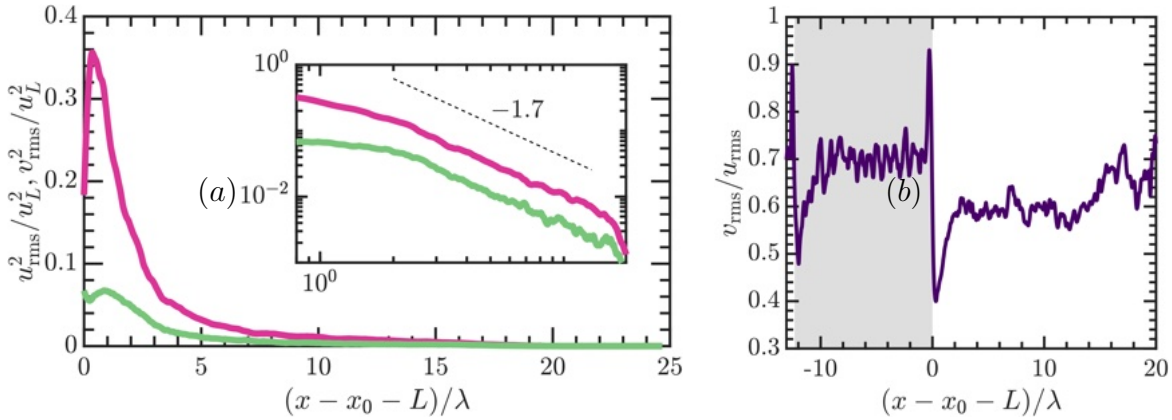

Figure 3.6: (a) Components of rms velocities $u^2_{\rm rms}$ (pink) and $v^2_{\rm rms}$ (green) for Case 10 downstream of the particle curtain at $t/\tau_L = 5$. The inset shows the components in log-scale. (b) Ratio of the spanwise to streamwise rms velocities as a function of streamwise distance normalized by interparticle spacing λ.

in log scale, from which we conclude that the decay does indeed follow a power-law behavior with an exponent $n = -1.7$. This value is slightly higher than the reported values for n in incompressible, single-phase grid-generated turbulence reported in the literature, which range from -1.13 to -1.6 [62, 87]. The ratio $v_{\rm rms}/u_{\rm rms}$ shown in Fig. 3.6(b) highlights significant anisotropy of approximately 0.7, while downstream it reduces to ≈ 0.5 suggesting that the flow remains anisotropic even at later time periods.

The turbulent Mach number, defined as $M_t = \sqrt{2k_g}/\bar{c}$, is shown at $t/\tau_L = 2$ for cases $1 - 9$ in Fig. 3.7. M_t tends to increase rapidly at the upstream edge of the curtain where turbulence is first generated, then gradually increases throughout the curtain and peaks at the downstream edge where the flow chokes. The turbulent Mach number increases monotonically with the incident shock speed. Within the curtain, M_t is relatively independent of Φ_p, but increases with increasing Φ_p at the downstream edge. For the cases with the lowest shock Mach number ($M_s = 1.2$), $M_t \approx 0.2$, which falls in the quasi-isentropic regime, as classified by Sagaut & Cambon [114], where pressure fluctuations are not significant. These cases are distinct from the higher M_s cases in that the velocity does not rapidly increase at the downstream edge of the curtain (see Fig. 3.3(c)) and the mean sound speed remains

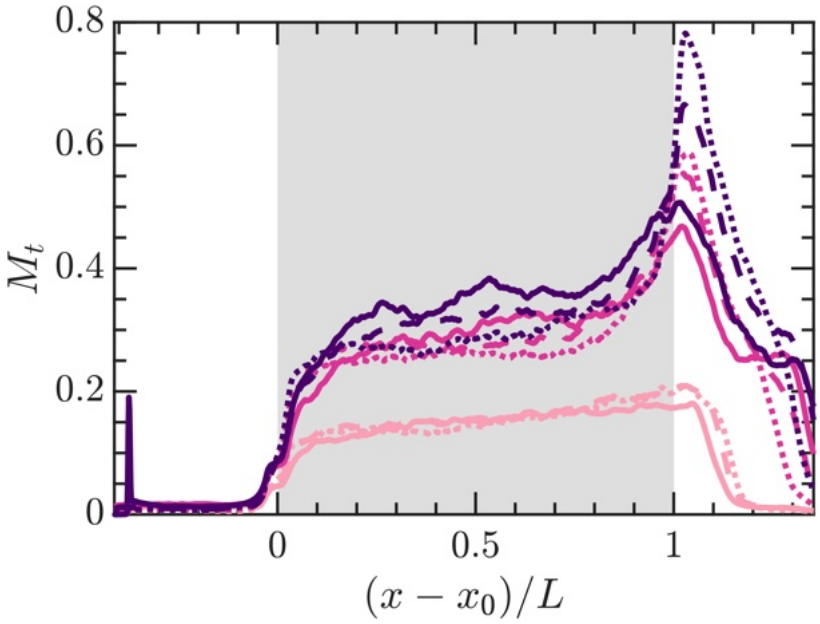

Figure 3.7: Turbulent Mach number for cases $1 - 9$ at $t/\tau_L = 2$. Same legend as b_{11} in figure 3.5.

relatively constant (not shown) and thus the trends in M_t are qualitatively different from the two higher M_s cases. For the two higher shock Mach number cases, M_t varies between 0.3 and 0.8, placing them in the nonlinear subsonic regime where dilatational fluctuations are expected to be important.

3.4.4 Budget of pseudo-turbulent kinetic energy

The presence of particles in the flow generates local gas-phase velocity fluctuations characterized by the pseudo-turbulent kinetic energy (PTKE), defined as $k_g = (\widetilde{u_i'' u_i''})/2$. Reynolds-averaged transport equations for compressible flows have previously been derived by Sarkar et al.[118] (refer Chapter 1), among others. In this study, the transport equation for PTKE is derived in a similar manner, but the presence of particles is accounted for by including the indicator function in the averaging process as defined in § 3.4.2. Multiplying through the viscous compressible Navier–Stokes equations by the indicator function and averaging over the homogeneous y- and z-directions yields a one-dimensional, time-dependent transport

equation for PTKE (a similar derivation is given by Vartdal and Osnes [141]), given by

$$\frac{\partial}{\partial t}(\alpha_g\,\overline{\rho}\,k_g)+\frac{\partial}{\partial x}(\alpha_g\,\overline{\rho}\,\widetilde{u}\,k_g)=\mathcal{P}_S+\mathcal{T}+\Pi+\alpha_g\rho\epsilon+\mathcal{M}+\mathcal{P}_D. \tag{3.7}$$

The terms on the right-hand side represent various mechanisms for producing, dissipating, and transporting PTKE. $\mathcal{P}_s$ is production due to mean shear, $\mathcal{T}$ is a term akin to diffusive transport, Π is the pressure-dilatation correlation term and ϵ is the viscous dissipation tensor. The trailing terms arising from the averaging procedure are lumped into $\mathcal{M}$. $\mathcal{P}_D=\mathcal{P}_D^P+\mathcal{P}_D^V$ is production due to drag that contains contributions from pressure and viscous stresses, respectively. These terms are each defined as

$$\mathcal{P}_S=-\alpha_g\widetilde{\overline{\rho}u''u''}\frac{\partial\widetilde{u}}{\partial x}, \tag{3.8}$$

$$\mathcal{T}=-\frac{1}{2}\frac{\partial}{\partial x}(\alpha_g\overline{\rho u_i''u_i''u''})-\frac{\partial}{\partial x}(\alpha_g\overline{p'u''})+\frac{\partial}{\partial x}(\alpha_g\overline{u_i''\sigma_{i1}'}), \tag{3.9}$$

$$\Pi=\alpha_g\,\overline{p'\frac{\partial u_i''}{\partial x_i}}, \tag{3.10}$$

$$\alpha_g\rho\epsilon=-\alpha_g\,\overline{\sigma_{ik}'\frac{\partial u_i''}{\partial x_k}}, \tag{3.11}$$

$$\mathcal{M}=-\frac{\partial}{\partial x_i}(\alpha_g\overline{p}\,\overline{u_i''})+\alpha_g\overline{p}\frac{\partial\overline{u_i''}}{\partial x_i}+\frac{\partial}{\partial x_i}(\alpha_g\overline{\sigma_{11}}\,\overline{u_i''})-\alpha_g\overline{\sigma_{11}}\frac{\partial\overline{u_i''}}{\partial x_i}, \tag{3.12}$$

$$\mathcal{P}_D=\mathcal{P}_D^P+\mathcal{P}_D^V=\overline{p'u_i''\frac{\partial\mathcal{I}}{\partial x_i}}-\overline{\sigma_{ik}'u_i''\frac{\partial\mathcal{I}}{\partial x_k}}. \tag{3.13}$$

Figure 3.8 shows the budget of PTKE at $t/\tau_L=0.5$ and 2 for different M_s and Φ_p. The terms are normalized by post-shock quantities: $\rho_{ps}u_{ps}^3/D$. The statistics from the particle-resolved simulations are noisy due to the indicator function and to provide reliable data, a low-pass (Gaussian) filter is applied in the streamwise direction with a standard deviation $3D$ after averaging in the periodic directions. It should be noted that most coarse-grain simulations of particle-laden flows use grid spacing larger than D. Also, the resulting profiles were found to be insensitive to a wide range of filter sizes. Note in Fig. 3.8$(c),(e),(h)$, small oscillations upstream of the curtain indicate the location of the reflected shock.

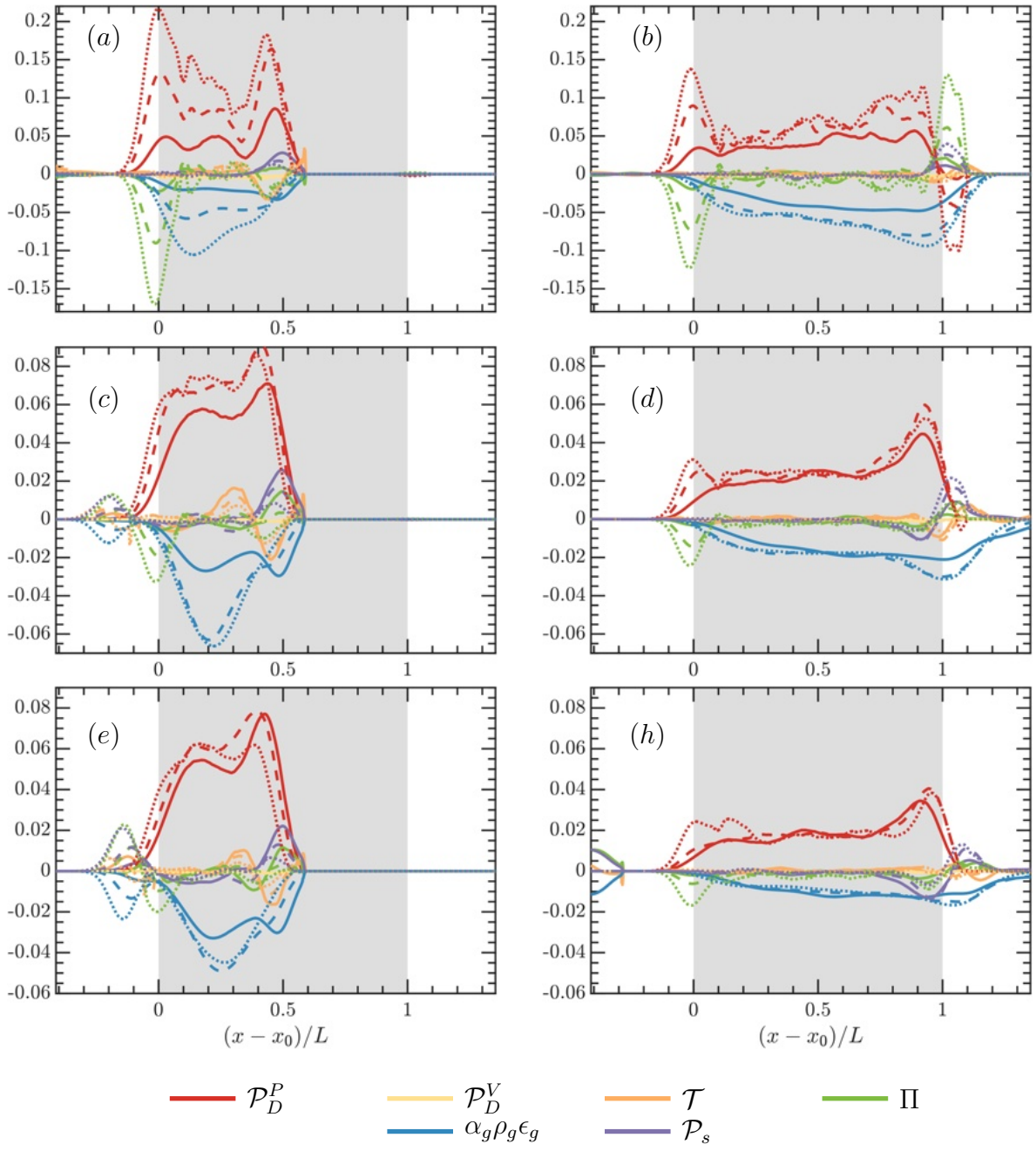

Figure 3.8: Budgets of PTKE at $t/\tau_L = 0.5$ (left) and $t/\tau_L = 2$ (right). (a, b) $M_s = 1.2$, (c, d) $M_s = 1.66$ and (e, f) $M_s = 2.1$. $\Phi_p = 0.1$ (—), $\Phi_p = 0.2$ (- - -) and $\Phi_p = 0.3$ (·····).

.

The majority of PTKE is generated via drag production, which is balanced by viscous dissipation. The remaining terms are negligible except for shear production, $\mathcal{P}_s$, and the pressure-dilatation correlation term Π near the shock and at the edge of the curtain where the volume fraction gradient is large. $\mathcal{M}_s$ is omitted from the plots since it was found to be negligible. At later times after the shock has passed through the curtain, mean-shear production and the pressure-strain correlation act as the dominant production terms at the downstream edge of the curtain. Downstream of the curtain, there are no production mechanisms and viscous dissipation dominates.

The magnitude of the terms in the budget are observed to increase with increasing Φ_p and decrease with increasing shock Mach number. This reduction at higher Mach number is not due to enhanced dilatational dissipation, but rather a reduction of all terms, similar to what has been observed in single-phase compressible shear layers [97, 117].

3.4.5 Energy spectra

Two-dimensional energy spectra of the phase-averaged streamwise velocity fluctuations are computed at different locations along the curtain. Special care is taken to account for the presence of particles. At each location along the x-axis, the instantaneous energy spectrum is defined as

$$E_{uu}(x,t) = \widehat{\sqrt{\mathcal{I}\rho}u''}\,\widehat{\sqrt{\mathcal{I}\rho}u''}^{\,*}, \tag{3.14}$$

where the $\widehat{(\cdot)}$ notation denotes the two-dimensional Fourier transform and * indicates its complex conjugate. The integration of E_{uu} at each streamwise location is taken over a circular shell in the $[\kappa_y \times \kappa_z]$ space, where κ represents the wave number. This definition of the Fourier coefficient is consistent with classic compressible turbulence literature [59, 65], extended to include the indicator function to account for particles.

Figure 3.9 shows the energy spectra for Case 5 ($M_s = 1.66$, $\Phi_p = 0.2$) at various x locations within the particle curtain at $t/\tau_L = 2$. The spectra for the initial 40 grid points

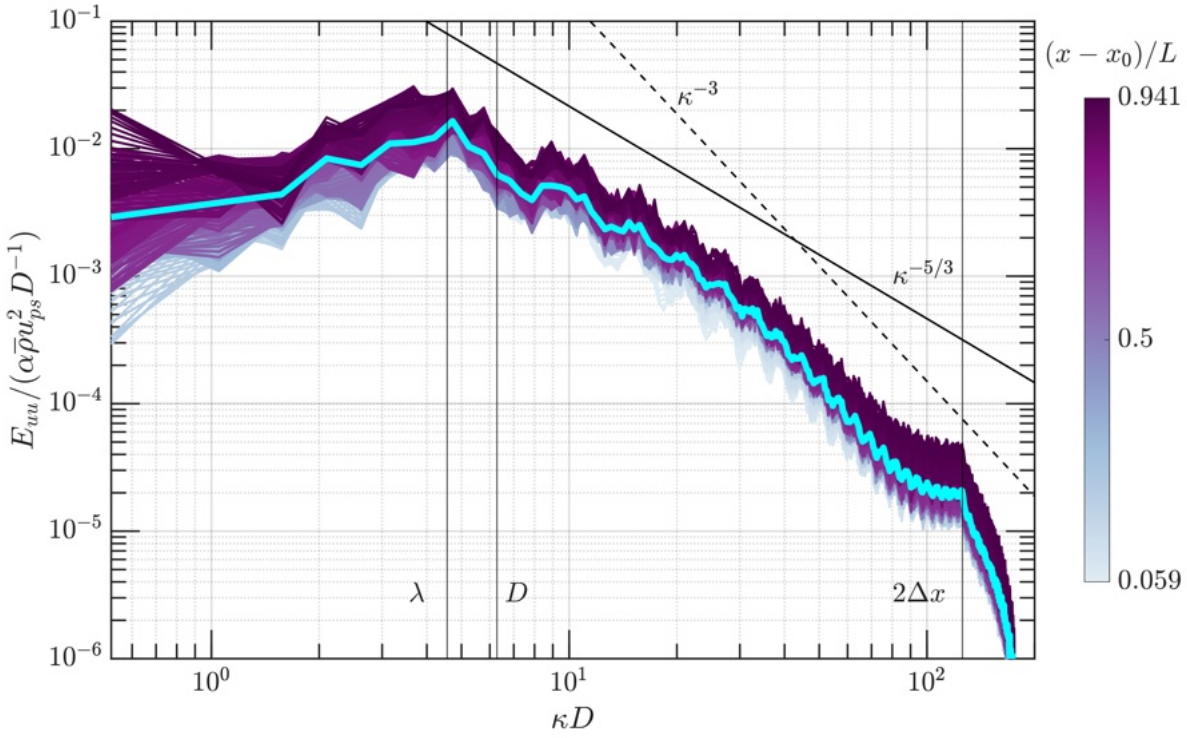

Figure 3.9: One-dimensional spectra of streamwise velocity fluctuations for $M_s = 1.66$ and $\Phi_p = 0.2$ at $t/\tau_L = 2$. The color bar corresponds to different locations in the particle curtain. Ensemble average of all the spectra within the curtain (thick cyan line). Vertical lines indicate relevant length scales in the flow. Solid and dashed lines correspond to slopes of $-5/3$ and -3, respectively.

$(x - x_0 < D)$ are excluded because the turbulence is not fully developed in this region. It is evident that the spectra remain relatively consistent across the streamwise positions, exhibiting minimal variation from the ensemble average of all spectra. Thus, although the flow is inhomogeneous in x, the turbulence is relatively homogeneous in the majority of the curtain. Consequently, subsequent figures will only display the ensemble average.

The inclusion of the discontinuous indicator function in (3.14) introduces oscillations throughout the spectrum, known as a 'ringing' artifact. While the ringing can be mitigated by applying a Butterworth filter or similar methods, such filtering was not employed to avoid the introduction of ad-hoc user-defined parameters.

Most of the energy resides at length scales that coincide with the mean interparticle spacing, λ. The interparticle spacing is found to differentiate the energy-containing range from the inertial subrange, indicating that wakes in the interstitial spaces between particles are responsible for the generation of PTKE. An inertial subrange is evident at scales smaller than λ, characterized by an energy spectrum that follows a $-5/3$ power law before transitioning to a steeper -3 power law at higher wavenumbers. The energy diminishes rapidly at scales below $2\Delta x$, which is attributed to numerical dissipation. Interestingly, part of the inertial subrange aligns with characteristics of homogeneous single-phase turbulence, displaying a $-5/3$ power law, while the smaller scales align with bubble-induced turbulence, evidenced by a -3 power law. However, the presence of noise in the spectra makes it challenging to draw definitive conclusions.

In Fig. 3.10, the ensemble-averaged spectra are compared across different cases at $t/\tau_L = 2$. A broadband reduction in E_{uu} is observed with increasing M_s, which is consistent with the observations made in the PTKE budget. As before, the turbulence levels are largely invariant with Φ_p. For each case, the mean interparticle spacing is found to delineate the inertial subrange. Compensated spectra are also shown to better identify the power-law scaling, which appears consistent in each case. The spectrum decays with a $-5/3$ law at wave numbers $\mathcal{O}(D)$, while at higher wave numbers there is a steeper -3 decay. It remains

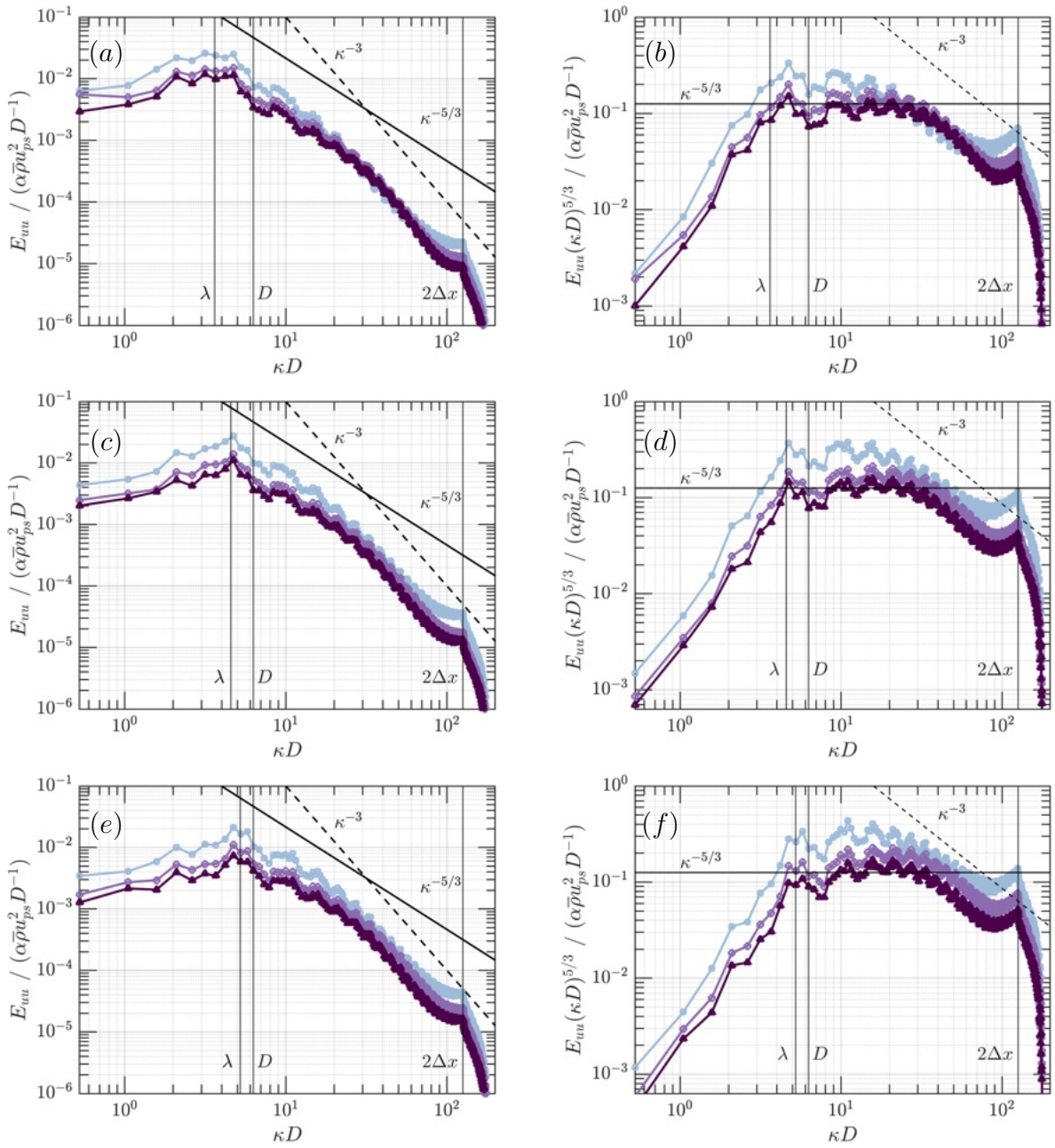

Figure 3.10: Mean (left) and compensated (right) energy spectra of streamwise velocity fluctuations within the particle curtain at $t/\tau_L = 2$ for (a, b) $\Phi_p = 0.1$, (c, d) $\Phi_p = 0.2$ and (e, f) $\Phi_p = 0.3$. $M_s = 1.2$ (light blue, square), $M_s = 1.66$ (lavender, circle), and $M_s = 2.1$ (purple, triangle).

unclear whether this steepening is due to gas-phase compressibility, interphase exchange with particles, or both. The following section decomposes the turbulent velocity field into solenoidal and dilatational components to gain further insight.

3.4.5.1 Helmholtz decomposition

A Helmholtz decomposition of the velocity field is performed to analyze the solenoidal (divergence-free) and dilatational (curl-free) components separately, according to [59, 149]

$$\boldsymbol{u} = \boldsymbol{u}_{sol} + \boldsymbol{u}_{dil}, \tag{3.15}$$

where $\boldsymbol{u}_{sol} = \nabla \times \boldsymbol{A}$ and $\boldsymbol{u}_{dil} = \nabla\varphi$. Here $\boldsymbol{A}$ is the vector potential satisfying $\nabla^2\boldsymbol{A} = -\boldsymbol{\omega}$, where $\boldsymbol{\omega} = \nabla \times \boldsymbol{u}$ is the local vorticity. The velocity potential φ satisfies $\nabla^2\varphi = \nabla \cdot \boldsymbol{u}$.

Figure 3.11 shows two-dimensional slices of the instantaneous streamwise velocity components. The solenoidal component exhibits significant fluctuations throughout the curtain, capturing particle wakes. In contrast, the dilatational velocity field remains relatively small within the curtain and increases sharply at the downstream edge, where the flow chokes. This indicates that the majority of PTKE is concentrated in the solenoidal portion, with compressibility playing a minor role except near large volume fraction gradients.

Figure 3.12 shows energy spectra of the streamwise solenoidal and dilatational velocity components at $t/\tau_L = 2$. The solenoidal energy spectrum is approximately two orders of magnitude larger than the dilatational component across all wavenumbers and tends to decrease with increasing M_s, while the dilatational component increases with increasing Mach number. These findings align with observations from direct numerical simulations of compressible homogeneous isotropic turbulence [30]. Interestingly, only the solenoidal spectrum demonstrates a -3 power law decay, while the dilatational component maintains an approximate $-5/3$ scaling throughout the inertial subrange. Consequently, the -3 power law decay may be attributed to incompressible wakes rather than compressible effects.

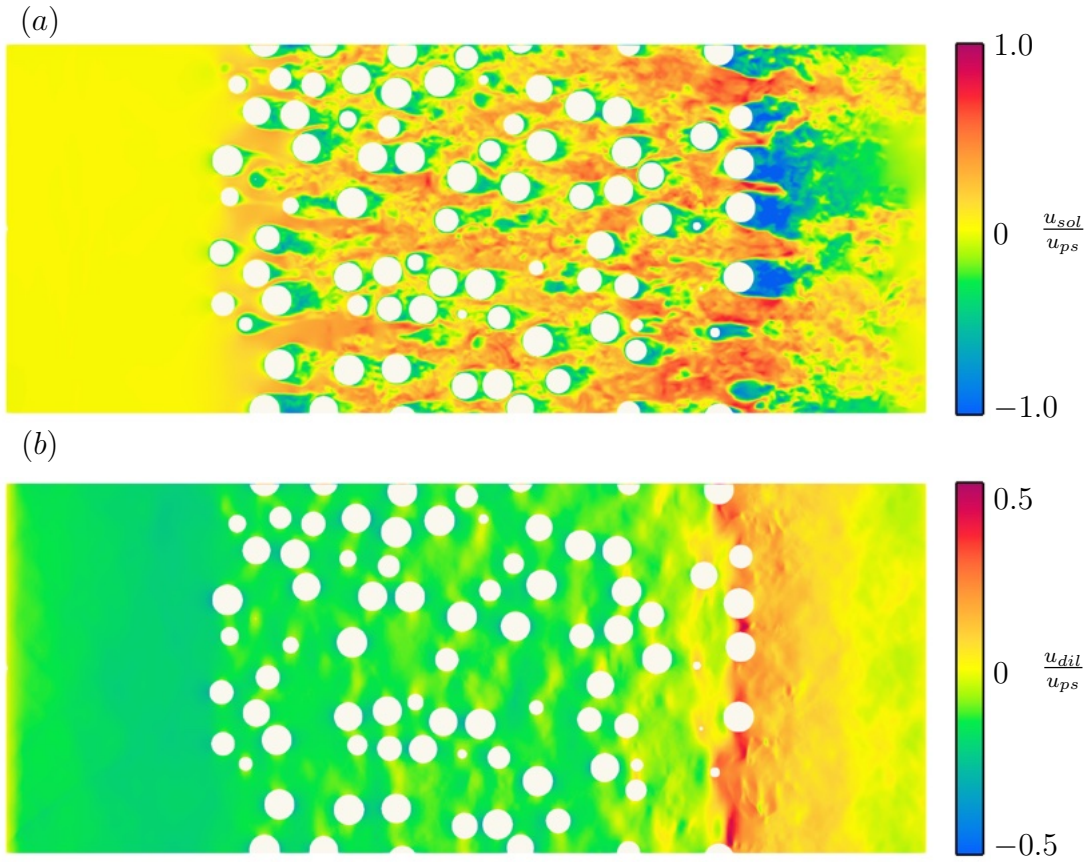

Figure 3.11: A two-dimensional slice of the (a) solenoidal and (b) dilatational streamwise velocity fields at $t/\tau_L = 2$ for Case 5.

A similar decomposition of the dissipation rate was performed following Sarkar et al. [118] and Donzis & John [31], yielding solenoidal ($\bar{\rho}\epsilon_s = \overline{\mu\omega_i''\omega_i''}$; $\boldsymbol{\omega}'' = \nabla \times \boldsymbol{u}''$) and dilatational ($\bar{\rho}\epsilon_d = \overline{4/3\mu(\partial u_i''/\partial x_i)^2}$) components. It was found that ϵ_s dominates the total dissipation of PTKE, exceeding ϵ_d by approximately two orders of magnitude.

3.5 Two-fluid turbulence model

In this section, we propose a two-equation model for PTKE and its dissipation. This turbulence model is integrated into a one-dimensional Eulerian-based two-fluid framework. The hyperbolic equations for particle-laden compressible flows include added mass and internal energy contributions, derived from kinetic theory based on the recent work of Fox [40, 41].

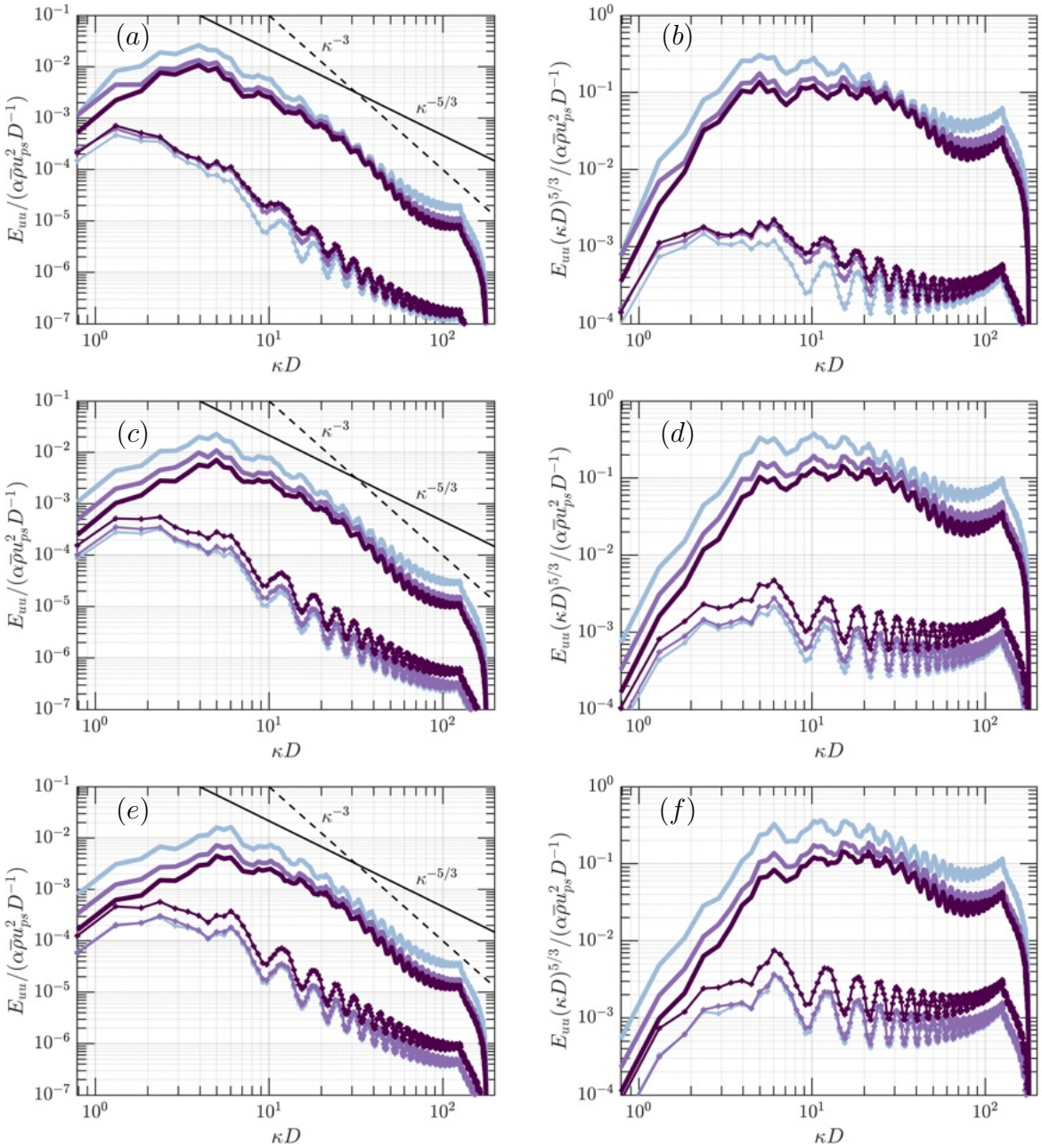

Figure 3.12: Mean (left) and compensated (right) spectra of the streamwise velocity fluctuations computed using solenoidal (—) and dilatational (- -) velocity fields at $t/\tau_L = 2$ for (a, b) $\Phi_p = 0.1$, (c, d) $\Phi_p = 0.2$ and (e, f) $\Phi_p = 0.3$. Color scheme same as figure 3.10.

The section ends with an a-posteriori analysis of the turbulence model and comparisons are made against the particle-resolved simulations.

3.5.1 A kinetic-based hyperbolic two-fluid model

Particle-resolved simulations require grid spacing significantly smaller than the particle diameter to adequately resolve boundary layers and capture relevant aerodynamic interactions. Eulerian-based two-fluid models are a widely used coarse-grained modeling approach that assume the properties of both solid and fluid phases can be expressed as interpenetrating continua interacting through interphase drag terms. Unlike particle-resolved simulations, the computational cost of modeling the particle phase scales with the number of grid cells rather than the number of particles, making it a more efficient option for simulating systems with a large number of particles.

The added mass is included in the mass, momentum, and energy balances, augmented to account for particle wakes. These equations are fully hyperbolic and avoid the ill-posedness common in conventional compressible two-fluid models with two-way coupling [41]. To match the conditions used in the particle-resolved simulations, stationary monodisperse particles are considered (i.e. the particle velocity $\boldsymbol{u}_p = 0$, granular temperature $\Theta_p = 0$ and $\alpha_p \rho_p$ is constant in the curtain, where $\alpha_p = 1 - \alpha_g$ is the particle volume fraction and ρ_p is the particle density). Heat transfer between the phases is neglected. For brevity, brackets and tildes are omitted and it is implied that the equations are written in terms of Favre- and phase-averaged quantities.

The governing equation for mass balance (added mass, gas phase) in one spatial dimension are given by

$$\begin{aligned} \frac{\partial}{\partial t}(\alpha_a \rho_a) &= S_a, \\ \frac{\partial}{\partial t}(\alpha_g^\star \rho) + \frac{\partial}{\partial x}(\alpha_g^\star \rho u) &= -S_a. \end{aligned} \tag{3.16}$$

The gas-phase momentum balance is

$$\frac{\partial}{\partial t}(\alpha_g^\star \rho u) + \frac{\partial}{\partial x}(\alpha_g^\star \rho u^2 + \hat{p} + \alpha_p^\star \alpha_g^\star \rho u^2) = -\frac{\alpha_p^\star \rho}{\tau_p} u + \alpha_p^\star \Big(\frac{\partial}{\partial x} \hat{p} + F_{pg} \Big) - S_{gp}, \tag{3.17}$$

and the gas-phase total energy balance is

$$\frac{\partial}{\partial t}(\alpha_g^\star \rho E) + \frac{\partial}{\partial x}(\alpha_g^\star \rho u E + \alpha_g^\star u \hat{p}) = -S_E. \tag{3.18}$$

The added-mass internal energy balance is

$$\frac{\partial}{\partial t}(\alpha_a \rho_a e_a) = S_E. \tag{3.19}$$

Here, α_a is the volume fraction of the added-mass phase and ρ_a is its density. The gas-phase volume fraction is replaced by $\alpha_g^\star = \alpha_g - \alpha_a$, $\alpha_p^\star = \alpha_p + \alpha_a$, $\alpha_g^\star = 1 - \alpha_p^\star$ and e_a is the specific internal energy of the added mass. The gas- and added-mass phases have the same pressure p, but different temperatures T and T_a, found from e and e_a, respectively. S_a represents mass exchange between the two phases through added mass, leading to momentum S_{gp} and energy S_E exchange. The particle response timescale $\tau_p = 4\rho_p D^2/(3\mu C_D \mathrm{Re}_p)$ depends on the drag coefficient C_D modeled using the drag law from Osnes et al.[94]. This model takes into account the effects of local volume fraction, the particle Reynolds number $\mathrm{Re}_p = \rho|u|D/\mu$ and particle Mach number $M_p = |u|/c$ based on slip velocity $|u|$ ($|u| = |u - u_p|$, $u_p = 0$). The remaining parameters are provided in the Appendix. Note that PTKE contributes to the modified pressure $\hat{p}$.

The equations are solved using a standard finite-volume method implemented in `MATLAB`. A HLLC scheme [137] is employed to solve the hyperbolic part of the system. Further details on the implementation and discretization of the one-dimensional two-fluid model can be found in Boniou & Fox [9].

3.5.2 Two-equation model for PTKE

To capture PTKE in the Eulerian framework, a two-equation k_g–ϵ model is proposed that retains only the significant source terms from the budget:

$$\frac{\partial}{\partial t}(\alpha_g^\star \rho k_g) + \frac{\partial}{\partial x}(\alpha_g^\star \rho k_g u\ ) = \mathcal{P}_s + \mathcal{P}_D - (1+M_t^2)\alpha_g^\star \rho \epsilon, \tag{3.20}$$

$$\frac{\partial}{\partial t}(\alpha_g^\star \rho \epsilon) + \frac{\partial}{\partial x}(\alpha_g^\star \rho \epsilon u\ ) = C_{\epsilon,1}\frac{\epsilon}{k_g}\mathcal{P}_S + \frac{C_{\epsilon,D}}{\tau_D}\mathcal{P}_D - C_{\epsilon,2}\ \alpha_g^\star \rho \frac{\epsilon^2}{k_g} \tag{3.21}$$

where $C_{\epsilon,1} = 1.44$ and $C_{\epsilon,2} = 1.92$ are constants from single-phase turbulence modeling [104]. The mean-shear production term is $\mathcal{P}_s = -\alpha_g^\star \rho \widetilde{u''u''}(\partial u/\partial x)$. Drag production is $\mathcal{P}_D = \alpha_p^\star \rho u^2/\tau_p$. $\tau_D = D/|u|$ is the rate of drag dissipation. ϵ represents the solenoidal component of dissipation, while the dilatational component is captured by the compressibility correction $(1+M_t^2)$ [118].

The mean-shear production term, $\mathcal{P}_s$, includes the streamwise component of the Reynolds stress, $\widetilde{u''u''}$. Based on the findings from § 3.4.3, the anisotropy was found to be relatively constant across the curtain and independent of volume fraction and shock Mach number (see Fig. 3.5). The streamwise component of Reynolds stress is therefore given by

$$\begin{aligned} \widetilde{u''u''} &= 2\left(b_{11} + \frac{1}{3}\right)k_g, \\ \widetilde{v''v''} = \widetilde{w''w''} &= 2\left(b_{22} + \frac{1}{3}\right)k_g, \end{aligned} \tag{3.22}$$

with $b_{11} = 0.2$ and $b_{22} = -0.1$.

In the two-equation model, the only remaining term requiring closure is $C_{\epsilon,D}$, a model coefficient that controls the portion of PTKE produced through drag that ultimately gets dissipated. In the limits of homogeneity and steady state with $M_t = 0$, the unsteady, convective, and mean shear production terms go to zero, thus reducing (3.20) and (3.21) to

$$\mathcal{P}_D = \alpha_g^\star \rho \epsilon \implies \epsilon = \frac{\alpha_p^\star \rho_p}{\alpha_g^\star \rho}\frac{u^2}{\tau_p} \tag{3.23}$$

and

$$\frac{\mathcal{C}_{\epsilon,D}}{\tau_D}\mathcal{P}_D = C_{\epsilon,2}\alpha_g^\star\rho\frac{\epsilon^2}{k_g} \implies C_{\epsilon,D} = C_{\epsilon,2}\tau_D\tau_p\frac{\alpha_g^\star\rho}{\alpha_p^\star\rho_p}\frac{\epsilon^2}{k_g}, \tag{3.24}$$

respectively. Substituting (3.23) into (3.24) yields

$$\frac{k_g}{u^2} = \frac{C_{\epsilon,2}}{C_{\epsilon,D}}\frac{\alpha_p^\star\rho_p}{\alpha_g^\star\rho}\frac{\tau_D}{\tau_p} \implies C_{\epsilon,D} = \frac{3}{4}\frac{\alpha_p^\star}{\alpha_g^\star}\frac{u^2}{k_g}C_{\epsilon,2}C_D. \tag{3.25}$$

We now calibrate the algebraic model for PTKE proposed by Mehrabadi et al.[75] for homogeneous particle suspensions valid for $\alpha_g\mathrm{Re}_p < 300$, $M_p = 0$ and $\alpha_p \geq 0.1$ as

$$\frac{k_g}{u^2} = 2\alpha_p\left(1 + 1.25\alpha_g^3\exp(-\alpha_p\sqrt{\alpha_g\mathrm{Re}_p})\right). \tag{3.26}$$

Plugging (3.26) into (3.25) provides closure for $C_{\epsilon,D}$ and ensures the model returns the correct level of PTKE in the limit of incompressible, homogeneous, steady flow. Because $\alpha_p^\star \to \alpha_p$ when $\alpha_p \to 0$, $C_{\epsilon,D}$ remains finite outside the particle curtain. With the expression for $C_{\epsilon,D}$, the two-equation transport model for PTKE and dissipation is now fully closed and is implemented in the two-fluid model from § 3.5.1.

3.5.3 A-posteriori analysis

One-dimensional shock–particle interactions are simulated using the two-fluid model detailed above with the parameters used in the particle-resolved simulations. It should be noted that the results will depend significantly on the volume fraction profile. To ensure a fair comparison, one-dimensional volume fraction profiles are extracted from the particle-resolved simulations and used in the model (see Fig. 4.4).

Figure 3.14 shows comparisons of the mean streamwise velocity between the two-equation model and particle-resolved simulations. Overall excellent agreement is observed. The location of the transmitted and reflected shocks are predicted correctly. The model can be seen to predict choked flow at the downstream edge resulting in supersonic expansion, closely

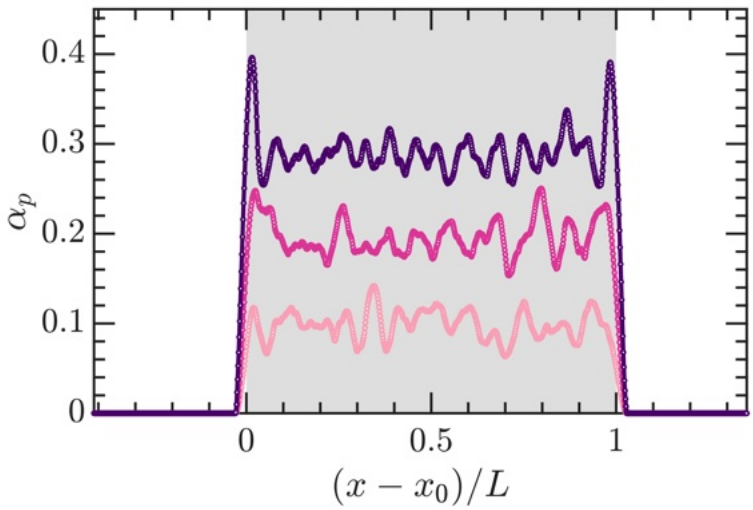

Figure 3.13: One-dimensional particle volume fraction profiles obtained from the particle-resolved simulations for $\Phi_p = 0.1$ (light pink), $\Phi_p = 0.2$ (pink) and $\Phi_p = 0.3$ (purple).

matching the particle-resolved simulations.

Figure 3.15 shows comparisons of PTKE between the two-equation model and particle-resolved simulations at two time instances. Results show good agreement for all cases considered except for the cases with $M_s = 1.2$ at higher volume fractions. The model predicts an increase in PTKE with Φ_p, which is not observed in the particle-resolved simulations. Despite this, the model results show overall good agreement both within the curtain and downstream.

The terms in the PTKE budget computed from the two-equation model are compared with particle-resolved simulation data to identify and explain the observed discrepancies in PTKE. Specifically, the dominant terms–drag production $\mathcal{P}_D$, viscous dissipation $\alpha_g \rho \epsilon$, and mean-shear production $\mathcal{P}_s$–are examined. Figure 3.16 presents the comparison for one case, with similar results observed across all cases. Overall, excellent agreement is found over the three time instances shown. The largest discrepancies occur at the upstream and downstream edges of the curtain, where the particle-resolved simulations predict a sharper increase in drag production at the upstream edge and greater dissipation at the downstream edge. These differences may be attributed to numerical diffusion in the coarse-grained model.

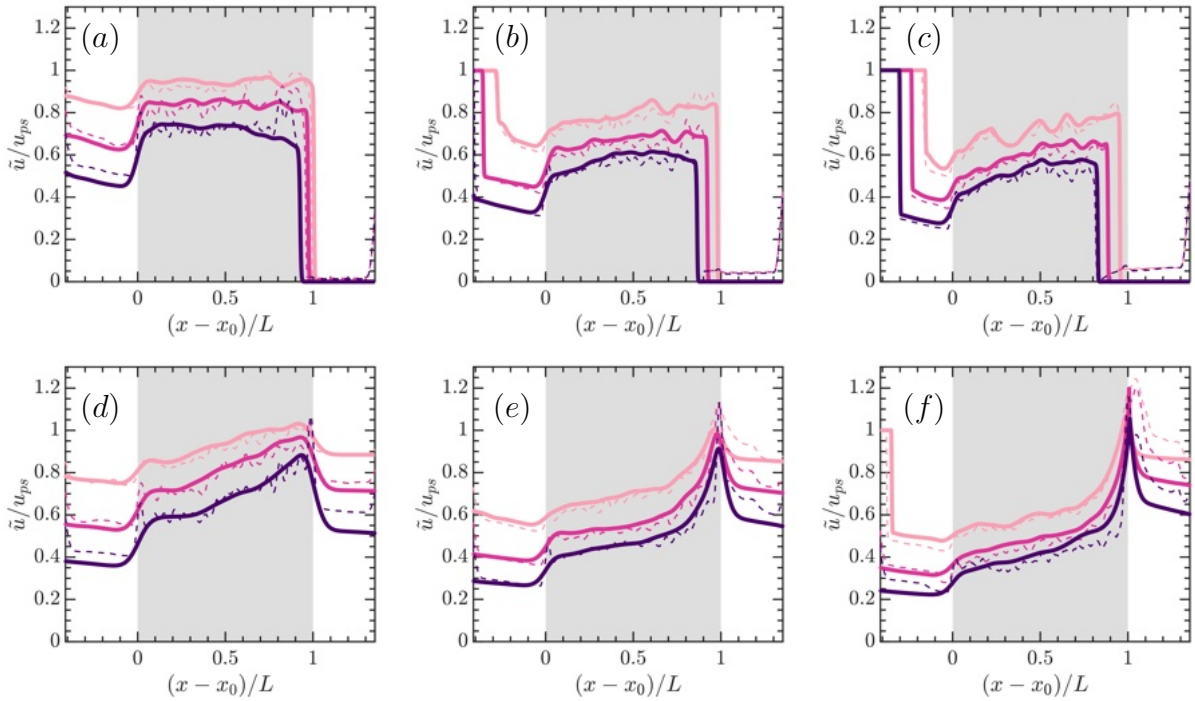

Figure 3.14: Comparison of mean streamwise velocity from particle-resolved simulations (- - -) with results from the two-equation model (—). (a, d) $M_s = 1.2$, (b, e) $M_s = 1.66$, (c, f) $M_s = 2.1$. $t/\tau_L = 1$ (top) and $t/\tau_L = 2$ (bottom). The color scheme for different volume fraction cases is the same as in figure 4.4.

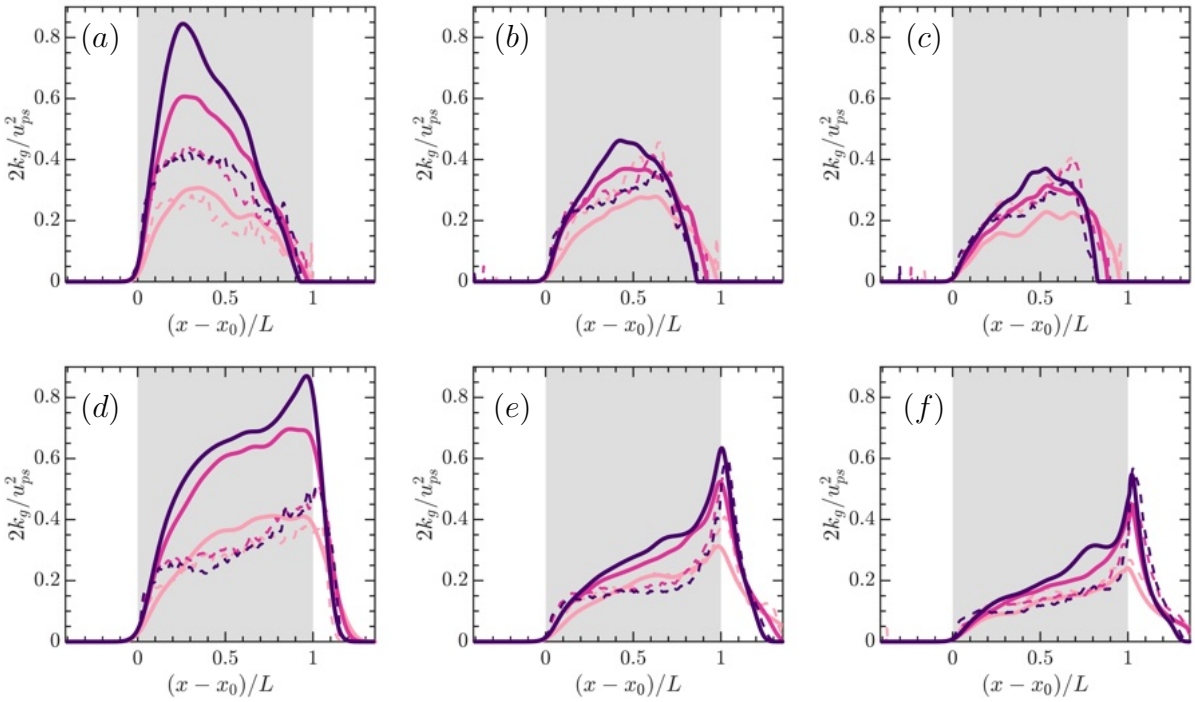

Figure 3.15: Comparison of pseudo-turbulent kinetic energy between particle-resolved simulations (- - -) with the two-equation model (—). (a, d) $M_s = 1.2$, (b, e) $M_s = 1.66$, (c, f) $M_s = 2.1$. $t/\tau_L = 1$ (top) and $t/\tau_L = 2$ (bottom). The color scheme for different volume fraction cases is the same as in figure 4.4.

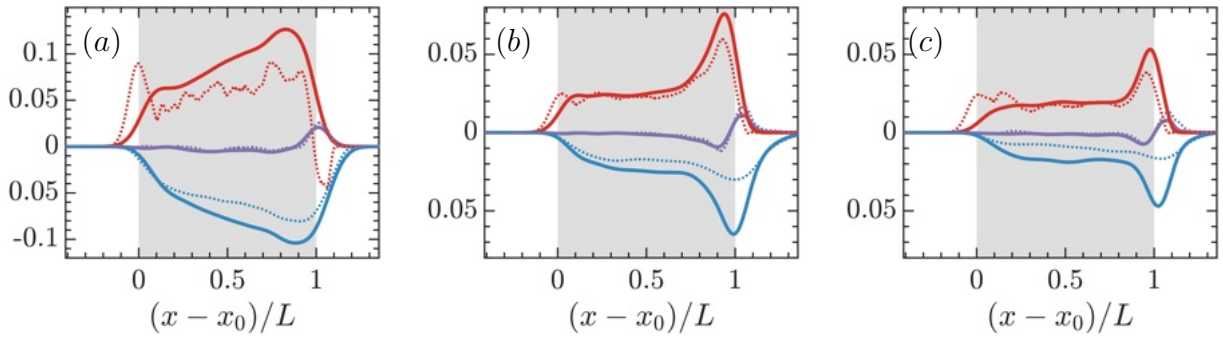

Figure 3.16: Comparison of terms in the PTKE budget between the two-equation model (—) and particle-resolved simulations (·····) for (a) $M_s = 1.2$ and $\Phi_p = 0.2$, (b) $M_s = 1.66$ and $\Phi_p = 0.2$ and (c) $M_s = 2.1$ and $\Phi_p = 0.3$ at $t/\tau_L = 2$. $\mathcal{P}_D^P$ (red), $\mathcal{P}_s$ (purple) and $\alpha_g \rho_g \epsilon_g$ (blue).

The streamwise and spanwise fluctuations are reconstructed using (3.22) and compared with particle-resolved simulations in Fig. 3.17. Overall, the results show good agreement, with cases 2 and 3 exhibiting the most discrepancies. These discrepancies may arise from the drag model, the choice of $C_{\epsilon,D}$, or the omission of the viscous term in the two-fluid model. At the downstream edge, streamwise fluctuations are slightly underpredicted, likely due to an overprediction of viscous dissipation, as observed in the previous figure. This overprediction is ultimately linked to the choice of $C_{\epsilon,D}$ or the drag model. Despite these issues, the two-equation model predicts the overall behaviour well, including the PTKE downstream of the curtain, in the pure gas.

The gas-phase turbulence downstream of the curtain lacks any production terms and, according to the budget, should only advect and diffuse. The cases considered so far extend only $6D$ from the downstream curtain edge to the right domain boundary. Here, we examine Case 10 from table 3.1, with $M_s = 1.66$, $\Phi_p = 0.3$, and a domain extending $34D$ ($2L$) downstream. Figure 3.18 shows PTKE comparisons after the flow reaches a statistically stationary state. The PTKE decay resembles grid-generated turbulence, and the model captures the turbulence transport and decay well.

3.6 Conclusion

When a shock wave interacts with a suspension of solid particles, momentum and energy exchanges between the phases give rise to complex flow. Particle wakes induced by the transmitted shock generate velocity fluctuations referred to as 'pseudo-turbulence.' Phase-averaging the viscous compressible Navier–Stokes equations reveals a route for turbulence generation through drag production within the particle curtain and localized mean-shear production at the edge of the curtain. This turbulence generation is balanced by viscous and dilatational dissipation.

Three-dimensional particle-resolved simulations of planar shocks interacting with sta-

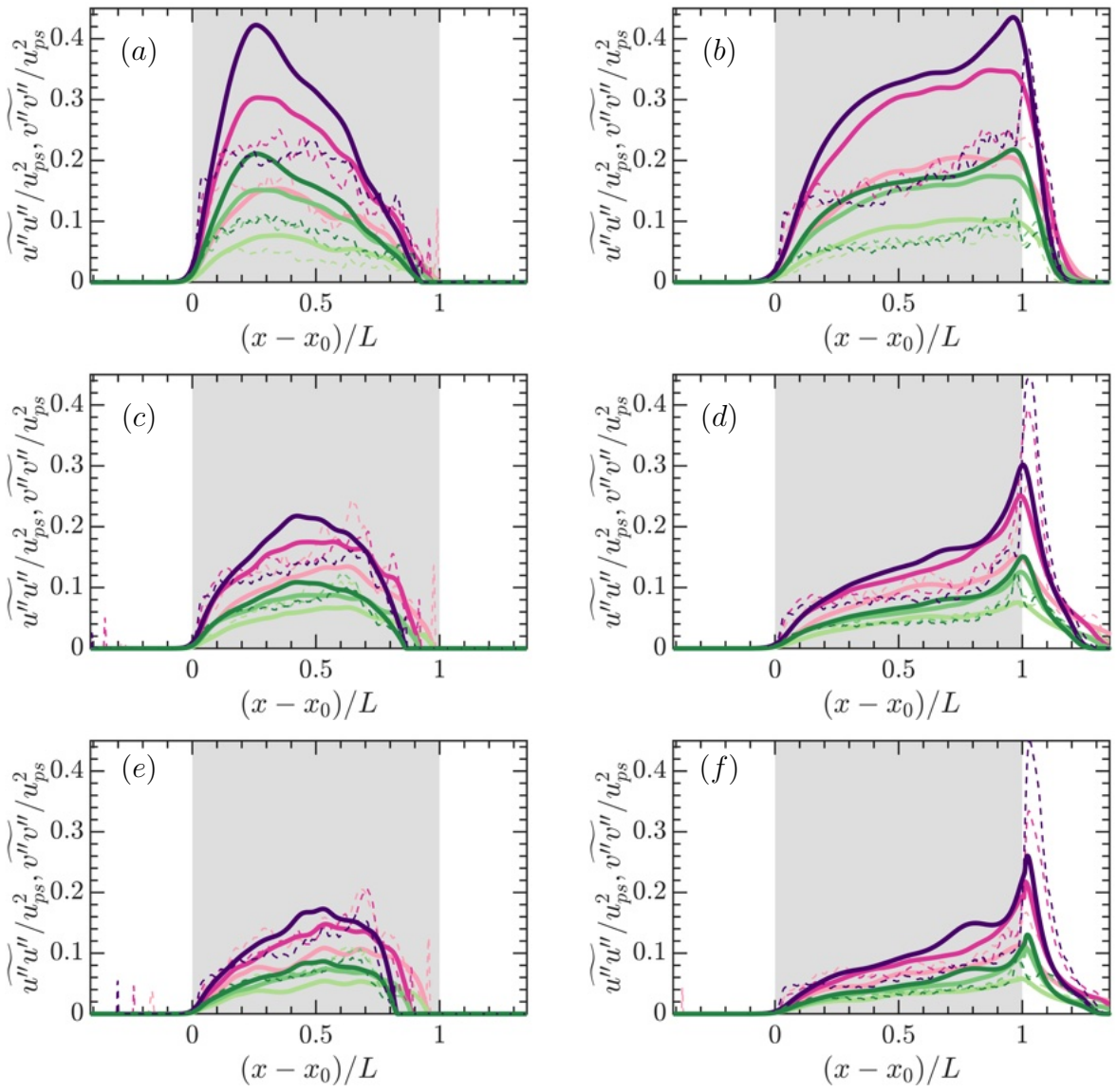

Figure 3.17: Comparison of pseudo-turbulent Reynolds stresses between the particle-resolved simulations (- - -) and the model (——). (a, d) $M_s = 1.2$, (b, e) $M_s = 1.66$, (c, f) $M_s = 2.1$. Color scheme defined in Fig. 3.4.

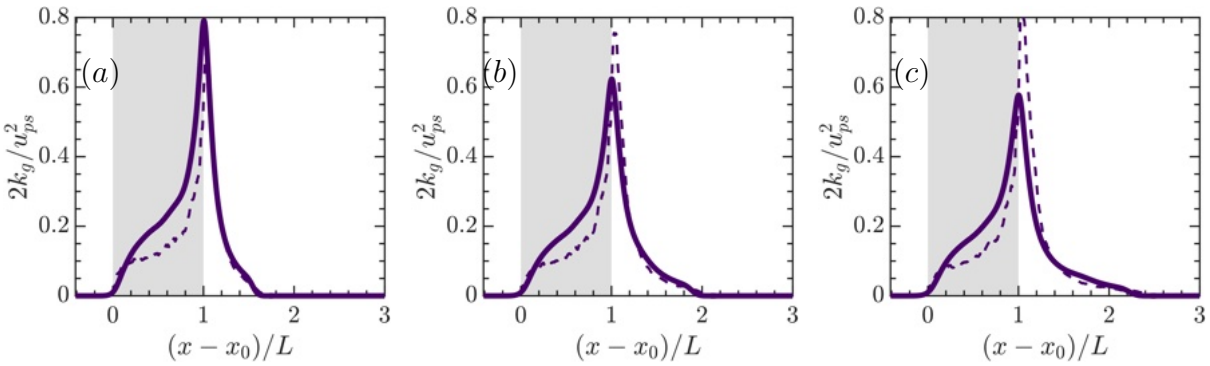

Figure 3.18: Comparison of pseudo-turbulent kinetic energy of the longer domain (case 10) between particle-resolved simulations (- - -) and the two-equation model (—) at (*a*) $t/\tau_L = 3$, (*b*) $t/\tau_L = 4$ and (*c*) $t/\tau_L = 5$.

tionary spherical particles were used to analyze the characteristics of pseudo-turbulence for a range of shock Mach numbers and particle volume fractions. In each case, pseudo-turbulent kinetic energy (PTKE) is generated through interphase drag coupling, contributing to $20 - 50\%$ of the post-shock kinetic energy. The abrupt change in volume fraction at the downstream edge of the curtain chokes the flow, resulting in supersonic expansion where PTKE is maximum. The pseudo-turbulent Reynolds stress is highly anisotropic but approximately constant throughout for the range of volume fractions and Mach numbers considered. The energy spectra of the streamwise gas-phase velocity fluctuations reveal an inertial subrange that begins at the mean interparticle spacing and decays with a $-5/3$ power law then steepens to -3 at smaller scales. This -3 scaling only exists in the solenoidal component of the velocity field and is attributed to particle wakes.

A one-dimensional two-equation turbulence model was formulated for PTKE and its dissipation and implemented within a hyperbolic two-fluid framework. Drag production is closed using a drag coefficient that takes into account local volume fraction, Reynolds number and Mach number. A new closure is proposed for drag dissipation that ensures the proper amount of PTKE is obtained in the limit of statistically stationary and homogeneous flow. An a-posteriori analysis demonstrated the ability of the model to predict PTKE accurately during shock-particle interactions and capture flow-choking behavior. Such a turbulence model can

be adopted into Eulerian two-fluid models or Eulerian–Lagrangian frameworks.

3.7 Acknowledgments

The authors would like to acknowledge the computing resources and assistance provided by Advanced Research Computing at the University of Michigan, Ann Arbor. The authors would also like to thank the resources provided by the NASA High-End Computing (HEC) Program through the NASA Advanced Supercomputing (NAS) Division at Ames Research Center. A portion of this work was supported by the National Aeronautics and Space Administration (NASA) SBIR contract no. 80NSSC20C0243 and SBIR contract no. HDTRA125P0006.

3.8 Appendix

3.8.1 Convergence studies

This section quantifies the effects of varying domain size and particle configurations within the curtain in particle-resolved simulations. A grid refinement study of the numerical solver for periodic compressible flow over a homogeneous suspension is detailed in our previous work [58].

3.8.1.1 Effect of domain size

In this section, we examine the effects of varying the domain size in the periodic spanwise (y and z) directions. A series of three-dimensional simulations were performed with $M_s = 1.66$ and $\Phi_p = 0.2$ to evaluate the impact of domain size on the individual terms in the PTKE budget. Table 3.2 summarizes the cases considered. The streamwise domain length L_x is kept constant, while the spanwise dimensions L_y and L_z are varied. Uniform grid spacing is maintained at $\Delta = D/40$.

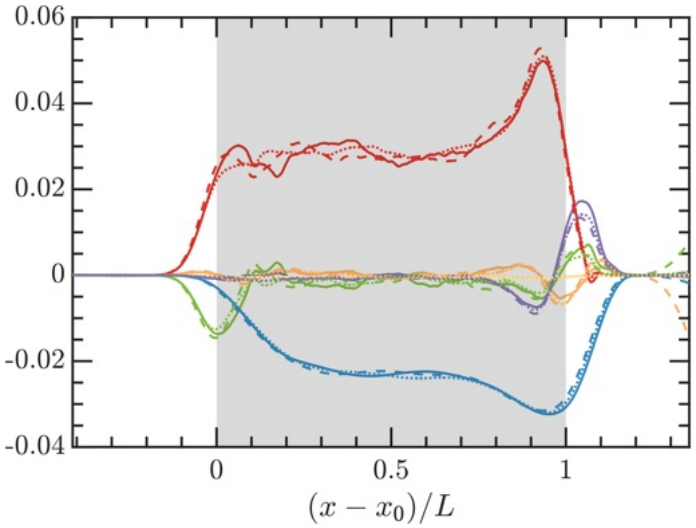

Figure 3.19: Effect of domain size on the PTKE budget for $M_s = 1.66$ and $\Phi_p = 0.2$ at $t/\tau_L = 1.5$. Case A (—), Case B (- - -), Case C (·····). Colours correspond to figure 3.8.

Fig. 3.19 presents comparisons of the individual PTKE budget terms. The results indicate that variations in the periodic domain lengths have minimal influence on the budget terms, suggesting that volume-averaging over two-dimensional $y - z$ slices can be performed without significantly affecting the one-dimensional statistics. Consequently, for the case studies presented in the main paper, we adopt $L_y = L_z = 12D$.

Case	L_x/D	L_y/D	L_z/D	$N_x \times N_y \times N_z$	N_p
A	30	8.5	8.5	$1200 \times 340 \times 340$	470
B	30	12	12	$1200 \times 480 \times 480$	936
C	30	24	24	$1200 \times 960 \times 960$	3740

Table 3.2: Parameters used for the domain size study. For each case, $M_s = 1.66$ and $\Phi_p = 0.2$.

3.8.1.2 Effect of varying random particle distributions

Particles are randomly distributed within the curtain while avoiding overlap. The drag force on individual particles is known to depend on the arrangement of their neighbours [1, 64, 94]. This section investigates the impact of different random particle configurations within the curtain on PTKE for $M_s = 1.2$ and $\Phi_p = 0.3$. Three distinct realizations are considered, keeping all parameters constant except for the random arrangement of particles.

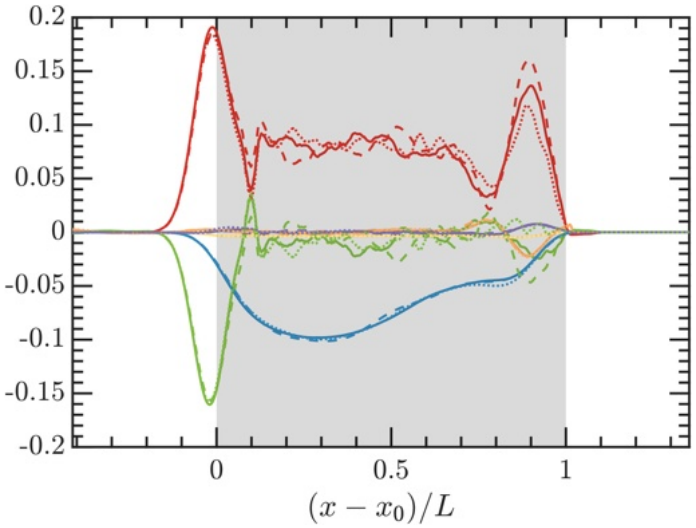

Figure 3.20: Effect of random particle placement on the PTKE budget for $M_s = 1.2$ and $\Phi_p = 0.3$ at $t/\tau_L = 1$. Realization 1 (—), realization 2 (- - -), realization 3 (·····). Colours correspond to figure 3.8.

Figure 3.20 shows the PTKE budget terms for each realization at $t/\tau_L = 1$, when the shock has just passed the downstream edge of the curtain. All realizations exhibit similar trends with negligible discrepancies. Therefore, we conclude that the random distribution of particles does not significantly affect the statistics.

3.8.2 One-dimensional two-fluid model parameters

Starting from the conserved variables $X_1 = \alpha_a \rho_a$ and $X_2 = \alpha_g^\star \rho$ with known α_p, the primitive variables are found using the following formulae:

$$\hat{\kappa} = \frac{X_1}{X_2};\ \kappa = \frac{T}{T_a};\ T = \frac{\gamma e}{C_p};\ T_a = \frac{\gamma e_a}{C_p};\ e = E - \frac{1}{2}u^2 - k_g; \tag{3.27}$$

$$\alpha_g = 1 - \alpha_p;\ \alpha_a = \frac{\hat{\kappa}}{\hat{\kappa} + \kappa}\alpha_g;\ \alpha_p^\star = \alpha_p + \alpha_a;\ \alpha_g^\star = \alpha_g - \alpha_a;\ \rho = \frac{X_2}{\alpha_g^\star}; \tag{3.28}$$

$$p = (\gamma - 1)\rho e;\ \hat{p} = p + 2/3\rho k_g. \tag{3.29}$$

The remaining model parameters are defined as follows:

$$P_{pfp} = \rho(\alpha_p^\star u)^2;\ F_{pg} = u^2\partial_x\rho + 2/3\rho(\partial\alpha_g^\star u/\partial x)u \tag{3.30}$$

$$S_a = \frac{\rho}{\tau_a}(c_m^\star\alpha_p\alpha_g - \alpha_a);\ S_{gp} = \max(S_a, 0)u;\ S_E = \max(S_a, 0)E + \min(S_a, 0)e_a \tag{3.31}$$

$$\mathrm{Re_p} = \frac{\rho \mathrm{Du}}{\mu};\ \mathrm{Pr} = \frac{\mathrm{C_p}\mu}{\mathrm{k}}; \tag{3.32}$$

$$c_m^\star = \frac{1}{2}\min(1 + 2\alpha_p, 2);\ \tau_a = 0.001\tau_p;\ \tau_p = \frac{4\rho_p D^2}{3\mu C_D Re_p}. \tag{3.33}$$

The drag coefficient C_D is given by Osnes et al. [94].

CHAPTER 4

An Analysis of Shock-Induced Size Segregation

Note: A version of this chapter is published in *Acta Mechanica Sinica* [127]. Data and figures have been used with all co-authors' consent.

4.1 Abstract

The framework developed in Chapter 2 is applied to a high-fidelity simulation of a planar shock interacting with bidisperse distributions of particles with size ratios of approximately thirty. Particle dispersion and size segregation are reported. A simple model is proposed for size segregation as a function of the particle diameter size ratio.

4.2 Simulation setup

To investigate particle size segregation and curtain displacement, we consider a three-dimensional domain with a planar shock interacting with a curtain of bidisperse particles (see Fig. 4.1). The particle curtain has a length of $L_c = 2.5$ mm and contains a mixture of large and small particles with diameters $D = 300$ μm and $d = 10$ μm, respectively. The total volume fraction within the curtain is $\Phi_p = 9.5\%$, with a 75% make-up of large particles and 25% of small particles by volume. The particle density is $\rho_p = 2520$ kg/m^3, corresponding

to soda lime. A summary of particle parameters is given in Table 5.1.

Table 4.1: Particle parameters used in the simulations.

Particle class	**Diameter** (μm)	**Volume fraction** %	**No. of particles** –	**Resolution** –	Re_s –
Large	$D = 300$	7.125	$N = 162$	$D/\Delta x = 33$	12624
Small	$d = 10$	2.375	$n = 2007898$	$d/\Delta x = 1$	420.8

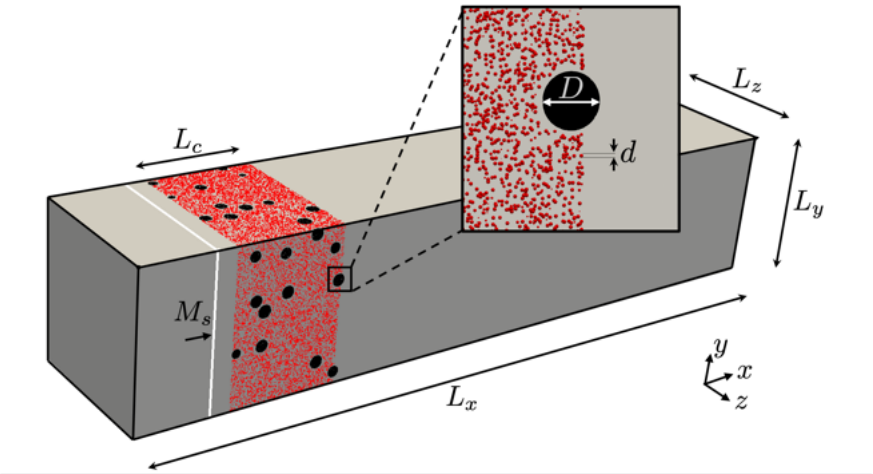

Figure 4.1: Schematic of the simulation setup with the inset showing the particle size difference (not to scale). The white line indicates the initial position of the shock. The black circles represent large particles and red circles represent small particles.

A shock Mach number of $M_s = 1.7$ is considered, defined as $M_s = u_s/c$, where u_s is the shock speed and c is the local speed of sound. The pre-shock conditions are taken to be air at standard temperature and pressure with $[P_\infty, \rho_\infty, u_\infty]$ = [82.7 kPa, 1.2 kg/m^3, 0 m/s]. The reference viscosity and heat capacity at constant pressure for air are $\mu_\infty = 1.8 \times 10^{-5}$ Pa·s and $C_{p,\infty} = 1005$ m^2/s^2/K, respectively. The reference sound speed is $c_\infty = 310$ m/s. The post-shock conditions are computed via the Rankine–Hugoniot jump conditions. A Reynolds number based on post-shock conditions is $Re_s = \rho_{ps} u_{ps} L/\mu_{ps}$, where $[\rho_{ps}, u_{ps}, \mu_{ps}]$ corresponding to [2.64 kg/m^3, 287.215 m/s, 2.31×10^{-5} Pa·s] are the post-shock density, velocity and viscosity, respectively. L is a characteristic length scale taken to be D for large particles and d for small particles (see Table 5.1).

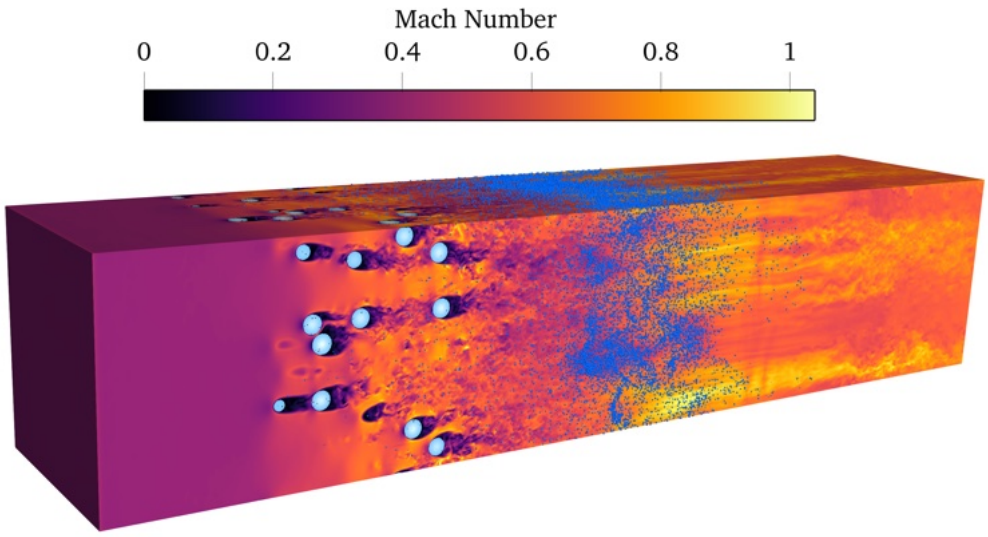

Figure 4.2: Contour of local gas-phase Mach number at $t/\tau_L = 10.13$ showing large (cyan circles) and small particles (dark blue).

The computational domain spans $[L_x \times L_y \times L_z] = [57 \times 12 \times 12]D$ with grid resolution of $D/\Delta x = 33$. This corresponds to grid spacing of $\Delta x = d$. This grid spacing is chosen based on the grid resolution study [125] and a validation study for the IBM method [58] in our previous work. The number of grid points in each direction is $[N_x \times N_y \times N_z] = [1881 \times 366 \times 366]$. The curtain length is set to $L_c = 8.3D$, with a downstream length extending to $5L_c$. Periodic boundary conditions are enforced in y and z. Since the grid resolution is sufficiently high, this high-fidelity simulation was run on UCSD's Expanse clusters through an `ACCESS` allocation using 1920 cores requiring roughly 100k CPU-h.

4.3 Results

4.3.1 Flow visualization

A three-dimensional visualization of the local gas-phase Mach number (Ma) and particle position at $(t-t_0)/\tau_L = 10.13$ is shown in Fig. 4.2. Here, time is normalized by $\tau_L = L_c/u_{ps}$, based on the curtain length and post-shock velocity, where t_0 is the instant the shock impinges

the upstream edge of the curtain. For a shock Mach number $M_s = 1.7$ and a curtain length of $L_c = 2.5$ mm, $\tau_L = 8.7$ μs. At the instant shown, the shock has reached the downstream boundary and particles have segregated significantly. The small particles are scaled up for better visibility. Wakes can be seen downstream of large particles, inducing gas-phase velocity fluctuations that travel downstream. Most of the small particles have traveled downstream of the curtain, forming local high-concentration clusters, while a dilute suspension of small particles remain in the wakes of larger particles.

Figure 4.3 shows a time series of two-dimensional slices of the two-phase flow. Upon impingement of the particle curtain, the incident shock splits into a transmitted shock traveling downstream and multiple shocklets upstream that coalesce into a reflected shock wave traveling upstream as seen in Fig. 4.3(a). Small particles are seen to accelerate rapidly in comparison with the highly inertial large particles. This can be observed in Fig. 4.3(b) where small particles have accumulated towards the downstream curtain edge leading to a concentrated region. Interactions between the small and large particles can be observed more distinctly in the inset provided. The majority of particle collisions are between small particles and the upstream side of large particles. Moreover, some small particles become trapped in the wake of large particles. Both of these effects hinder the segregation rate.

Small particles moving through interstitial spaces between large particles follow the wake and eventually coalesce several large particle lengths downstream. Because the particle response time (and thus the Stokes number) scales with the square of the diameter, the larger particles are far more inertial and respond much slower to the impinging shock. Small particles move through the interstitial spaces in the curtain, and eventually exit the curtain and spread out over much larger lengths as can be seen in Fig. 4.3(e). In contrast, the large particles have not yet moved one curtain length in distance downstream of their initial position over the simulated time.

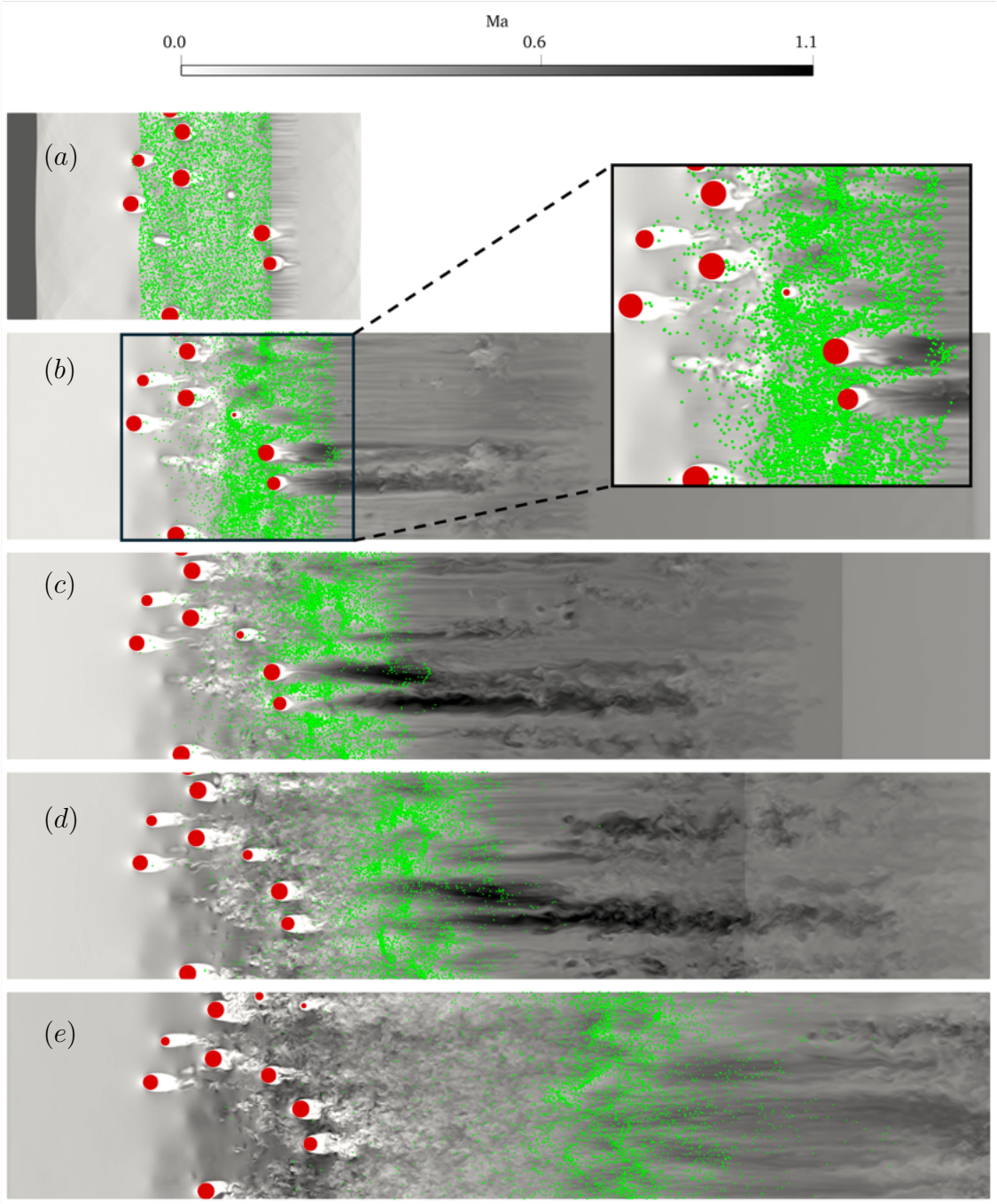

Figure 4.3: Local gas-phase Mach number and particle position in the $x-y$ plane at $z = 6D$ when (a) $(t - t_0)/\tau_L = 1.16$, (b) 4.43, (c) 6.32, (d) 8.1, and (e) 11.89. Red and green circles depict large and small particles, respectively.

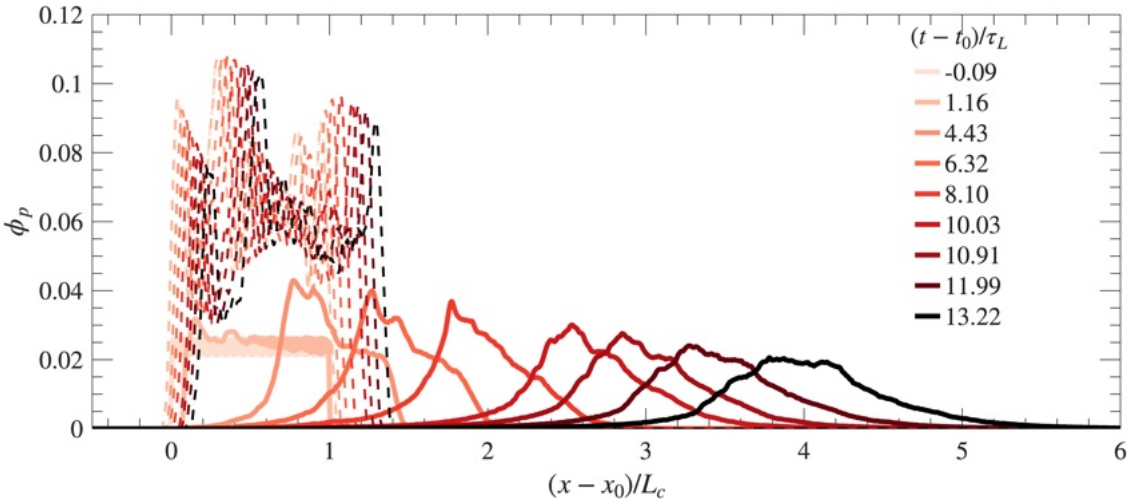

Figure 4.4: Profiles of particle volume fraction associated with large particles (dashed lines) and small particles (solid lines) at different time instances.

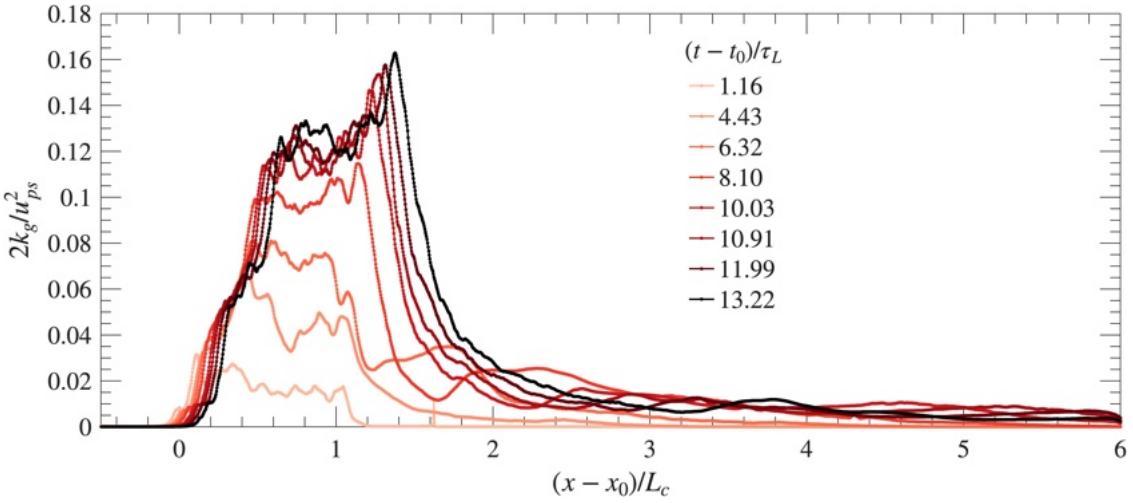

Figure 4.5: Pseudo-turbulent kinetic energy as a function of streamwise length.

4.3.2 One-dimensional statistics

One-dimensional volume fraction profiles of each size particle are shown in Fig. 4.4. Averaging is performed over the two homogeneous (y and z) directions. The volume fraction of large and small particles is given by

$$\phi_{p,\text{large}}(x,t) = \frac{1}{L_y L_z}\int_{L_z}\int_{L_y} \mathcal{I}(\boldsymbol{x},t)\mathrm{d}y\ \mathrm{d}z, \tag{4.1}$$

$$\phi_{p,\text{small}}(x,t) = \frac{1}{L_y L_z}\int_{L_z}\int_{L_y} (1-\alpha(\boldsymbol{x},t))\ \mathrm{d}y\ \mathrm{d}z. \tag{4.2}$$

Here, $\mathcal{I}$ is an indicator function associated with the large particles that is determined from the levelset function defined by Eq. (2.29). $\mathcal{I}=0$ within the volume of large particles (where $\mathbb{G}\leq 0$) and $\mathcal{I}=1$ in the fluid (where $\mathbb{G}>0$).

The volume fraction profiles associated with the large particles is seen to move approximately half the curtain length downstream at the final time. The small particles, on the other hand, are seen to translate four times the curtain length over the same time frame, with some particles traveling as far as six curtain lengths downstream. Shortly after the shock passes through the particles, the small particles compress and the local volume fraction increases. The curtain then spreads as it moves downstream, with the average volume fraction decreasing in time. The passage of a shock through the curtain establishes a pressure gradient across it and the gas velocity decreases/increases behind the reflected/transmitted shock, causing a positive velocity gradient inside the particle curtain [68, 145]. As a result, the relative velocity and the resulting quasi-steady drag force for the particle located at the downstream front of the curtain is larger than at the upstream front, contributing to the expansion of the particle curtain. After the passage of the transmitted shock, the pressure downstream continues to grow slowly due to the compression waves generated from the downstream front of the particle curtain. The upstream pressure however gradually decreases with time, due to expansion waves generated at the upstream curtain edge propagating upstream [68]. This results in a gradual reduction of the initially established pressure gradient reducing over time

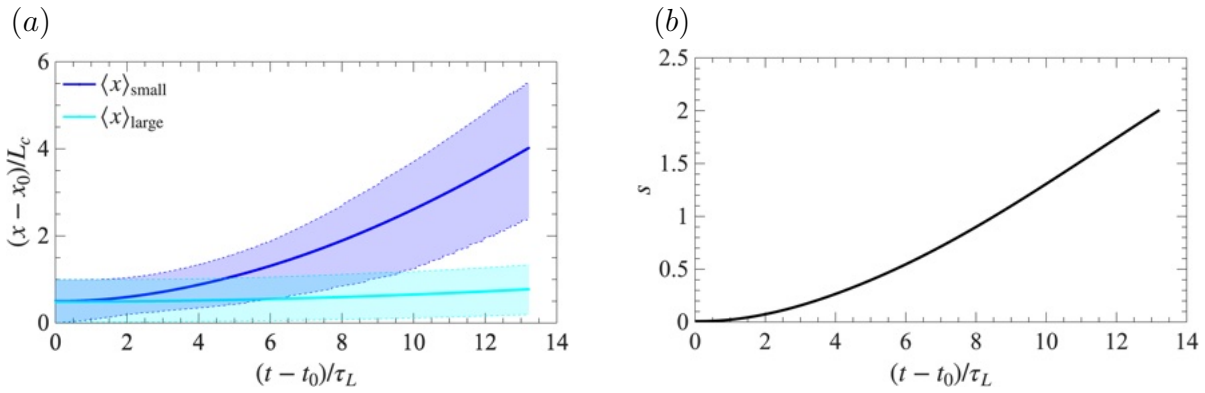

Figure 4.6: Temporal evolution of (a) particle curtain displacement and (b) segregation rate. Dashed lines represent the curtain edges while the shaded regions between them represent the extent of the curtain.

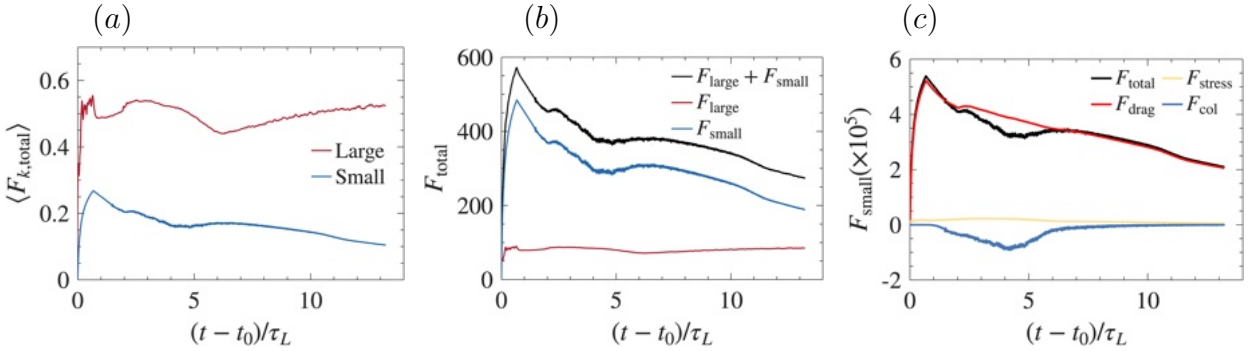

Figure 4.7: Time history of (a) mean streamwise drag force normalized by $0.5N_k\rho_{ps}u_{ps}^2A_k$, ($b$) total streamwise force normalized by $0.5\rho_{ps}u_{ps}^2A_D$, and (c) force contributions acting on the small particles normalized by $0.5\rho_{ps}u_{ps}^2A_d$.

which subsequently causes a diffused volume fraction profile in Fig. 4.4.

Figure 4.5 reports the temporal evolution of the gas-phase velocity fluctuations (pseudo-turbulence). The phase/Favre-averaged velocity is defined as $\widetilde{\boldsymbol{u}}(x,t) = \overline{\mathcal{I}\rho\boldsymbol{u}}/(\overline{\mathcal{I}\rho})$, where the overbar denotes an average in y and z. Using this, local fluctuations are computed as $\boldsymbol{u}''(\boldsymbol{x},t) = \boldsymbol{u}(\boldsymbol{x},t) - \widetilde{\boldsymbol{u}}(x,t)$. The pseudo-turbulent kinetic energy (PTKE) is defined as $k_g(x,t) = \widetilde{\boldsymbol{u}''\cdot\boldsymbol{u}''}/2$. As shown in Fig. 4.5, the PTKE normalized by the post-shock kinetic energy is initially zero and increases with time after the shock passes through the curtain. The majority of this PTKE is generated from the large particles via drag, while the small particles contribute only a minor fraction. As the small particles leave the curtain ($(t-t_0)/\tau_L > 4.43$), PTKE is transported with them, coinciding with the peak volume fraction of the small particles.

4.3.3 Time-dependent statistics

The temporal evolution of the particle curtain displacement and segregation rate are shown in Fig. 5.6. The upstream/downstream edges of the curtain are determined based on the 1% and 99% particle position, respectively. We use $\langle x \rangle$ to denote the average displacement of the entire curtain computed by taking the mean over all particle positions of a given size. Figure 5.6(a) shows this displacement with respect to time. The thick lines in blue and cyan represent the average displacement of the small and large particles, respectively.

The variation in the curtain spread of the large particles is observed to be minimal, while the small particles exhibit a large spread over the times reported.

The relative motion between the differently sized particles can be more aptly quantified using the segregation rate, defined as

$$s = \frac{\langle x \rangle_{\text{small}}}{\langle x \rangle_{\text{large}}} - 1. \tag{4.3}$$

As shown in Fig. 5.6(b), the segregation rate increases monotonically, exceeding a value of 2 over the time considered.

4.3.4 Forces

Particle forces are given in Fig. 4.7. The mean streamwise drag force acting on particle class k is given by

$$\langle F_{k,\text{total}} \rangle = \frac{F_{k,\text{total}}}{0.5 N_k \rho_{ps} u_{ps}^2 A_k}, \tag{4.4}$$

where $F_{k,\text{total}}$ is the total streamwise force acting on particle class k, A_k is the frontal area, and N_k the number of particles ($N_k = N$ for large particles and $N_k = n$ for small particles). The average non-dimensional force exerted on the large particles is around 0.5, more than twice the force experienced by the small particles. This difference is primarily due to variations in slip velocities. Since drag scales linearly with slip velocity, the larger particles, with

their significantly greater inertia, have velocities that are nearly zero. As a result, their slip velocity is closely proportional to u_{ps}. On the other hand, the small particles quickly adjust to the local flow conditions, which results in much lower slip velocities and, consequently, reduced drag. An interesting observation is that the average force acting on small particles decreases with time, while the average force on large particles increases after $(t-t_0)/\tau_L > 6$. At this time, small particles have dispersed downstream away from the large particles, giving rise to large local gas-phase volume fraction and increasing interstitial space in the vicinity of the large particles. The gas phase thus experiences less overall drag and large particles are subjected to higher slip velocity.

Figure 4.7(b) shows the combined total forces acting on the particles. Because $n >> N$, small particles contribute to overall drag forces significantly. The total force exerted on large particles reaches a peak at $(t-t_0)/\tau_L < 1$ and remains relatively constant while the force on small particles reaches a peak at $(t-t_0)/\tau_L \approx 1$ and steadily decays as time progresses because of drag force reduction due to decreasing slip velocity.

The small particles exhibit an interesting trend between $2 < (t-t_0)/\tau_L < 6$. To explore this further, we look at the individual small particle force contributions. Figure 4.7(c) displays the individual force contributions acting on the small particles, as defined in Eq. (2.12). It is evident that nearly the entire force acting on the small particles is due to 'quasi-steady' drag. While the forces attributable to the resolved pressure and viscous stress are minimal, the collision term reduces the overall particle momentum during intermediate times before the particles pass through the large particles. This aligns with the findings in Fig. 4.3(b), where most of the small particles were seen colliding with the upstream side of the large particles.

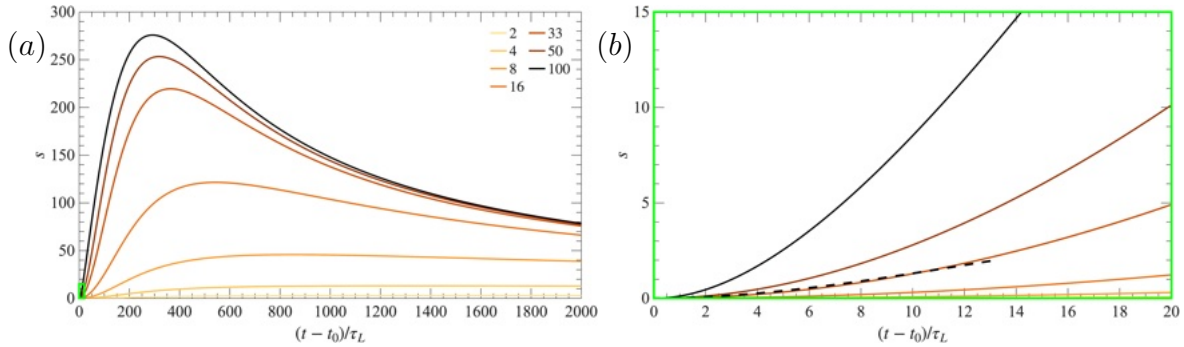

Figure 4.8: (a) Segregation rate for different particle size ratios $D/d \in [2, 100]$ using the model given in Eq. (4.8). An enlarged plot of the early time instances highlighted by the green rectangle is presented in (b). The thick dashed black line indicates the result obtained from the numerical simulation.

4.4 A simple model for size segregation

From the previous section, it can be seen that the 'quasi-steady' drag force, $\boldsymbol{F}_{\text{drag}}$, is the dominant force. If we neglect non-linearities in drag due to Reynolds number, Mach number, and volume fraction effects, a simple model for the average streamwise displacement can be derived. Neglecting two-way coupling, the streamwise fluid velocity is constant with $u = u_{ps}$. Starting with Eq. (2.12), applying these assumptions and averaging yields

$$\frac{d\langle u_p \rangle}{dt} = \frac{u_{ps} - \langle u_p \rangle}{\tau_p}. \tag{4.5}$$

Integrating the above equation and assuming the particles begin at rest ($\langle u_p \rangle(t = 0) = 0$), yields an analytic expression for the average particle velocity:

$$\langle u_p(t) \rangle = u_{ps}(1 - e^{-t/\tau_p}). \tag{4.6}$$

Integrating once more yields an analytic expression for the average particle displacement:

$$\langle x(t) \rangle = \langle x_0 \rangle + u_{ps}t - \tau_p u_{ps}(1 - e^{-t/\tau_p}), \tag{4.7}$$

where $\langle x_0 \rangle$ is the initial position of the particle curtain, taken to be $L_c/2$. The impact of particle size is incorporated through τ_p.

Plugging this expression into Eq. (4.3), an analytic expression for the segregation rate is

$$s = \frac{\langle x_0 \rangle + u_{ps}t - \tau_{p,\text{small}} u_{ps}(1 - e^{-t/\tau_{p,\text{small}}})}{\langle x_0 \rangle + u_{ps}t - \tau_{p,\text{large}} u_{ps}(1 - e^{-t/\tau_{p,\text{large}}})} - 1, \tag{4.8}$$

where $\tau_{p,\text{small}} = \rho_p d^2/(18\mu)$ and $\tau_{p,\text{large}} = \rho_p D^2/(18\mu)$. The reference gas-phase viscosity (μ_∞) is used to compute τ_p.

The algebraic model can predict size segregation trends for various particle diameter ratios D/d by adjusting τ_p. Figure 4.8(a) shows the segregation rate for size ratios $D/d \in [2, 100]$. As expected, the segregation rate is more pronounced at higher size ratios. The process can be divided into distinct stages. Initially, size segregation occurs rapidly, especially when $(t-t_0)/\tau_L < 200$. A peak in segregation rate is observed, with its amplitude scaling according to D/d and occurring earlier as the size ratio increases. After the large particles begin to move, they ultimately catch up with the smaller particles, leading to a steady state where $s = 0$. Figure 4.8(b) shows the segregation rate during the initial transient. The simple model is compared to the numerical simulation (with $D/d = 33$). The overall trend is accurately predicted by the model, although any arising discrepancy can be attributed to the neglected nonlinearities in drag and volume fraction effects.

4.5 Conclusion

The hybrid framework proposed in Chapter 2 was applied to a simulation of a planar shock wave interacting with a bidisperse distribution of particles to evaluate size segregation and particle curtain displacement. One-dimensional statistics of particle volume fraction field reported revealed a pronounced spread of small particles over large distances as compared to the large ones. Moreover, majority of the PTKE was found to be produced by the large-particle wakes, and small particles only contributed to a minor portion away from the large

particles. A simple model for the segregation report is reported and compares well with the numerical simulation.

4.6 Acknowledgments

A portion of this work was funded by Sandia National Laboratories, a multi-mission laboratory managed and operated by National Technology & Engineering Solutions of Sandia, LLC, a wholly owned subsidiary of Honeywell International Inc., for the U.S. Department of Energy's National Nuclear Security Administration under contract DE-NA0003525. This paper describes objective technical results and analysis. Any subjective views or opinions that might be expressed in the paper do not necessarily represent the views of the U.S. Department of Energy or the United States Government. We would also like to acknowledge partial funding of this project under SBIR Award No. HDTRA125P0006. This work used Expanse systems at UCSD through an allocation from the from the Advanced Cyberinfrastructure Coordination Ecosystem: Services & Support (ACCESS) program, which is supported by NSF.

CHAPTER 5

Parametric Study of Shock-Induced Size Segregation of Bidisperse Particles

Note: This chapter has been published in the journal of *American Institute of Aeronautics and Astronautics* [126]. It has also been presented as "Paper 2025-1878" at the 2025 AIAA SciTech Forum, Orlando, FL, January 6–10, 2025. Data and figures have been used with all co-authors' consent.

5.1 Abstract

The interaction of a planar shock wave with a suspension of bidisperse particles is examined using high-fidelity simulations over a range of shock Mach numbers (M_s), particle volume fractions (Φ_p), and particle diameter size ratios (D/d) between large (D) and small (d) particles. The study aims to quantify the effects of these parameters on size segregation and particle curtain spread. Results indicate that size segregation increases with increasing M_s and decreasing Φ_p. Additionally, segregation exhibits a weak proportionality to the size ratio D/d across the range of conditions and time horizons considered. Streamwise profiles of the mean particle volume fraction reveal a pronounced downstream spread of smaller particles compared to larger ones.

5.2 Introduction

Shock-induced particle dispersal is a phenomenon observed in a wide range of environmental and engineering applications, from volcanic eruptions [69] to mining safety [116, 152], pulsed detonation engines [20, 113], heterogeneous detonation [151], and rocket propulsion [14, 77]. Understanding the underlying mechanisms is crucial for predicting and mitigating the effects of explosive events, optimizing propulsion system performances, and enhancing safety standards in the aforementioned contexts. These applications involve strong shocks, local regions of flow instabilities [106], a wide range of particle concentrations, particle sizes, and four-way coupling involving gas-particle and particle-particle interactions.

The applications mentioned above typically involve particles with a wide size distribution. Aerodynamic drag forces and particle-particle interactions through collisions and wakes scale with particle diameter [18], contributing to spatial size segregation in various ways. Finite slip velocity between the phases generates net mean aerodynamic forces on each particle, which give rise to relative mean motion between particles of different sizes, thereby promoting size segregation [76]. However, aerodynamic forces acting on each particle can also induce inter-particle velocity fluctuations (wakes) that generate random particle motion (granular temperature), enhancing collisions and potentially hindering size segregation [74]. Most studies on particle segregation focus on incompressible flow regimes, but high-speed, compressible flows with shocks are expected to amplify these effects. This paper focuses on the dynamics of bidisperse systems in the presence of shocks.

Common approaches for modeling dispersed two-phase flows include particle-resolved direct numerical simulation (PR-DNS) [76, 128], Euler–Euler (EE) [9] and Euler–Lagrange (EL) [16] methods. Both EE and EL are coarse-grained modeling techniques that rely on accurate models for interphase exchange and inter-particle interactions. PR-DNS, whereby sufficient resolution is applied to capture all of the relevant scales of motion, specifically, gas-phase fluctuations induced by the presence of particles (termed pseudo-turbulent kinetic energy or PTKE) is a comprehensive approach to analyze flow-induced size segregation, but

the associated computational cost can be prohibitive. These limitations confine studies to particles with low size ratios of $O(1)$ [22, 74], as sufficient resolution is necessary to capture boundary layers for all size particles.

This chapter employs a framework that balances cost with accuracy, enabling the simulation of shocks through bidisperse suspensions of particles with size ratios ranging between 12 and 40. An EL method is employed to handle small particles, where the particle diameter is comparable to the grid spacing, and drag models are incorporated in the particle equations of motion. PR-DNS is used for large particles, providing sufficient resolution to resolve fluid stresses at the particle surface. Momentum transfer between particles is managed using a soft-sphere collision model combined with a novel neighbor detection algorithm. This hybrid scheme is used to quantify the effects of shock Mach number, particle volume fraction, and particle diameter size ratio on particle curtain spread and size segregation.

5.3 Simulation Setup

To investigate shock-induced particle size segregation, we consider a two-dimensional domain with a planar shock interacting with a curtain of bidisperse particles as shown in Fig. 5.1. The gas-phase conditions and particle parameters were chosen to match the experimental setup at Sandia [144]. The length of the particle curtain is $L_c = 2.5$ mm and contains a mixture of large and small particles with a large particle diameter $D = 300$ μm and small particle diameter d that will be varied based on the desired size ratio defined as the ratio of the diameter of the large particle to the small particle (D/d). Particles are randomly distributed within the curtain while avoiding overlap. The total volume fraction within the curtain is varied from $\Phi_p = 0.05$ to 0.2, with a 75% make-up of large particles and 25% of small particles by volume. The particle density is $\rho_p = 2520$ kg/m^3, corresponding to soda lime. The shock Mach number is defined as $M_s = u_s/c$, where u_s is the shock speed and c is the speed of sound. The pre-shock conditions are taken to be air at standard temperature

and pressure with $[P_\infty, \rho_\infty, u_\infty] = [82.7\ \text{kPa},\ 1.2\ \text{kg/m}^3,\ 0\ \text{m/s}]$. The post-shock conditions are obtained from the Rankine–Hugoniot jump conditions and the associated variables are represented using the subscript '*ps*'. The post-shock Mach number is defined using the post-shock velocity and speed of sound as $M_{ps} = u_{ps}/c_{ps}$. A summary of the simulation parameters is given in Table 5.1.

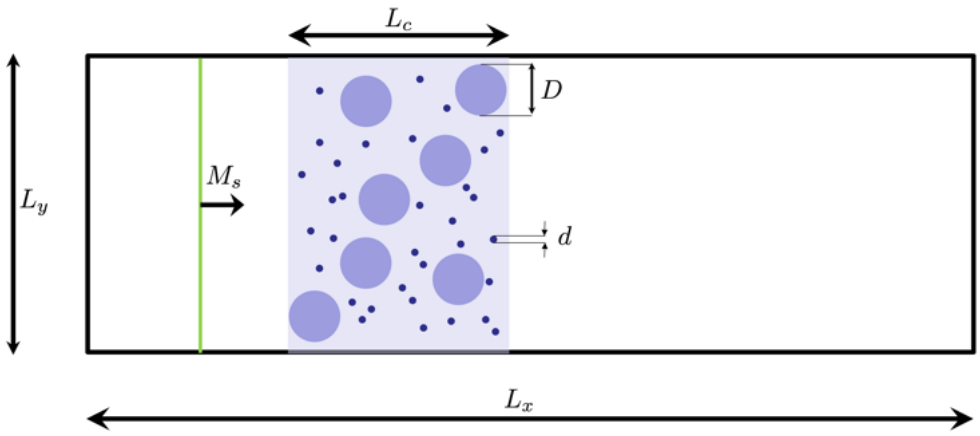

Figure 5.1: Schematic of the simulation configuration.

The computational domain spans $[L_x \times L_y] = [99 \times 12]D$ discretized using a Cartesian grid with grid spacing $\Delta x \sim d$. This restriction is mainly the artifact of using a Lagrangian particle tracking approach. Closure models for drag and other interphase exchange terms are often formulated based on volume averages significantly larger than the particle diameter. A general rule of thumb is that the characteristic averaging volume must be at least an order of magnitude larger than the volume of a particle, resulting in grid spacing $\Delta x > 1.74d$ [100]. However, explicitly filtering the interphase exchange terms, as described in § 2.4.1, enables $\Delta x \sim d$. The number of grid points in the streamwise and spanwise directions, i.e. $[N_x \times N_y]$ is determined based on the grid refinement study in § 5.4.1. The curtain length is set to $L_c = 8.3D$, with a downstream length extending to $10L_c$ to allow sufficient space for the particles to segregate. Periodic boundary conditions are enforced in the spanwise (y) direction.

Table 5.1: Parameters considered in the simulations where N corresponds to the number of large particles of diameter D and n corresponds to the number of small particles of diameter d.

	Case no.	M_s	Φ_p	D/d	M_{ps}	N	n	$N_x \times N_y$
	0	1.7	0.1	33	0.77	9	3346	3268×396
	1	1.2	0.1	33	0.29	9	3522	3268×396
	2	2.1	0.1	33	1.02	9	3522	3268×396
	3	3.0	0.1	33	1.36	9	3522	3268×396
	4	2.1	0.1	20	1.02	9	1268	1981×240
	5	2.1	0.1	40	1.02	9	5072	3961×480
	6	2.1	0.05	33	1.02	4	1761	3268×396
	7	2.1	0.2	33	1.02	19	7045	3268×396

Table 5.2: Simulation parameters used in the grid refinement study.

	Case	$D/\Delta x$	**Grid size**
	A0	12	697×144
	B0	20	1161×240
	C0	30	1741×360
	D0	40	2321×396

5.4 Numerics

The numerics for these simulations are summarized in Chapter 2. A ghost-point immersed boundary method (IBM) is used to enforce no-slip, adiabatic boundary conditions at the surface of the large particles. Small particles are handled using a volume-filtered Euler–Lagrange (VFEL) approach. The framework is implemented within `jCODE`, a high-order, energy-stable multiphase flow solver [15].

5.4.1 Grid resolution

Because the numerical framework combines a ghost-point IBM approach with a volume-filtered Euler–Lagrange method, the diameter ratio needs to be carefully chosen as the smaller particle is required to be smaller than the grid spacing while the larger particles need a sufficient number of grid points to resolve fluid boundary layers. In this section, a grid refinement study is performed for a curtain of monodisperse particles with $D/\Delta x \in$

[12, 20, 30, 40] using the IBM approach described above to determine the minimum number of grid points needed to resolve the large particles.

Figure 5.2 shows the temporal evolution of the curtain edge displacement and gas-phase velocity fluctuations for the grid resolutions listed in Table 5.2. In each case, a shock Mach number of $M_s = 1.7$ was chosen with a total particle volume fraction of $\Phi_p = 0.2$, which results in 25 particles of size D within the curtain. Time is normalized by $\tau_L = L_c/u_{ps}$, where u_{ps} is the post-shock velocity. The initial time t_0 is taken as the instant the shock impinges on the curtain and x_0 is the initial position of the curtain's upstream edge.

The streamwise displacement of the upstream and downstream edges of the curtain is shown in Fig. 5.2a. The evolution of the upstream edge remains consistent across all grid sizes considered. While some discrepancies are noted in the downstream edge across different cases, the overall agreement is satisfactory.

To evaluate the sensitivity of the grid to local gas-phase velocity fluctuations, we analyze the time evolution of pseudo-turbulent kinetic energy (PTKE), defined as $k_g(t) = \widetilde{u_i'' u_i''}/2$, where $u_i''(t) = u(\boldsymbol{x}, t) - \widetilde{u}(t)$ in Fig. 5.2b. The tilde represents a spatial Favre average, i.e., $\widetilde{u}(t) = \langle \mathcal{I}\rho \boldsymbol{u} \rangle / \langle \mathcal{I}\rho \rangle$. The indicator function $\mathcal{I}$ is 1 within the fluid and 0 in the large particles. Angled brackets represent a volume average across the streamwise and spanwise directions. PTKE is normalized by the post-shock kinetic energy. The trends in PTKE evolution are consistent for each grid size considered. There is initially no PTKE. When the shock first interacts with the curtain, the local volume fraction is maximum, and PTKE is generated through drag in the form of wakes. PTKE rapidly increases as the flow establishes within the curtain. Due to the finite inertia of the particles, curtain spreading is delayed. As the curtain spreads, the local volume fraction drops, and so does the PTKE. While the initial transient trends are similar ($t/\tau_L <= 7$) across all cases, the intermediate times ($7 < t/\tau_L \sim 16$) show some discrepancy. The lowest resolution case underpredicts PTKE by $\sim 10\%$. Thus, we conclude that a value of $D/\Delta x > 10$ is satisfactory.

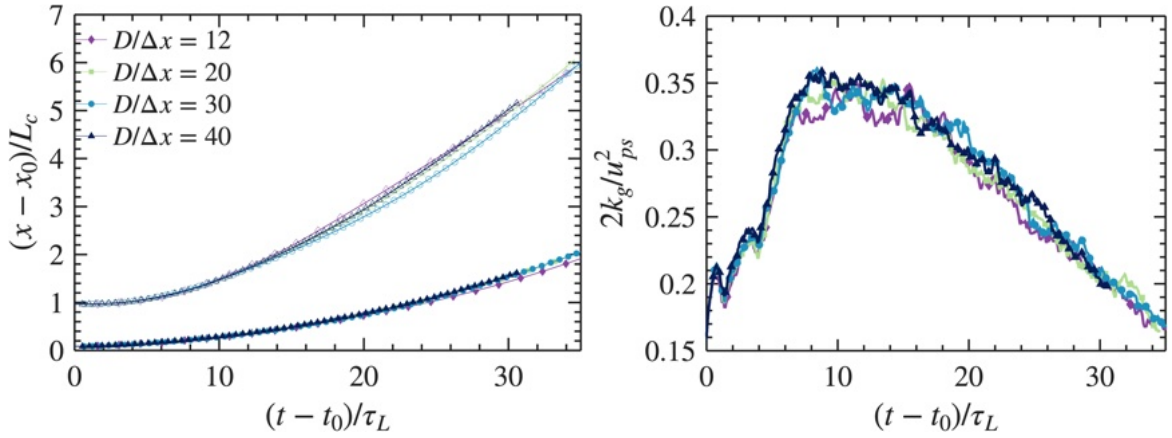

(a) Particle curtain edge displacement.

(b) Average PTKE.

Figure 5.2: Evolution of curtain edge displacement and ptke for large/IBM particles. Filled markers: Upstream edge, Unfilled: Downstream edge.

5.5 Results

5.5.1 Case 0 analysis

A visualization of shock-induced size segregation for Case 0 ($M_s = 1.7$, $\Phi_p = 0.1$, $D/d = 33$) is given in Fig. 5.3, which shows contours of the local gas-phase Mach (Ma) and the position of large/small particles at four different instances of time. The small particles are scaled up for better visibility. At the instant the incident shock impinges the curtain, a transmitted shock passes through the particles in the positive streamwise direction. Multiple shocklets form at the surface of each particle near the upstream edge of the curtain and coalesce into a reflected shock that travels upstream. At $t/\tau_L = 0.84$, the transmitted shock has passed the downstream curtain edge, inducing wakes that generate gas-phase velocity fluctuations. Small particles accelerate downstream significantly faster than the large particles. A fraction of the small particles become trapped in the wakes of large particles which hinder size segregation. At $t/\tau_L = 3.04$, visible segregation between the two particle classes is observed. Small particles at the downstream edge compress, while upstream, the volume fraction is significantly lower. The downstream edge appears to remain intact while a distinct upstream edge is almost non-existent for the smaller particles. Because the particle response time (and

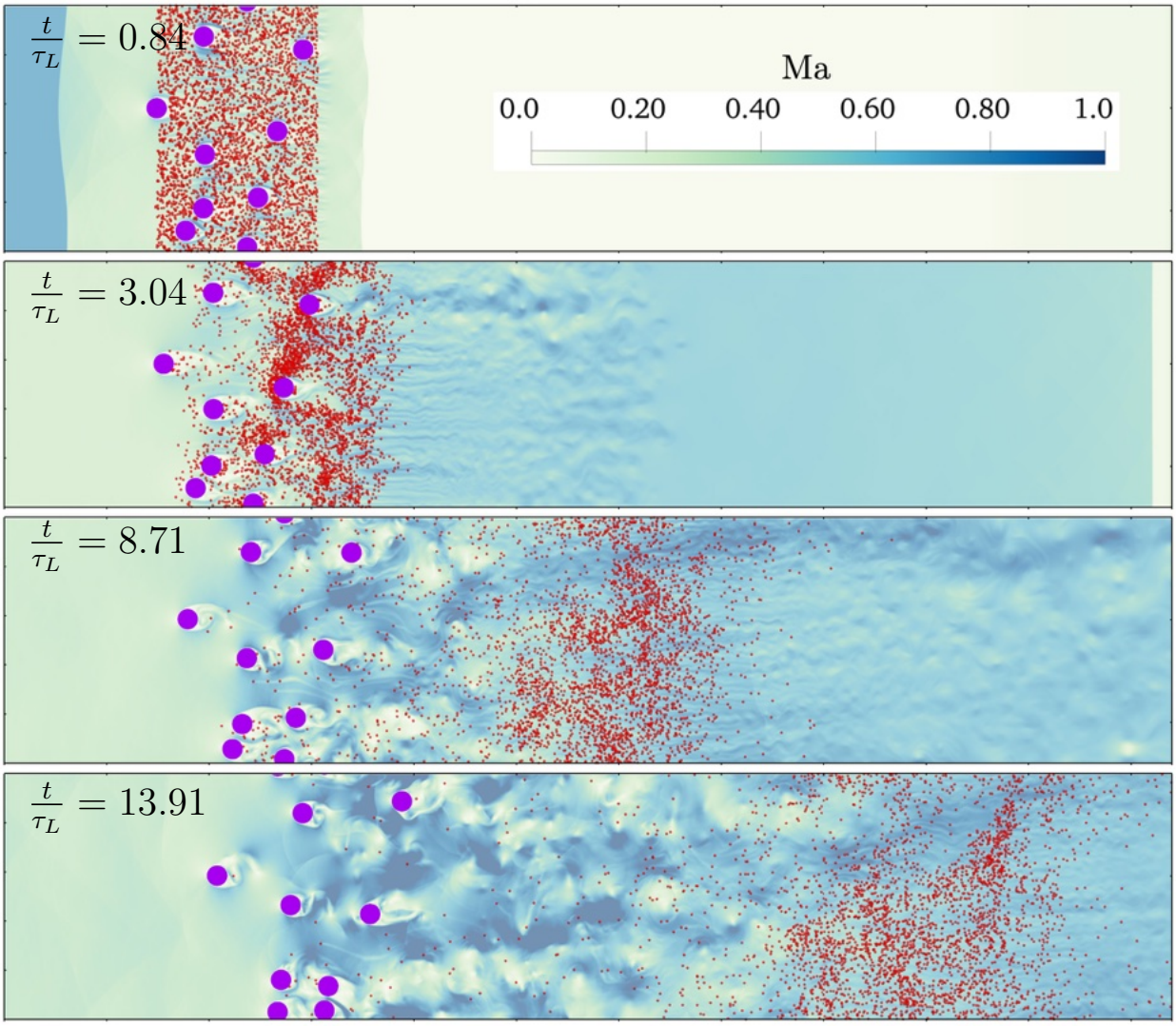

Figure 5.3: Contours of local gas-phase Mach number for Case 0 at different time instances. Large particles (purple circles), small particles (red circles; not to scale).

thus the Stokes number) scales with the square of the diameter, the larger particles are far more inertial and respond much slower to the impinging shock. Small particles move through the interstitial spaces in the curtain, accumulating towards the midstream region. At a later time ($t/\tau_L \sim 8.71$), the small particles have traveled far downstream and are more spread out. The small particles reach the downstream boundary of the domain at the final time instant ($t/\tau_L = 13.91$). In contrast, the large particles have not yet moved one curtain length distance downstream of their initial position.

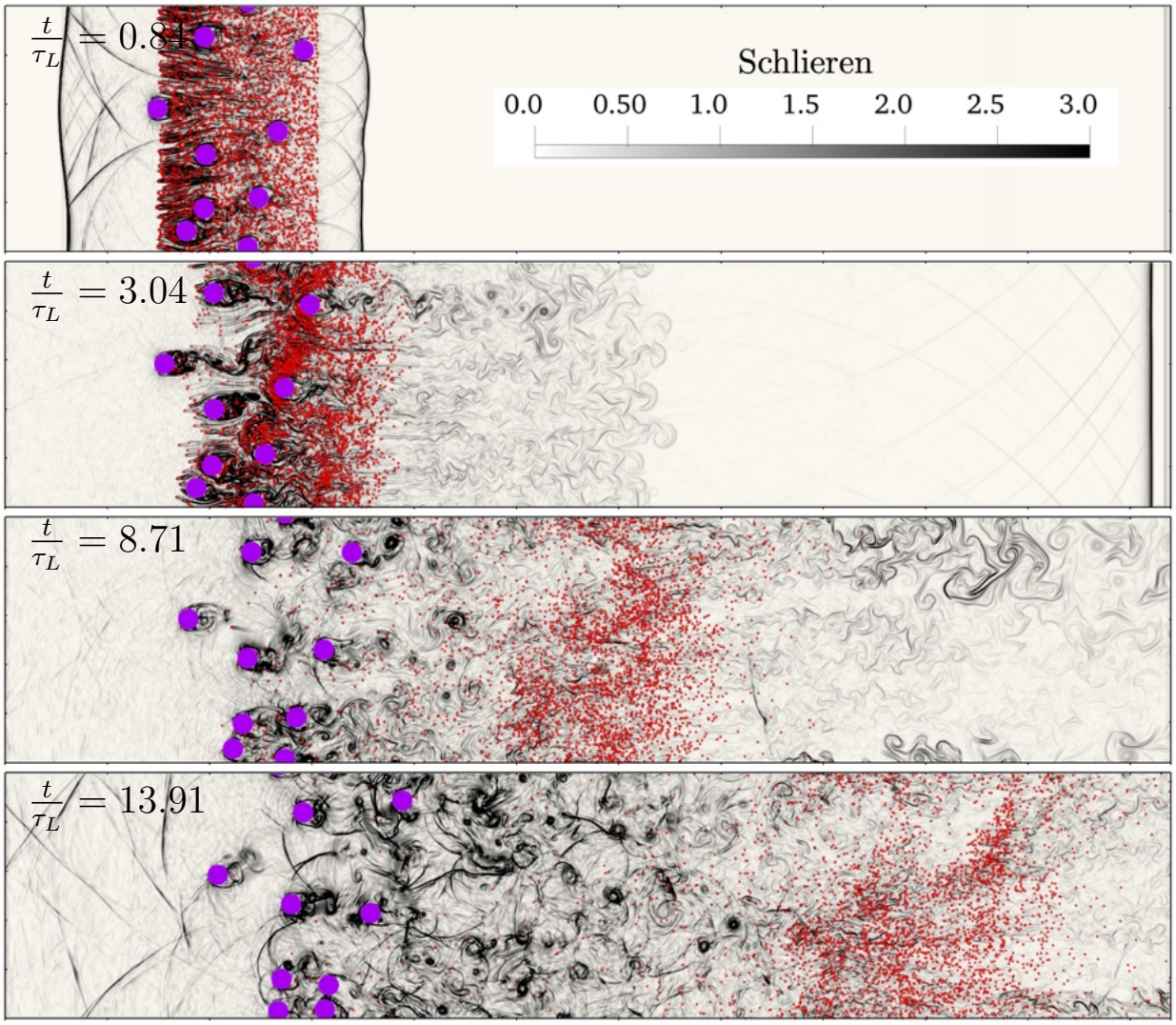

Figure 5.4: Numerical Schlieren (black/white) for Case 0 at different time instances. Large particles (purple circles), small particles (red circles; not to scale).

Figure 5.4 shows instantaneous snapshots of numerical Schlieren, highlighting the reflected/transmitted shocks, shocklets, and downstream wakes. The numerical schlieren represents the magnitude of the density gradient $\|\nabla\rho\|D/\rho_\infty$. Regions of black are indicative of high compressibility. The transmitted and reflected shocks can be seen in the first frame. Small particles initially follow streamlines with high density gradients (black curves) generated by the large particles ($t/\tau_L = 0.84, 3.04$).

The average displacement of the upstream and downstream curtain edges for each particle

class is reported as a function of time. The upstream/downstream edges of the curtain are determined based on the 1% and 99% particle position, respectively. We use $\langle x \rangle$ to denote the average displacement of the entire curtain. The evolution of the displacement of curtain edges gives a general idea of the curtain spread. The curtain edge averages are computed in the same manner as § 5.4.1. Figure 5.5a shows this displacement with respect to time. The thick lines in red and purple represent the average displacement of the small and large particles, respectively. The shaded regions represent the spread between the edges with the lower bound indicating the upstream edge and the upper bound indicating the downstream edge. The variation in the curtain spread of the large particles is observed to be minimal, while the small particles exhibit a large spread over the times reported.

The relative motion between the differently sized particles can be more aptly quantified using the segregation rate, defined in Eq. (4.3). As shown in Fig. 5.5b, the segregation rate increases monotonically, exceeding a value of 2 over the time considered.

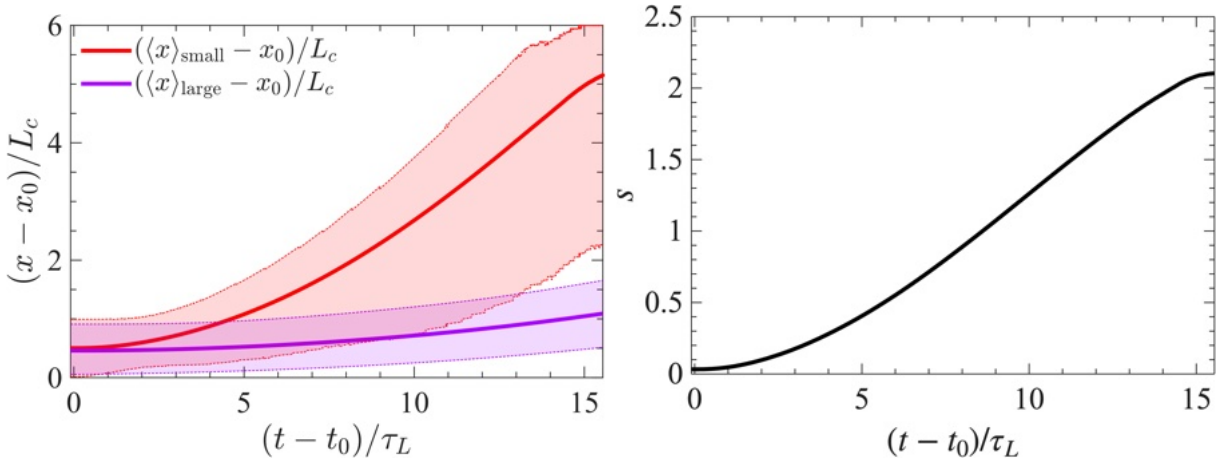

(a) Particle curtain spread.

(b) Segregation rate.

Figure 5.5: Temporal evolution of the curtain spread and segregation rate for Case 0. Red and purple shaded regions indicate the extent of small and large particle spread respectively.

5.5.2 Parametric study

The effects of varying the shock Mach number, particle volume fraction, and particle diameter ratio on segregation ratio are reported in this section. All the figures adhere to the color scheme and case notation described in Table 5.1. Cases 1-3 indicate the trends with increasing M_s, while cases 4, 2, and 5 represent increasing diameter ratios, D/d. The diameter of the large particles is held constant, implying that d is decreased to increase D/d, and vice versa. Cases 6, 2, and 7 represent the trends with increasing Φ_p.

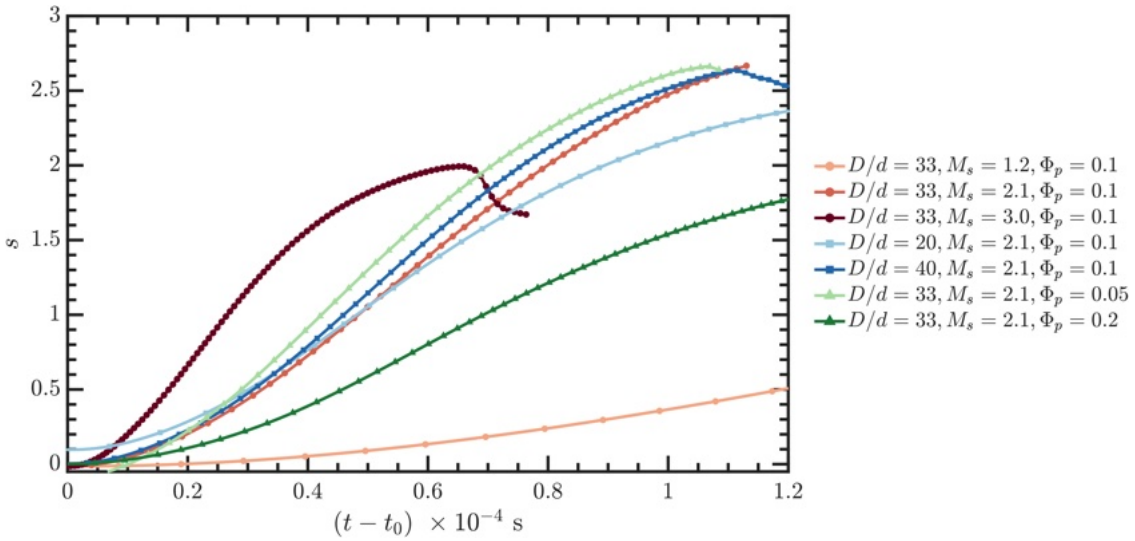

Figure 5.6: Segregation rate (4.3) as a function of dimensional time for the cases listed in Table 5.1.

Figure 5.6 shows the segregation of particles for all the cases simulated. An increase in M_s from 1.2 to 3.0 resulted in the most pronounced enhancement in size segregation among particles. This suggests that the drag forces, influenced by the induced velocity acting on smaller particles, substantially contributed to the overall segregation dynamics. The differences in segregation rate are pronounced. With $M_s = 1.2$ (Case 1), a final value of $s = 1$ is achieved, while for $M_s = 2.1$ (Case 2), s exceeds values of 2.5. The fastest case with $M_s = 3$ exhibits maximum segregation until $(t - t_0) \sim 670$ µs, at this point small particles begin to leave the domain and the large particles are moving downstream. The effect of the diameter ratios D/d considered is noted to be minimal for the range considered.

Larger diameter ratios imply smaller d. The smaller particles have greater acceleration and, consequently, increased segregation is observed. Varying the particle concentration has a converse effect. Increased particle concentrations reduce the interstitial spaces for the small particles to navigate through, which consequently increases inter-particle collisions, which acts to reduce segregation.

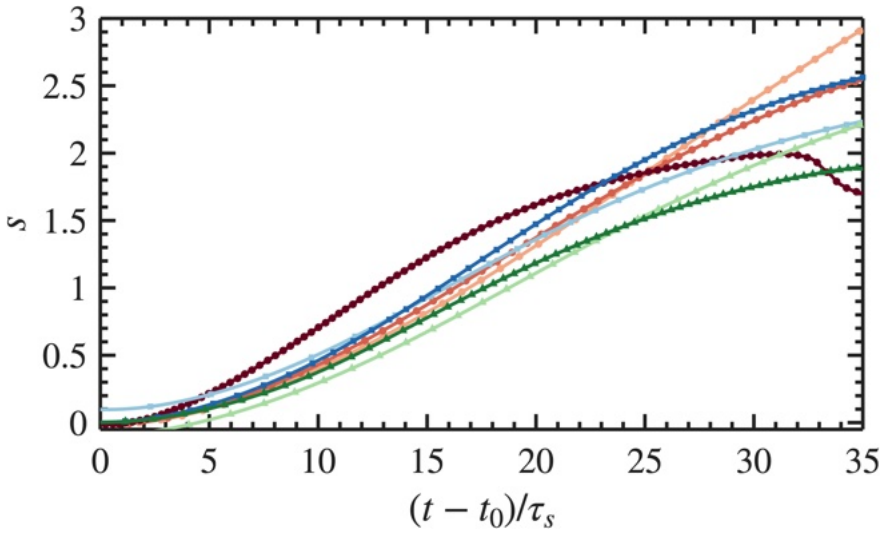

Figure 5.7: Segregation rate (4.3) as a function of time normalized by (5.1). Color scheme same as Fig. 5.6.

The simulations reveal large spread in segregation rates across the range of parameters. Beyond the initial transient, s is approximately linear in time. Based on the simulation results, the segregation rate is found to scale like:

$$s \propto \frac{u_{ps}}{L_c} \frac{(1 - d/D)}{(\Phi_p M_s)^{0.4}} t = \frac{t}{\tau_s}. \tag{5.1}$$

As shown in Fig. 5.7, this yields a reasonable collapse of the segregation rates. The scaling ensures that $s = 0$ in the limit $d/D = 1$ (monodisperse).

Figure 5.8 shows the variation of particle curtain spread defined as $\delta(t) = x_{\text{downstream}} - x_{\text{upstream}}$. The spread normalized by initial curtain length, for large particles, varies between $0.6 \leq \delta/L_c \leq 2$, while for small particles, ranges from $0.6 \leq \delta/L_c \leq 5$. It is interesting to

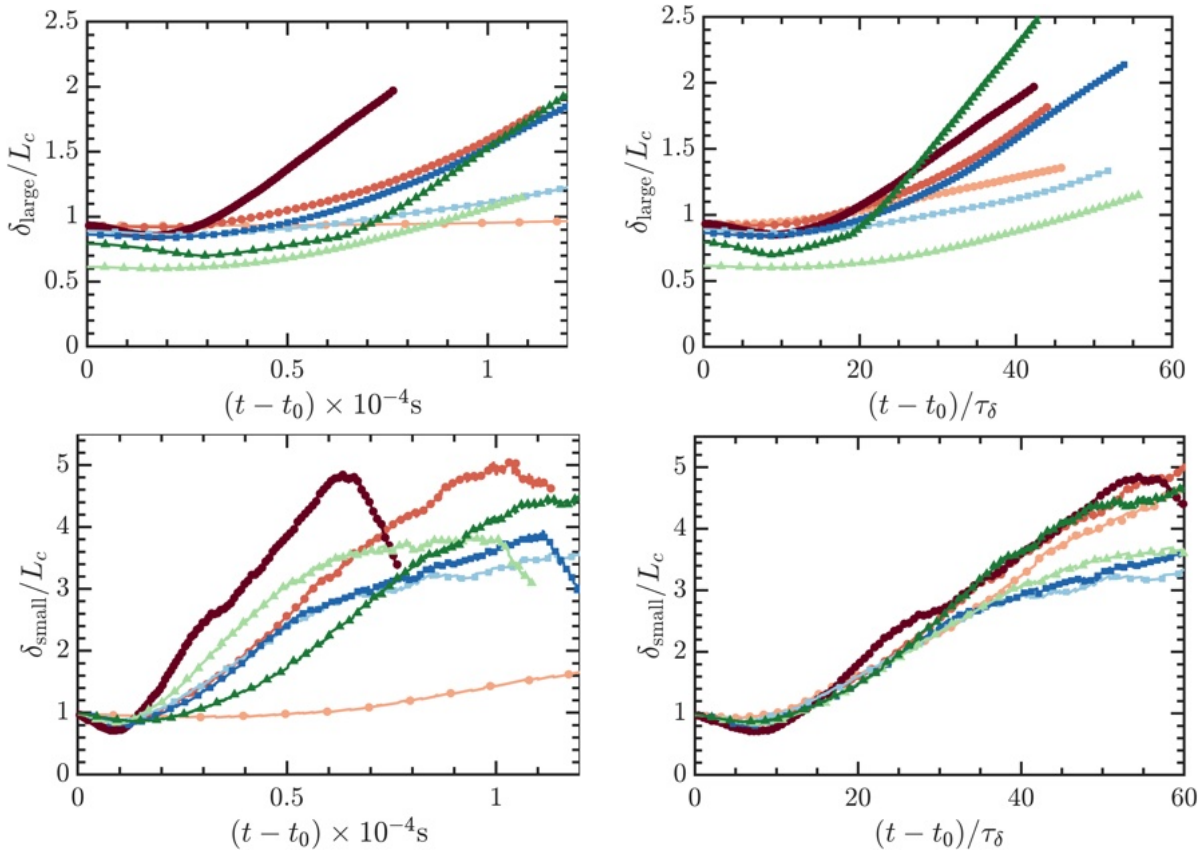

Figure 5.8: Curtain spread rates for large particles (top row) and small particles (bottom row) as a function of dimensional time (left) and normalized time (right).

note that at early times, $(t - t_0) \leq 150$ μs, the curtain spread of small particles decreases with time. This can be attributed to the relatively high acceleration of the particles near the upstream edge due to drag forces in comparison with those near the downstream edge. These fast particles travel downstream and accumulate in the center of the curtain, while the downstream edge particles are slow to respond, resulting in a temporarily narrowing curtain. There are no clear monotonic trends observed with D/d. With increasing M_s, the spread for small particles exhibits a significant jump from 1.2 to 2.1 but behaves similarly between 2.1 and 3.0. Time for the δ_i ($i \in [\text{small}, \text{large}]$) plots is normalized using a scaling factor

$$\tau_\delta = L_c(\Phi_{p,i} M_s)^{0.4}/u_{ps}, \tag{5.2}$$

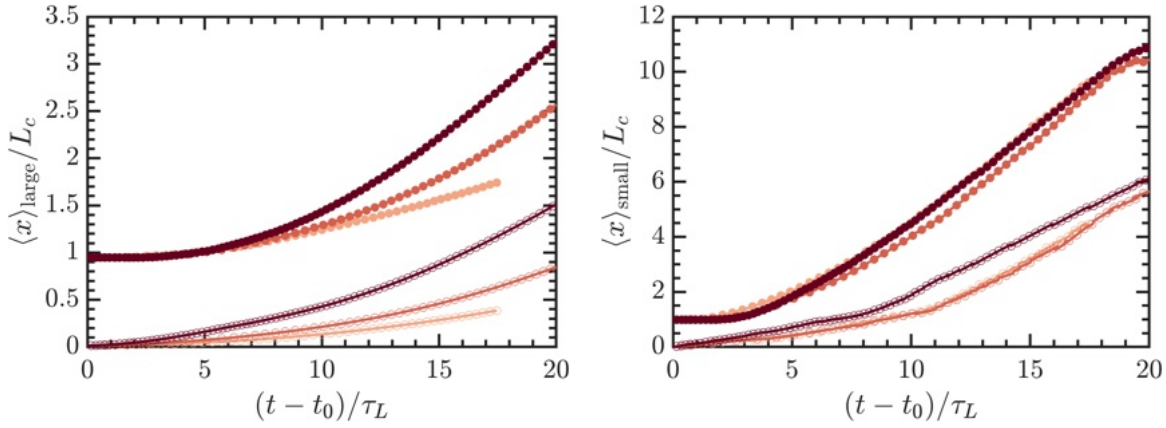

Figure 5.9: Average curtain edge displacement with time as a function of M_s. The line types are the same as Fig. 5.6.

where $\Phi_{p,i}$ is either the small or the large particle volume fraction. This scaling results in an effective collapse of the spread rate for small particles.

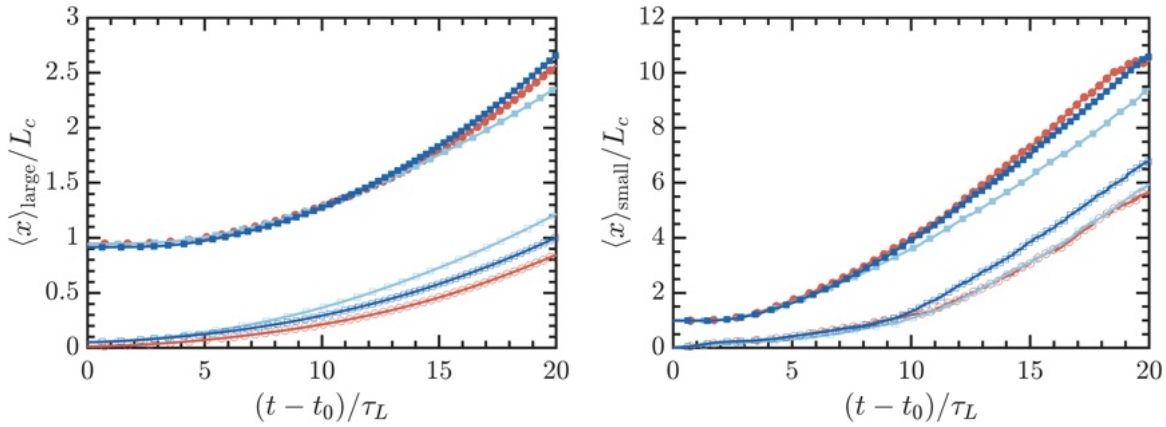

Figure 5.10: Average curtain edge displacement with time as trends of D/d. The line types are the same as Fig. 5.6.

Figs. 5.9–5.11 show individual trajectories of the upstream and downstream curtain edges for large (left column) and small (right column) particles as functions of M_s, D/d, and Φ_p, respectively. Overall, there is an expansion in the curtain size. As seen in Fig. 5.9, the upstream edges have a steeper slope at early times which explains the decrease in curtain spread in the earlier figure. After $(t - t_0)/\tau_L \sim 5$, the downstream edge moves faster. This

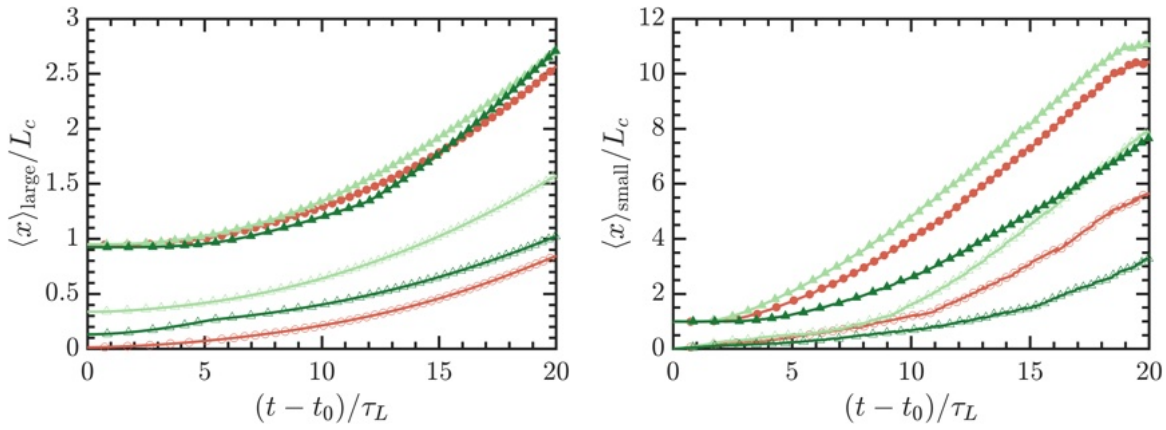

Figure 5.11: Average curtain edge displacement with time as trends of Φ_p. The line types are the same as Fig. 5.6.

is in alignment with previous experimental observations [136]. The passage of a shock wave through the curtain causes the flow to expand and pressure and density to drop while the gas-phase velocity rises, hence increasing the drag at the downstream edge relative to the upstream edge. The higher drag at the downstream edge accelerates the particles in this region faster than those at the upstream edge. Thus, the edge displacements increase with increasing M_s. The edge displacements remain relatively constant with particle size ratios D/d for both the particle classes (see Fig. 5.10). Any slight variation could be the effect of differences in random configurations of the particles. Additionally, a strong sensitivity to Φ_p can be observed in Fig. 5.11. With an increase in Φ_p, edge displacements appear to decrease, which is contrary to the observations from experimental studies with monodisperse particle configurations [68]. Cases 2 and 7 have a higher overall volume fraction, which reduces the available interstitial space. This reduction leads to more frequent collisions and increases the likelihood of small particles becoming trapped in the wakes of larger ones, thereby inhibiting segregation. In conclusion, M_s and Φ_p are observed to impact segregation and curtain spread dynamics significantly.

One-dimensional particle volume fields are computed by taking the spatial average over

the spanwise direction via

$$\alpha_{p,\text{large}}(x,t) = \frac{1}{L_y}\int_y \mathcal{I}(\boldsymbol{x},t)\mathrm{d}y; \quad \alpha_{p,\text{small}}(x,t) = \frac{1}{L_y}\int_y (1-\alpha(\boldsymbol{x},t))\ \mathrm{d}y. \tag{5.3}$$

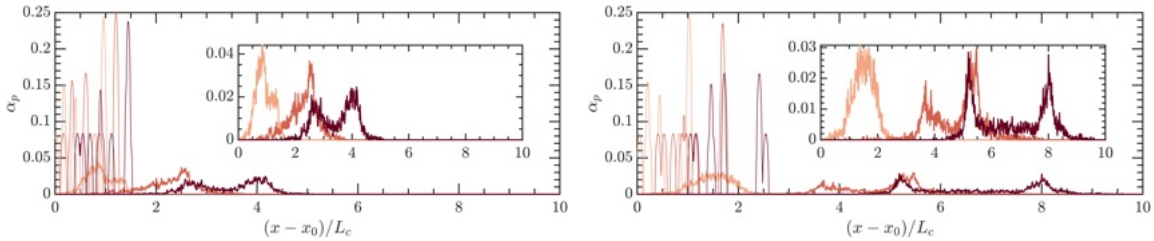

(a) Varying M_s

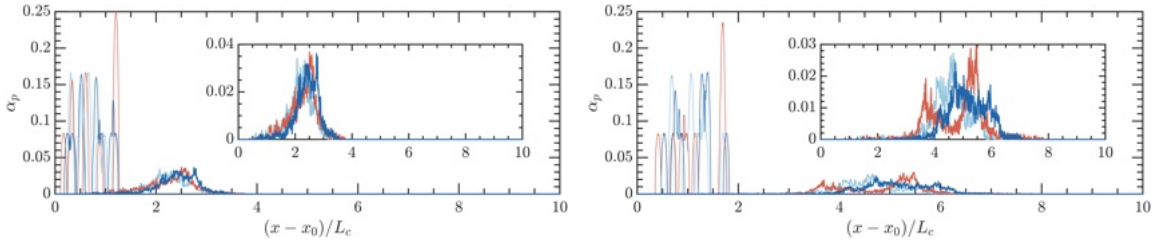

(b) Varying D/d

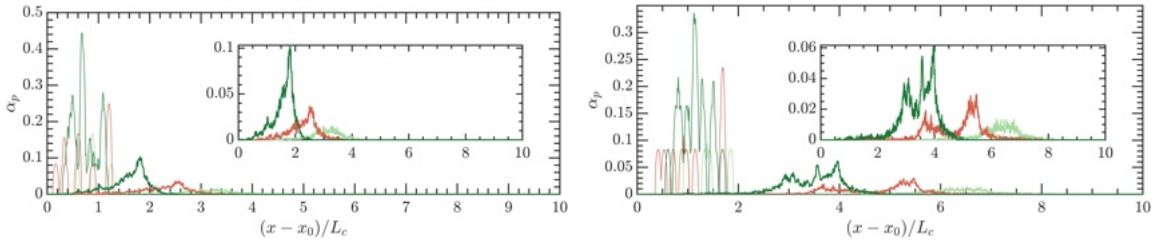

(c) Varying Φ_p

Figure 5.12: Volume fraction of small (thick) and large (thin) particles at $(t-t_0)/\tau_L \sim 7.59$ (left) and $(t-t_0)/\tau_L \sim 12.26$ (right). Inset shows $\alpha_{p,\text{small}}$. Refer to Fig. 5.6 for colors.

Figure 5.12 shows the volume fraction profiles at two different time instances. The inset shows the small particle volume fraction fields for clarity. Figure 5.12a illustrates the strong effect of M_s on dispersion of small particles. More importantly, the small particle curtains for $M_s = 2.1, 3$ exhibit a stretching-like behavior with time, in the sense that particles accumulate around the edges and thin out in the central region leading to a bimodal distribution. We

posit that when the shock wave traverses the particle curtain, the smaller particles located at the upstream edge initially undergo acceleration and begin to move downward through the curtain. The passage of the shock generates wakes due to the presence of larger particles within the curtain and chokes the flow at the downstream edge. This region imparts significant acceleration to the small particles. Furthermore, as these small particles travel through the suspension, they are subjected to increased collisions with the larger particles and wake entrainment, which result in the formation of concentrated peaks in the volume fraction profiles at the curtain edges, while in the central region, the particles tend to diffuse out. Figure 5.12b further shows that for the range of diameter ratios considered, statistics remain largely invariant. Figure 5.12c demonstrates the dilute particle cloud for small particles travels further due to fewer collisions. The more heavily concentrated Case 7 evolves much slower in comparison as small particles take longer to overcome collisions and the wake entrainment to commence segregation.

5.6 Conclusion

This work investigates the interaction of a planar shock wave with a bidisperse mixture of solid, rigid particles. We presented a numerical framework that combines an immersed boundary method for large particles with Lagrangian particle tracking for small particles. A soft-sphere collision model with efficient neighbor detection is employed to handle momentum transfer between all particles. The evolution of particle curtain spread and segregation rate with time were presented for a wide range of shock Mach numbers, diameter ratios, and volume fractions. While the curtain spreads for large particles across all cases were noted to be minimal ($\delta/L_c \approx 1 - 1.5$), small particles were found to have significant spreads of $\delta/L_c \approx 4$. It was observed that M_s and Φ_p have the most significant effect on shock-induced size segregation. A scaling with volume fraction correction was proposed to collapse the segregation and particle curtain spread rates with time. Further efforts are needed to extend

this scaling across wider particle diameter size ratios for comparison with experiments. All simulations reported herein were conducted in two dimensions. Three-dimensional results are expected to result in reduced segregation but the overall trends that were concluded in this paper should remain the same. Finally, it should be noted that this framework is ideally suited to handle heterogeneous reactions whereby finer particulates undergo combustion in the Euler–Lagrange framework while scalar fluxes induced by wakes of large particles are resolved.

Acknowledgments

A portion of this work was funded by Sandia National Laboratories, a multi-mission laboratory managed and operated by National Technology & Engineering Solutions of Sandia, LLC, a wholly owned subsidiary of Honeywell International Inc., for the U.S. Department of Energy's National Nuclear Security Administration under contract DE-NA0003525. This paper describes objective technical results and analysis. Any subjective views or opinions that might be expressed in the paper do not necessarily represent the views of the U.S. Department of Energy or the United States Government. We would also like to acknowledge partial funding of this project under SBIR Award No. HDTRA125P0006. The computing resources and assistance provided by the staff of the Advanced Research Computing at the University of Michigan, Ann Arbor are greatly appreciated.

CHAPTER 6

Conclusion and Future Work

Shock-particle interactions are observed in a variety of natural phenomenon and industrial applications. Some examples of these complex physics interactions are found in detonation blasts [43, 151], volcanic eruptions [12, 69], plume-surface interactions [14, 77, 98] and pulse-detonation engines. In some of these applications, these interactions have detrimental effects. Over the past few decades, significant progress has been made towards developing numerical models for disperse multiphase flows in incompressible flow regimes. Significantly less work has been done for compressible gas-particle flows that add an additional layer of complexity to pre-existing modeling challenges due to the wide range of length and time scales involved in these interactions.

Some of the challenges involved in simulating and modeling these flows deal with the presence of shock-waves, subsonic to supersonic velocities, compressibility, dilute to dense particle concentrations, shock-wake interactions at the microscale, local regions of turbulence and/instabilities within the flow field. Turbulence in multiphase flows is an important phenomenon at the microscale generated due to the presence of particles, as opposed to single-phase turbulence, where turbulence is generated at the large scales and cascades down to smaller Kolmogorov length scales.

This thesis is divided into two main parts. The first part introduces a comprehensive simulation framework for modeling the dynamics of moving bidisperse particles that have large differences in diameter. The second part investigates the phenomenon of pseudo-

turbulence—and elucidates the mechanisms responsible for its generation and dissipation. Although the primary focus is on a shock tube configuration, the findings related to pseudo-turbulence and particle size segregation can be extended to other multiphase compressible flows.

6.1 Summary of key findings and concluding remarks

A detailed summary of the key findings in each chapter follows:

1. **Chapter II**

   The numerical framework was detailed in this chapter. Key contributions include the following:

   (a) We proposed a coupled framework using volume-filtered Euler–Lagrange method and immersed boundary method to simulate bidisperse particle size-segregation with high size ratios.

   (b) Small particles were treated as Lagrangian particles and the large particle presence was enforced through immersed boundary methods.

   (c) An efficient algorithm was developed for detection of collision between small and large particles.

2. **Chapter III**

   To isolate the physics of shock–particle–turbulence interactions, three-dimensional high-fidelity simulations of a planar shock wave interacting with a suspension of particle were performed.

   (a) Local fluctuations within the gas-phase (pseudo-turbulence) were noted to be significant–about $25 - 50\%$ of the post-shock energy during these interactions.

(b) The effects of compressibility, i.e. increasing M_s, were observed to decrease the overall magnitude of streamwise and spanwise fluctuations, while the particle volume fraction had negligible effect except at the downstream curtain edge.

(c) A strong degree of anisotropy was observed across all cases, but the value for the anisotropy tensor was nearly constant through the curtain–$b_{11} = 0.2$ and $b_{22} = -0.1$ for all cases evaluated.

(d) A case with longer domain length downstream revealed that the translation of pseudo-turbulence downstream was analogous to the grid-generated turbulence decay with an exponent of -1.7.

(e) From the first-principles, a statistically one-dimensional transport equation for the pseudo-turbulent kinetic energy (PTKE) was derived. Key mechanisms of production were the mean shear and drag production terms, while viscous dissipation was noted to be the primary sink mechanism. Magnitude of all terms were noted to decrease with M_s due to compressibility effects, which was in alignment with single–phase turbulence literature.

(f) An energy spectrum analysis revealed an inertial-subrange with a scaling of $-5/3$ for the most part, while at higher wave numbers, it steepened to -3 due to particles. We also performed a Helmholtz decomposition and noted that the solenoidal component was modified by the dispersed phase while the dilatational component remained unaffected.

(g) A two-fluid turbulence model was proposed which showed very good agreement with the high-fidelity results.

3. **Chapter IV**

The framework developed in Chapter II is implemented on a shock-induced particle dispersal problem. The diameter size ratio between the large and the small particles is approximately 30.

(a) A three-dimensional simulation of bidisperse particles impacted by a shock was performed and revealed significant size segregation due to two mechanisms– hydrodynamic forces which enhanced segregation and interparticle collisions/wakes which inhibit segregation.

(b) One-dimensional statistics of particle volume fraction and PTKE revealed a pronounced and diffused spread of the small particles with time due to established drag across the curtain. The small particles undergo increased collisions with large particles at early instances of time, thereby reducing segregation, and this peak diffuses out with time.

(c) Mean forces of large particles were found to be higher than small. A closer look at the individual small particle forces reveal that force due to drag was the major contributor to acceleration while collisions at intermediate times were negative, reducing acceleration.

(d) A simple reduced order model was proposed for size segregation, dependent on particle diameter size ratios.

4. **Chapter V**:

A parametric study was performed for bidisperse particles by varying M_s, Φ_p, and D/d.

(a) The curtain spreads for large particles across all cases were noted to be minimal, small particles were found to have significant spreads.

(b) It was observed that M_s and Φ_p have the most significant effect on shock-induced size segregation.

(c) A scaling with volume fraction correction was proposed to collapse the segregation and particle curtain spread rates with time.

6.2 Future research directions

6.2.1 Reacting particles

The simulations of particle-dispersal due to interactions with shock waves revealed interesting insights into the effects of hydrodynamic forces of drag and turbulence (wakes) on particle segregation. One of the motivations to study bidisperse size segregation was to delineate the underlying physics of particle dispersal during detonation blasts. The natural next step is to incorporate reacting particles in our compressible multiphase flow solver, which is natural to do within the volume-filtered Euler–Lagrange framework.

The following review provides a path forward to simulate reacting flows relevant to the applications motivating this work. Dispersed aluminum in the gas is given as the sum of the mass of a single solid aluminum particle and the layer of alumina (Al_2O_3) formed on the particle surface [47, 48]. Aluminum undergoes oxidation through two different processes: oxidation at the particle surface (heterogeneous surface reaction) and a homogeneous reaction where Al and O_2 are in vapor form. Within our high-speed solver, `jCODE`, dispersed particles can be modeled within a Lagrangian framework (presented in Chapter 2) and interact with the gas-phase through source terms for mass, momentum and energy, according to

$$\frac{\partial \alpha\rho}{\partial t} + \nabla \cdot (\alpha\rho u) = S_m \tag{6.1}$$

$$\frac{\partial \alpha\rho u}{\partial t} + \nabla \cdot (\alpha\rho \boldsymbol{u} \otimes \boldsymbol{u}) = \alpha\nabla \cdot (\tau - p\mathcal{I}) + \mathcal{F} + S_{momentum} \tag{6.2}$$

$$\frac{\partial \alpha\rho E}{\partial t} + \nabla \cdot (\alpha\boldsymbol{u}(\rho E + p) - \alpha\boldsymbol{u}\tau) = \alpha\nabla \cdot q + (\tau - p\mathbb{I}) : \nabla(\alpha\boldsymbol{u}) + \boldsymbol{u} \cdot \boldsymbol{\mathcal{F}} + \boldsymbol{\mathcal{Q}} + S_{energy} \tag{6.3}$$

$$\frac{\partial \alpha\rho Y_l}{\partial t} + \nabla \cdot (\alpha\rho Y_l \boldsymbol{u}) = \dot{\omega}_l - \alpha\nabla \cdot (\rho D \nabla Y_l) + S_{species}, \tag{6.4}$$

where α specifies the voidage formed due to the Aluminum particles. ρ, $\boldsymbol{u}$, E are the density, velocity and energy of the gas-phase respectively. The equation of state is given by $\rho = P\bar{W}/(R_u T)$. p is the thermodynamic pressure, $R_u = 8.314$J/mol/K and the mixture

molecular weight is $1/\bar{W} = \sum_{k=1}^{N} Y_k/W_k$. $\boldsymbol{\mathcal{F}}$ and $\boldsymbol{\mathcal{Q}}$ are the interphase drag exchange and heat exchange terms. $\boldsymbol{u}_p$ is the particle velocity. S_m, $S_{momentum}$,S_{energy} are the source terms due to reactions. Y_l represents the species under consideration. $\mathcal{D}$ is the diffusivity determined by maintaining a constant Schmidt number $Sc = \upsilon/\mathcal{D} = 0.7$ and $\dot{\omega}$ is the reaction rate for species Y.

The aluminum particles are tracked according to

$$\frac{\mathrm{d}\boldsymbol{x}_p}{\mathrm{d}t} = \boldsymbol{u}_p, \tag{6.5}$$

$$m_p \frac{\mathrm{d}\boldsymbol{u}_p}{\mathrm{d}t} = \mathcal{V}_p \nabla \cdot (-p\mathbb{I} + \boldsymbol{\tau}) + \boldsymbol{f}_{drag} + \boldsymbol{f}_{col} \tag{6.6}$$

where x_p and u_p are the position and velocity of a particle. $\boldsymbol{f}_{drag}$ and $\boldsymbol{f}_{col}$ are the drag and collision forces. The evolution of particle temperature is governed by convection between the particle surface and surrounding gas and heat released due to the heterogeneous surface reaction:

$$m_p C_p \frac{\mathrm{d}T_p}{\mathrm{d}t} = \dot{q}_{conv} + \dot{q}_{HSR}. \tag{6.7}$$

q_{HSR} is modeled using an Arrhenius equation. Two distinct stages are defined: pre-ignition and combustion phases. In the pre-ignition stage, the relevant species for mass exchange from the dispersed phase back to the gas is due to formed alumina, and oxygen and solid Al being consumed. Post-ignition, heat exchange occurs due to convection and combustion. Empirical relations for the combustion model based on [47] will be used.

For the homogeneous reactions, the gas phase reaction of evaporated Al and oxygen is simulated by solving for the reaction kinetics. The reaction mechanism will consist of five reaction steps with seven species $Al, O_2, Al_2O_3, Al_2O_2, AlO, O, Al_2O$. The reaction rate is calculated as $k = A \times \exp(-E/RT)$. An assumption is made that gaseous Al_2O_3 does not exist because of the instant condensation. Liquid phase Al_2O_3 can be treated in a Eulerian solver, as it exists as a very fine smoke.

Work remains to extend the current framework to account for these reaction physics. Ad-

ditionally, the PTKE model developed in Chapter 3 can be implemented to the EL framework to account for reaction enhancement due to pseudo-turbulence.

6.2.2 Scalar flux modeling

Before studying turbulence in reacting flows, it is recommended to first consider passive scalars to isolate the effect of turbulence on scalar mixing. The first step to understanding these reacting flows, is to understand the transport of a passive scalar. A passive scalar is a scalar quantity such as temperature or the concentration of a chemical reagent that has negligible effect on the flow [148]. Equation 6.4 shows the phase-averaged transport of a scalar accounting for particle presence.

An ongoing task is to quantify the effects of passive scalar transport and leverage high-fidelity data to assess the importance of the scalar flux, which is an unclosed term that appears on phase-averaging the transport equation for a scalar quantity. Eq. 6.4 with no source term and interphase term is written as

$$\frac{\partial}{\partial t}(\alpha_g \bar{\rho} \widetilde{Y}) + \nabla \cdot (\alpha_g \bar{\rho} \widetilde{\boldsymbol{u}} \widetilde{Y}) + \nabla \cdot (\alpha_g \bar{\rho} \widetilde{\boldsymbol{u}'' Y''}) = \nabla \cdot (\alpha_g \mathcal{D} \widetilde{\nabla Y}), \tag{6.8}$$

$\mathcal{D}$ is the mass diffusivity for the scalar Y. The scalar flux or $\widetilde{\boldsymbol{u}'' Y''}$ that arises out of the averaging procedure requires modeling.

`jCODE` has been extended to account for general scalar transport of N species in the presence of immersed boundaries and Lagrangian particles. A modified version of the SBP dissipation detailed in Chapter 2 is used that reduces the local order of accuracy in grid points where the scalar field is unbounded such that the operator is diffusive and minimizes over/undershoots [61]. Figure 6.1 shows the simulation setup for evaluating the scalar flux. A planar shock impinging on a suspension of monodisperse stationary particles in a three-dimensional particle bed box is considered. $Y = 1$ in the post-shock conditions and $Y = 0$ in the pre-shock region. The shock wave has a Mach number of $M_s = 1.66$. A domain size

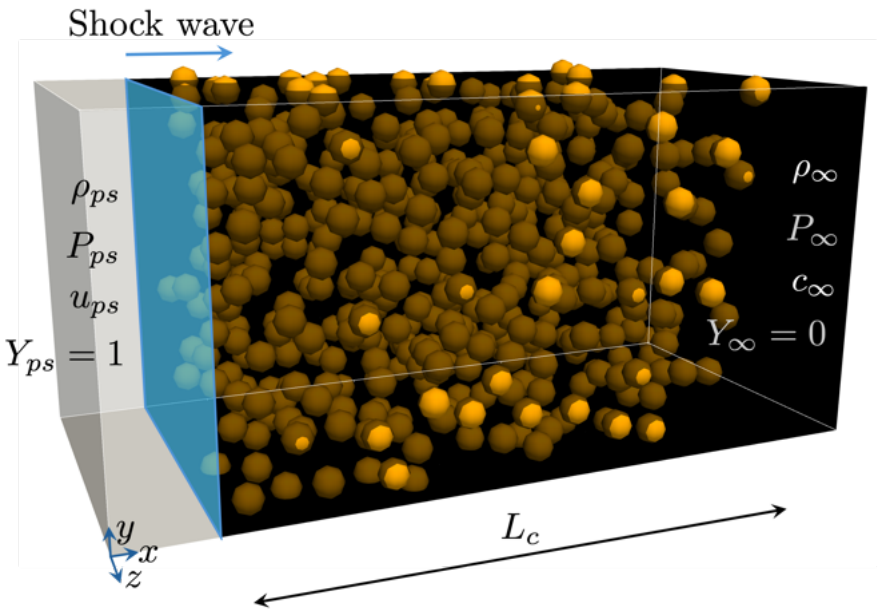

Figure 6.1: Schematic of the three-dimensional simulation setup showing the scalar field.

of $[25 \times 12 \times 12]$ D with a grid of $[1001 \times 480 \times 480]$ with particle sizes of $D = 115\mu$m in a suspension of length $L = 2$ mm is considered. Pre-shock conditions are taken to emulate Sandia's experimental setup, i.e. $[P_o,\ \rho_o] = [82.7\text{ kPa}, 0.98\text{ kg/m}^3]$. A Prandtl number of 0.7 is used.

Figure 6.2 shows the scalar flow field of a simulation conducted. This contour is presented at a late instant of time where the shock has passed the particle suspension and reached the downstream domain edge. The scalar field is initially 1 post-shock but as the flow progresses, significant scalar mixing occurs which leads to non-zero values throughout the suspension.

Figures 6.3(a) and (b) present mean scalar $\widetilde{Y}$ and scalar variance $\widetilde{Y''Y''}$ as a function of streamwise distance at different time instances. Scalar variance is initially high ($t/\tau_L = 0.5$) suggesting that it is mainly due to the mixing generated by the presence of particles but becomes diffusion controlled at later times. It is also non-zero outside of the suspension due to the transport of the wakes generated by particles.

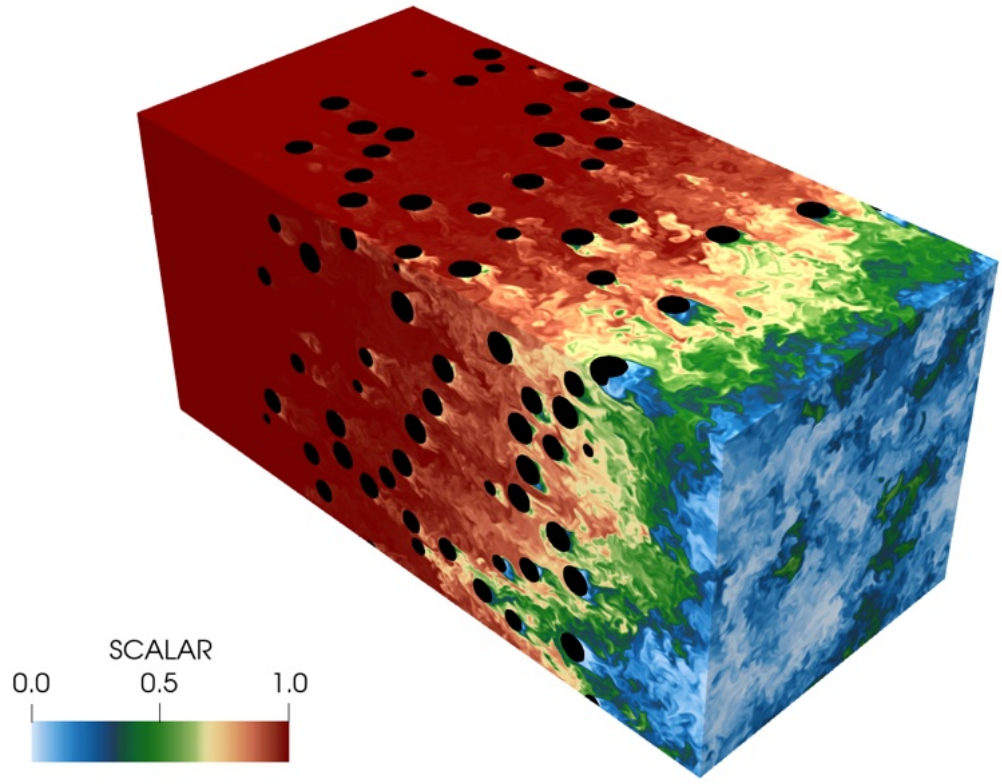

Figure 6.2: Contour of the scalar field at $t \gg 0$.

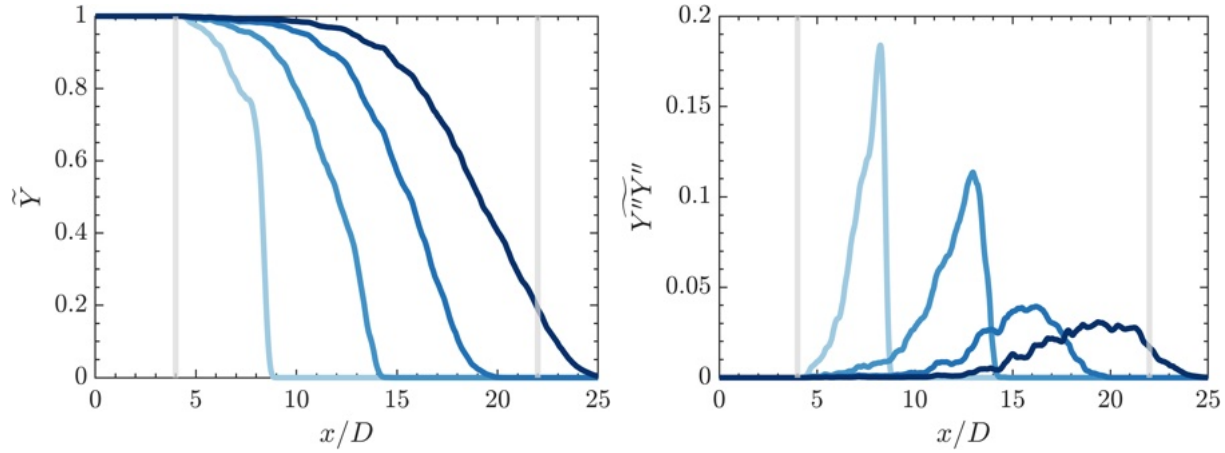

Figure 6.3: One-dimensional statistics of (a) Mean scalar quantity and (b) Mean scalar variance at times $t/\tau_L = 0.5$, 1, 1.5, and 2 (from light to dark) for $M_s = 1.66$, and $\Phi_p = 0.1$. Light gray vertical lines represent edges of the particle suspension.

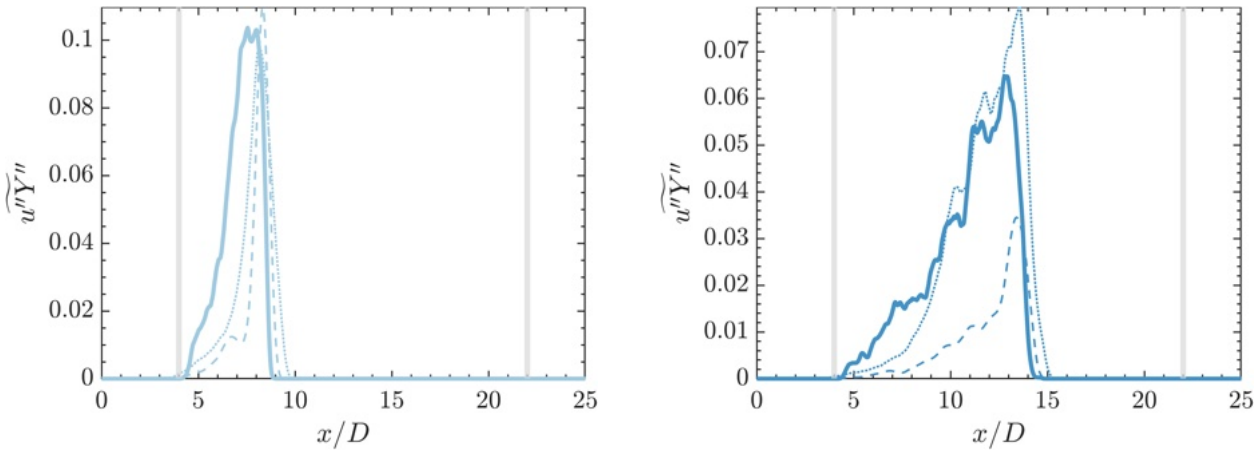

(a) $t/\tau_L = 0.5$

(b) $t/\tau_L = 1$

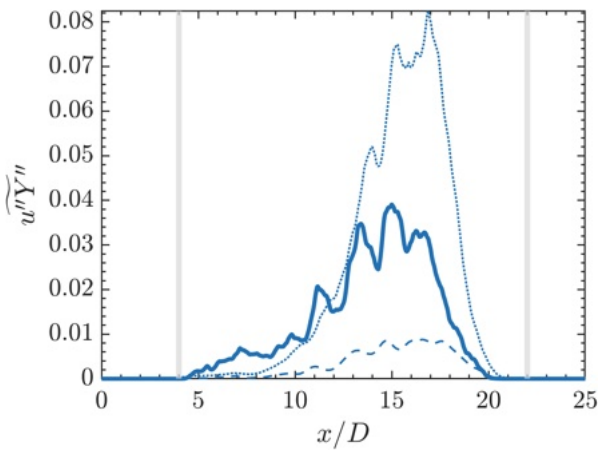

(c) $t/\tau_L = 1.5$

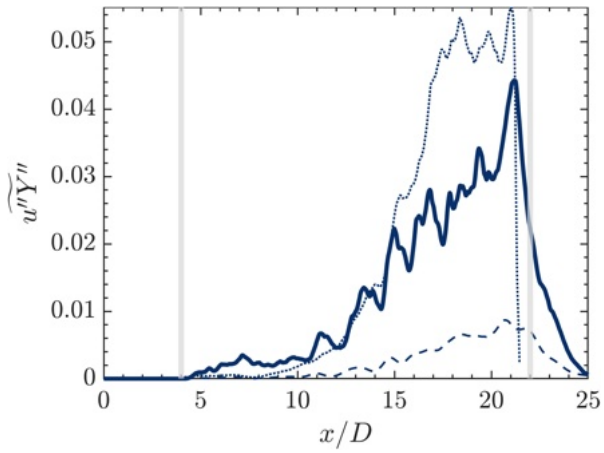

(d) $t/\tau_L = 2$

Figure 6.4: A comparison of the scalar flux component obtained from Model 1 (dashed) and Model 2 (dotted) against PR-DNS data (solid lines) at four different times.

6.2.2.1 Model 1: Boussinesq model from single-phase theory

A common modeling approach is to make a gradient diffusion approximation, i.e., $\widetilde{\boldsymbol{u}''Y_k''} = -\mathcal{D}_t \nabla Y_k$, where the turbulent diffusivity is given by $\mathcal{D}_t = \mu_t/(\rho Sc_t)$ where the turbulent Schmidt number $Sc_t \approx 1$ and the turbulent viscosity can be deduced from the multiphase $k-\epsilon$ model we recently developed, via $\mu_t = \rho C_\mu k^2/\epsilon$, where $C_\mu = 0.09$. This is what is typically done for singe phase flow and it is not obvious if such an approach will hold for gas-solid turbulent flows.

At this time of reporting, we have considered the value of k and ϵ to be the true values from the particle-resolved direct numerical simulations (PR-DNS) to evaluate the model's accuracy. Figure 6.4 shows the one-dimensional stats of the scalar flux from this model in dashed curves compared against the results from PR-DNS (solid lines). Although this model underpredicts scalar flux significantly, the overall trend is well captured and works well downstream of the suspension where particle volume fraction $\alpha_p \to 0$.

6.2.2.2 Model 2: Pseudo-turbulent diffusivity tensor

We employ a similar approach as Peng et al. [99] for the scalar flux $\widetilde{\boldsymbol{u}''Y_k''} = -\boldsymbol{\mathcal{D}}_{PT} \cdot \nabla\, Y_k$ where unlike a constant for diffusivity (like model 1), $\boldsymbol{\mathcal{D}}_{PT}$ is a pseudo-turbulent diffusivity tensor $\boldsymbol{\mathcal{D}}_{PT} = \mathrm{diag}(\mathcal{D}_{\parallel,\parallel}, \mathcal{D}_{\perp,\perp}, \mathcal{D}_{\perp,\perp})$ which essentially aligns with the slip velocity direction. The parallel component is computed as,

$$\frac{\mathcal{D}_{\parallel,\parallel}}{\alpha} = \frac{1.4Re_p(Re_p+1.4)Pr[\alpha(-5.11\alpha_p+10.1\alpha_p^2)+1-\exp(-10.96\alpha_p)]\exp(-0.002089Re_p)}{3\pi\alpha_p^2 Nu(1.17\alpha_p - 0.2021\alpha_p^{1/2} + 0.08568\alpha_p^{1/4})[1-1.6\alpha_p\alpha - 3\alpha_p\alpha^4\exp(-Re_p^{0.4}\alpha_p)]}, \tag{6.9}$$

and the perpendicular component is,

$$\mathcal{D}_{\perp,\perp} = \left(\frac{3b_{\perp,\perp}+1}{3b_{\parallel,\parallel}+1}\right)\mathcal{D}_{\parallel,\parallel}. \tag{6.10}$$

The correlations for Nusselt number and $\boldsymbol{\mathcal{D}}_{\mathbf{PT}}$ are the same as [131]. We obtained the

values for local α_g, Re_p and κ using the PR-DNS statistics. The results for this model are presented in Fig. 6.4 in dotted lines. At initial times (Fig. 6.4a and 6.4a), we note good agreement with the PR-DNS statistics. However, the diffusion of the scalar flux with time (6.4c, 6.4c) is not well captured by this model. It appears that the model nearly overpredicts the scalar flux by at least twice the PR-DNS amount. Also, this model essentially fails to capture the scalar flux downstream of the curtain where α_p is non-zero. These two models could potentially be combined using a blending function to capture the scalar flux within and outside of the particle suspension.

We have ongoing work that evaluates the effects of different parameters of M_s, Φ_p, and Sc on the scalar flux. The logical next step would be to propose scaling laws for the mean scalar quantity to collapse the spread shown in Fig. 6.3a that are valid across the parameter range considered. An analytical solution to a step function is of the form,

$$\widetilde{Y} = (1 + \mathrm{erf}(x/\sqrt{4\mathcal{D}t})/2. \tag{6.11}$$

If the mean scalar at $t = 0$ is considered to be a step function (with $Y = 1(x < x_s)$ and $Y = 0(x > x_s)$), it can be hypothesized that it advects at post-shock velocities and diffuses according to the diffusion coefficient, and a similarity variable $\bar{\xi}$ can be proposed to achieve a collapse as,

$$\xi = \frac{x - u_{ps}t}{\sqrt{\mathcal{D}_t t}} \quad \text{or} \quad \frac{x - u_{ps}t}{\sqrt{\boldsymbol{\mathcal{D}}_{PT} t}} \tag{6.12}$$

This collapse needs to be evaluated with an accurate model for $\mathcal{D}$. A particle volume fraction correction based on [95] can also be included to account for volume fraction correction.

Additionally, developing a precise scalar transport model for species would allow for more accurate simulation of reactant transport and potential reignition within the particle cloud. This advancement would make it possible to model reacting conditions in future detonation simulations with Aluminium particles.

6.3 Concluding remarks

This work was motivated by the need to understand and expand on the limited existing work on the microscale physics in multiphase compressible flows, relevant to the applications of detonation blasts, volcanic eruptions, PSIs, etc. Turbulence is a key phenomenon in this context which had previously received less attention as compared to single-phase incompressible and compressible and multiphase incompressible flows. To reiterate, interactions between shocks, turbulence and particles present challenges in understanding and modeling these complex flows.

This thesis intended to bridge this gap by leveraging large-scale, high-fidelity simulations of particle-laden shock tubes. New insights into the effects of compressibility on turbulence and the distribution of energy across scales were obtained. Further experimental efforts using shock tube facilities at Sandia National Laboratories can be used in conjunction with our numerical studies to validate the scalings in energy spectrum we note in our results. A supplementary study varying M_s and Φ_p conducted with longer domain lengths downstream of the particle suspension (similar to Case 10 from Chapter 3), revealed that at very late times, instead of an expected PTKE decay, the interstitial spaces between particles at the downstream curtain edge behaved like underexpanded nozzles. This resulted in the formation of a series of Mach diamonds (see Fig. 6.5) which coalesced into a secondary shock wave traveling downstream (seen in the figure). This is an extremely interesting physical phenomenon, which has not previously been noted or observed in shock-particle studies and warrants further investigation. Recent advances in computing power and resources facilitate these simulations as they require longer run times. Investigating magnitudes of PTKE, pressure and energy exchange mechanisms in these conditions presents an exciting path forward for this work.

This work also proposes a novel two-equation transport model for turbulence and dissipation with the potential for application in coarse-grained Euler–Euler and Euler–Lagrange frameworks for multiphase compressible flow problems in general. The model has currently

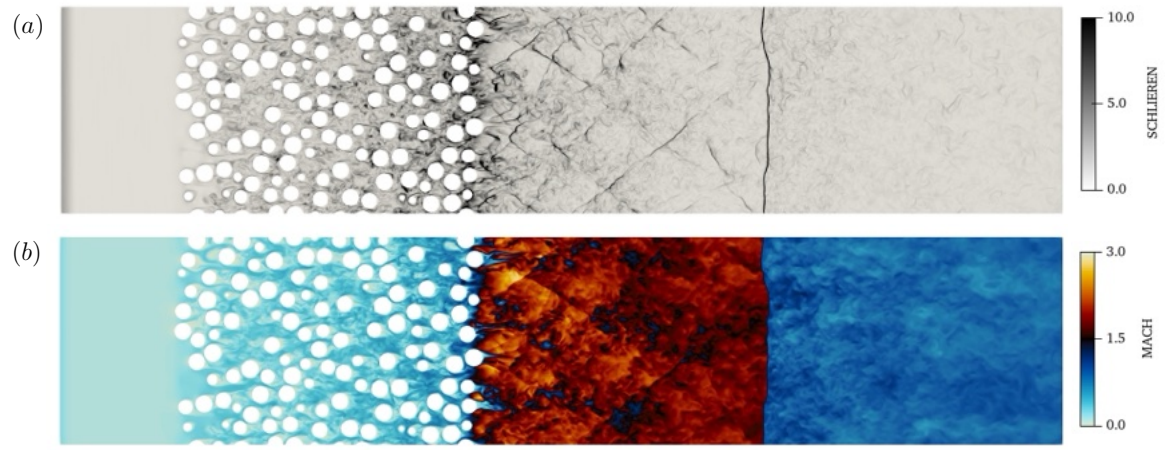

Figure 6.5: $2D$ Contour of (a) Numerical schlieren and (b) Local Mach number for $M_s = 2.1$ and $\Phi_p = 0.3$.

been evaluated for a range of M_s and Φ_p, which can potentially be expanded and tested for a wider range of parameters. Although we have evaluated the effect of Φ_p on turbulence and anisotropy within the curtain, the effects of volume fraction gradients at curtain edges remains to be quantified. A functional form for anisotropy, including these gradient effects can be part of future work.

Detonation conditions involve polydisperse particles with disparate sizes. A new framework that captures shock-induced size segregation of bidisperse flows (a fundamental polydisperse configuration) involving high size ratios was developed. Although the simulation results using this framework provide a high-fidelity baseline for validation of coarse-grained models, there is ground for validation with experimental efforts at Sandia. Additionally, the PTKE model developed in Chapter 3 remains to be implemented in this bidisperse framework for capturing PTKE of small particles.

Finally, shock-tube studies [55, 85] also note shock-driven multiphase instabilities (SDMIs) when certain conditions are satisfied, such as shock impinginement on radially (non-planar) distributed particle configurations or using a perturbed shock wave. The effect of subgrid-scale turbulence on particle dispersion and instabilities could be an interesting follow-up study.

BIBLIOGRAPHY

[1] G. Akiki, W. C. Moore, and S. Balachandar. Pairwise-interaction extended point-particle model for particle-laden flows. *J. Comput. Phys.*, 351:329–357, 2017.

[2] M. Anderson, P. Vorobieff, C. R. Truman, C. Corbin, G. Kuehner, P. Wayne, J. Conroy, R. White, and S. Kumar. An experimental and numerical study of shock interaction with a gas column seeded with droplets. *Shock Waves*, 25(2):107–125, 2015.

[3] B. J. Andrews. Dispersal and air entrainment in unconfined dilute pyroclastic density currents. *Bull. Volcanol.*, 76(9):852, 2014.

[4] S. Balachandar and J. K. Eaton. Turbulent dispersed multiphase flow. *Annu. Rev. Fluid Mech.*, 42(1):111–133, 2010.

[5] G. K. Batchelor. Small-scale variation of convected quantities like temperature in turbulent fluid part 1. general discussion and the case of small conductivity. *J. Fluid Mech.*, 5(1):113–133, 1959.

[6] G. K. Batchelor and A. A. Townsend. Decay of isotropic turbulence in the initial period. *Proc. R. Soc. Lond. A: Math. Phys. Eng. Sci.*, 193(1035):539–558, 1948.

[7] R. Beetstra, M. A. van der Hoef, and J. A. M. Kuipers. Drag force of intermediate Reynolds number flow past mono-and bidisperse arrays of spheres. *AIChE J.*, 53(2), 2007.

[8] M. C. Benage, J. Dufek, and P. A. Mothes. Quantifying entrainment in pyroclastic density currents from the tungurahua eruption, ecuador: Integrating field proxies with numerical simulations. *Geophys. Res. Lett.*, 43(13):6932–6941, 2016.

[9] V. Boniou and R. O. Fox. Shock–particle-curtain-interaction study with a hyperbolic two-fluid model: Effect of particle force models. *Int. J. Multiph. Flow*, 169:104591, 2023.

[10] P. Bradshaw. Compressible turbulent shear layers. *Annu. Rev. Fluid Mech.*, 9:33–52, 1977.

[11] E. C. P. Breard, J. Dufek, and G. Lube. Enhanced mobility in concentrated pyroclastic density currents: An examination of a self-fluidization mechanism. *Geophy. Res. Lett.*, 45(2):654–664, 2018.

[12] E. C. P. Breard, G. Lube, J. R. Jones, J. Dufek, S. J. Cronin, G. A. Valentine, and A. Moebis. Coupling of turbulent and non-turbulent flow regimes within pyroclastic density currents. *Nat. Geosci.*, 9(10):767–771, 2016.

[13] G. L. Brown and A. Roshko. On density effects and large structure in turbulent mixing layers. *J. Fluid Mech.*, 64(4):775–816, 1974.

[14] J. Capecelatro. Modeling high-speed gas–particle flows relevant to spacecraft landings. *Int. J. Multiph. Flow*, 150:104008, 2022.

[15] J. Capecelatro. High-order multiphase/multi-physics flow solver. jCODE, 2023.

[16] J. Capecelatro and O. Desjardins. An euler–lagrange strategy for simulating particle-laden flows. *J. Comput. Phys.*, 238:1–31, 2013.

[17] J. Capecelatro, O. Desjardins, and R. O. Fox. On the transition between turbulence regimes in particle-laden channel flows. *J. Fluid Mech.*, 845:499–519, 2018.

[18] J. Capecelatro and J. L. Wagner. Gas–particle dynamics in high-speed flows. *Annu. Rev. Fluid Mech.*, 56(1):379–403, 2024.

[19] Mark H Carpenter, David Gottlieb, and Saul Abarbanel. Time-stable boundary conditions for finite-difference schemes solving hyperbolic systems: methodology and application to high-order compact schemes. *J. Comput. Phys.*, 111(2):220–236, 1994.

[20] E. J. Chang and K. Kailasanath. Shock wave interactions with particles and liquid fuel droplets. *Shock Waves*, 12:333–341, 2003.

[21] A. Chaudhuri, A. Hadjadj, and A. Chinnayya. On the use of immersed boundary methods for shock/obstacle interactions. *J. Comput. Phys.*, 230(5):1731–1748, 2011.

[22] Z. Cheng and A. Wachs. Hydrodynamic force and torque fluctuations in a random array of polydisperse stationary spheres. *Int. J. Multiphase Flow*, 167, October 2023.

[23] K. Chojnicki, A. B. Clarke, and J. C. Phillips. A shock-tube investigation of the dynamics of gas-particle mixtures: Implications for explosive volcanic eruptions. *Geophys. Res. Lett.*, 33(15), 2006.

[24] D. K. Clarke, M. D. Salas, and H. A. Hassan. Euler calculations for multielement airfoils using cartesian grids. *AIAA J.*, 24(3), 1986.

[25] A. W. Cook and W. H. Cabot. A high-wavenumber viscosity for high-resolution numerical methods. *J. Comput. Phys.*, 195(2), 2004.

[26] C. T. Crowe, T. R. Troutt, and J. N. Chung. Numerical models for two-phase turbulent flows. *Annu. Rev. Fluid Mech.*, (28):11–43, 1996.

[27] P. A. Cundall and O. D. L. Strack. A discrete numerical model for granular assemblies. *Géotechnique*, 29(1), 1979.

[28] K. A. Daniel and J. L. Wagner. The shock-induced dispersal of particle curtains with varying material density. *Int. J. Multiph. Flow*, 152:104082, 2022.

[29] E. P. DeMauro, J. L. Wagner, L. J. DeChant, S. J. Beresh, and A. M. Turpin. Improved scaling laws for the shock-induced dispersal of a dense particle curtain. *J. Fluid Mech.*, 876:881–895, 2019.

[30] D. A. Donzis and S. Jagannathan. Fluctuations of thermodynamic variables in stationary compressible turbulence. *J. Fluid Mech.*, 733:221–244, oct 2013.

[31] D. A. Donzis and J. P. John. Universality and scaling in homogeneous compressible turbulence. *Phys. Rev. Fluids*, 5(8):084609, August 2020.

[32] F. Duan, Y. Yu, X. Chen, and Q. Zhou. Particle–particle drag force in inertial bidisperse gas–particle suspensions. *J. of Fluid Mech.*, 952, 2022.

[33] F. Ducros, V. Ferrand, F. Nicoud, C. Weber, D. Darracq, C. Gacherieu, and T. Poinsot. Large-eddy simulation of the shock/turbulence interaction. *J. Comput. Phys.*, 152(2):517–549, 1999.

[34] J. Dufek. The fluid mechanics of pyroclastic density currents. *Annu. Rev. Fluid Mech.*, 48(1):459–485, 2016.

[35] J. Dufek and G. W. Bergantz. Suspended load and bed-load transport of particle-laden gravity currents: the role of particle–bed interaction. *Theor. Comput. Fluid Dyn.*, 21(2):119–145, 2007.

[36] S. Elghobashi. Particle-laden turbulent flows: direct simulation and closure models. *Appl. Sci. Res.*, 48(3):301–314, 1991.

[37] S. Elghobashi. On predicting particle-laden turbulent flows. *Appl. Sci. Res.*, 52(4):309–329, 1994.

[38] S. E. Elghobashi and T. W. Abou-Arab. A two-equation turbulence model for two-phase flows. *Phys. Fluids*, 26(4):931–938, 04 1983.

[39] R. O. Fox. On multiphase turbulence models for collisional fluid–particle flows. *J. Fluid Mech.*, 742:368–424, 2014.

[40] R. O. Fox. A kinetic-based hyperbolic two-fluid model for binary hard-sphere mixtures. *J. Fluid Mech.*, 877:282–329, 2019.

[41] R. O. Fox, F. Laurent, and A. Vié. A hyperbolic two-fluid model for compressible flows with arbitrary material-density ratios. *J. Fluid Mech.*, 903:A5, 2020.

[42] J. B. Freund. Proposed inflow/outflow boundary condition for direct computation of aerodynamic sound. *AIAA J.*, 35(4):740–742, 1997.

[43] D. L. Frost. Heterogeneous/particle-laden blast waves. *Shock Waves*, 28(3):439–449, 2018.

[44] D. L. Frost, Y. Grégoire, O. Petel, S. Goroshin, and F. Zhang. Particle jet formation during explosive dispersal of solid particles. *Phys. Fluids*, 24(9), 2012.

[45] D. L. Frost, C. Ornthanalai, Z. Zarei, V. Tanguay, and F. Zhang. Particle momentum effects from the detonation of heterogeneous explosives. *J. Appl. Phys.*, 101(11), 2007.

[46] D. J. Gunn. Transfer of heat or mass to particles in fixed and fluidised beds. *Int. J. Heat Mass Transf.*, 21(4), 1978.

[47] D. H. Han, J. S. Shin, and H. G. Sung. A detailed flame structure and burning velocity analysis of aluminum dust cloud combustion using the eulerian–lagrangian method. *Proc. Combust. Inst.*, 36(2):2299–2307, 2017.

[48] D. H. Han and H. G. Sung. A numerical study on heterogeneous aluminum dust combustion including particle surface and gas-phase reaction. *Combust. Flame*, 206:112–122, 2019.

[49] T. R. Hendrickson, A. Kartha, and G. V. Candler. An improved Ducros sensor for the simulation of compressible flows with shocks. In *2018 Fluid Dyn. Conf.*, page 3710, 2018.

[50] Z. Hosseinzadeh-Nik, S. Subramaniam, and J. D. Regele. Investigation and quantification of flow unsteadiness in shock-particle cloud interaction. *Int. J. Multiph. Flow*, 101:186–201, April 2018.

[51] Z. Hou, D. Wang, Y. Zhu, S. Luo, Q. Zhong, Z. Liu, Y. Lu, and Y. Zhang. Experimental study on pressure wave-induced explosion of different types of deposited coal dust. *Process Saf. Environ. Prot*, 172:825–835, 2023.

[52] R. W. Houim and E. S. Oran. A multiphase model for compressible granular–gaseous flows: formulation and initial tests. *J. Fluid Mech.*, 789:166–220, 2016.

[53] X. Y. Hu, B. C. Khoo, N. A. Adams, and F. L. Huang. A conservative interface method for compressible flows. *J. of Comput. Phys.*, 219(2), 2006.

[54] T. Inoue, R. Yamazaki, and Shu-ichiro Inutsuka. Turbulence and magnetic field amplification in supernova remnants: interactions between a strong shock wave and multiphase interstellar medium. *Astrophys. J.*, 695(2):825, 2009.

[55] R. G. Izard, S. R. Lingampally, P. Wayne, G. Jacobs, and P. Vorobieff. Instabilities in a shock interaction with a perturbed curtain of particles. *Multiph. Flow: Theo. Appl.*, 6(1):59–70, 2018.

[56] S. Jagannathan and D. A. Donzis. Reynolds and Mach number scaling in solenoidally-forced compressible turbulence using high-resolution direct numerical simulations. *J. Fluid Mech.*, 789:669–707, February 2016.

[57] S. Kawai, S. K. Shankar, and S. K. Lele. Assessment of localized artificial diffusivity scheme for large-eddy simulation of compressible turbulent flows. *J. Comput. Phys.*, 229(5):1739–1762, 2010.

[58] M. Khalloufi and J. Capecelatro. Drag force of compressible flows past random arrays of spheres. *Int. J. Multiph. Flow*, 165:104496, 2023.

[59] S. Kida and S. A. Orszag. Energy and spectral dynamics in forced compressible turbulence. *J. Sci. Comput.*, 5(2):85–125, June 1990.

[60] A. N. Kolmogorov. The local structure of turbulence in incompressible viscous fluid for very large Reynolds numbers. *Dokl. Akad. Nauk SSSR*, 30:299–303, 1941b.

[61] Ali Kord and Jesse Capecelatro. Adaptive energy stable artificial dissipation for preserving scalar boundedness in turbulent flows. *Comput. Fluids*, 254:105776, 2023.

[62] T. Kurian and J. H. M. Fransson. Grid-generated turbulence revisited. *Fluid Dyn. Res.*, 41(2):021403, 2009.

[63] M. Lance and J. Bataille. Turbulence in the liquid phase of a uniform bubbly air–water flow. *J. Fluid Mech.*, 222:95–118, 1991.

[64] A. M. Lattanzi, V. Tavanashad, S. Subramaniam, and J. Capecelatro. Stochastic model for the hydrodynamic force in Euler–Lagrange simulations of particle-laden flows. *Phys. Rev. Fluids*, 7(1):014301, 2022.

[65] S. K. Lele. Compact finite difference schemes with spectral-like resolution. *J. Comput. Phys.*, 103(1):16–42, 1992.

[66] S. K. Lele. Compressibility effects on turbulence. *Annu. Rev. Fluid Mech.*, 26(1):211–254, 1994.

[67] Y. Ling, A. Haselbacher, and S. Balachandar. Importance of unsteady contributions to force and heating for particles in compressible flows: Part 1: Modeling and analysis for shock–particle interaction. *Int. J. Multi. Flow*, 37(9):1026–1044, 2011.

[68] Y. Ling, J. L. Wagner, S. J. Beresh, S. P. Kearney, and S. Balachandar. Interaction of a planar shock wave with a dense particle curtain: Modeling and experiments. *Phys. Fluids*, 24(11), 2012.

[69] G. Lube, E. C. P. Breard, T. Esposti-Ongaro, J. Dufek, and B. Brand. Multiphase flow behaviour and hazard prediction of pyroclastic density currents. *Nat. Rev. Earth Environ.*, 1(7):348–365, 2020.

[70] D. Ma and G. Ahmadi. A thermodynamical formulation for dispersed multiphase turbulent flows—II: Simple shear flows for dense mixtures. *Int. J. Multiph. Flow*, 16(2):341–351, 1990.

[71] T. Ma, C. Santarelli, T. Ziegenhein, D. Lucas, and J. Fröhlich. Direct numerical simulation–based Reynolds-averaged closure for bubble-induced turbulence. *Phys. Rev. Fluids*, 2(3):034301, March 2017.

[72] K. Mattsson, M. Svärd, and J. Nordström. Stable and accurate artificial dissipation. *J. Sci. Comput.*, 21:57–79, 2004.

[73] J. A. McFarland, W. J. Black, J. Dahal, and B. E. Morgan. Computational study of the shock driven instability of a multiphase particle-gas system. *Phys. Fluids*, 28(2), 2016.

[74] M. Mehrabadi and S. Subramaniam. Mechanism of kinetic energy transfer in homogeneous bidisperse gas-solid flow and its implications for segregation. *Phys. Fluids*, 29(2), 2017.

[75] M. Mehrabadi, S. Tenneti, R. Garg, and S. Subramaniam. Pseudo-turbulent gas-phase velocity fluctuations in homogeneous gas–solid flow: fixed particle assemblies and freely evolving suspensions. *J. Fluid Mech.*, 770:210–246, 2015.

[76] M. Mehrabadi, S. Tenneti, and S. Subramaniam. Importance of the fluid-particle drag model in predicting segregation in bidisperse gas-solid flow. *Int. J. Multiphase Flow*, 86, 2016.

[77] M. Mehta, A. Sengupta, N. O. Renno, J. W. V. Norman, P. G. Huseman, D. S. Gulick, and M. Pokora. Thruster plume surface interactions: Applications for spacecraft landings on planetary bodies. *AIAA J.*, 51(12):2800–2818, 2013.

[78] Y. Mehta, R. J. Goetsch, O. V. Vasilyev, and J. D. Regele. A particle resolved simulation approach for studying shock interactions with moving, colliding solid particles. *Comput. Fluids*, 248, 2022.

[79] Y. Mehta, T. L. Jackson, and S. Balachandar. Pseudo-turbulence in inviscid simulations of shock interacting with a bed of randomly distributed particles. *Shock Waves*, 30:49–62, 2020.

[80] Y. Mehta, C. Neal, K. Salari, T. L. Jackson, S. Balachandar, and S. Thakur. Propagation of a strong shock over a random bed of spherical particles. *J. Fluid Mech.*, 839:157–197, 2018.

[81] Y. Mehta, K. Salari, T. L. Jackson, and S. Balachandar. Effect of mach number and volume fraction in air-shock interacting with a bed of randomly distributed spherical particles. *Phys. Rev. Fluids*, 4(1):014303, 2019.

[82] J. M. Mercado, D. C. Gomez, D. Van Gils, C. Sun, and D. Lohse. On bubble clustering and energy spectra in pseudo-turbulence. *J. Fluid Mech.*, 650:287–306, 2010.

[83] Y. Mezui, A. Cartellier, and M. Obligado. An experimental study on the liquid phase properties of a bubble column operated in the homogeneous and in the heterogeneous regimes. *Chem. Eng. Sci.*, 268:118381, 2023.

[84] Y. Mezui, M. Obligado, and A. Cartellier. Buoyancy-driven bubbly flows: scaling of velocities in bubble columns operated in the heterogeneous regime. *J. Fluid Mech.*, 952:A10, 2022.

[85] John B Middlebrooks, Constantine G Avgoustopoulos, Wolfgang J Black, Roy C Allen, and Jacob A McFarland. Droplet and multiphase effects in a shock-driven hydrodynamic instability with reshock. *Exp. Fluids*, 59:1–16, 2018.

[86] A. R. Miles. The blast-wave-driven instability as a vehicle for understanding supernova explosion structure. *Astrophys. J.*, 696(1):498, 2009.

[87] M. S. Mohamed and J. C. Larue. The decay power law in grid-generated turbulence. *J. Fluid Mech.*, 219:195–214, 1990.

[88] J. Mohd-Yusof. Combined immersed-boundary/B-spline methods for simulations of flow in complex geometries. *NASA Annu. Res. Briefs*, 161(1):317–327, 1997.

[89] A. B. Morris. *Simulation of rocket plume impingement and dust dispersal on the lunar surface*. PhD thesis, University of Texas, 2012.

[90] A. B. Morris, D. B. Goldstein, P. L. Varghese, and L. M. Trafton. Plume impingement on a dusty lunar surface. In *AIP Conference Proceedings*, volume 1333, pages 1187–1192, 2011.

[91] A. Neri and G. Macedonio. Numerical simulation of collapsing volcanic columns with particles of two sizes. *J. Geophys. Res.: Solid Earth*, 101(B4):8153–8174, 1996.

[92] J. Nordström and M. Svärd. Well-posed boundary conditions for the navier–stokes equations. *SIAM J. Numer. Anal.*, 43(3):1231–1255, 2005.

[93] A. N. Osnes and M. Vartdal. Performance of drag force models for shock-accelerated flow in dense particle suspensions. *Int. J. Multiph. Flow*, 137:103563, 2021.

[94] A. N. Osnes, M. Vartdal, M. Khalloufi, J. Capecelatro, and S. Balachandar. Comprehensive quasi-steady force correlations for compressible flow through random particle suspensions. *Int. J. Multiph. Flow*, 165:104485, 2023.

[95] A. N. Osnes, M. Vartdal, M. G. Omang, and B. A. P. Reif. Computational analysis of shock-induced flow through stationary particle clouds. *Int. J. Multiph. Flow*, 114:268–286, 2019.

[96] A. N. Osnes, M. Vartdal, M. G. Omang, and B. A. P. Reif. Particle-resolved simulations of shock-induced flow through particle clouds at different reynolds numbers. *Phys. Rev. Fluids*, 5(1):014305, 2020.

[97] C. Pantano and S. Sarkar. A study of compressibility effects in the high-speed turbulent shear layer using direct simulation. *J. Fluid Mech.*, 451:329–371, 2002.

[98] M. Patel, J. S. Rubio, D. Shekhtman, N. Parziale, J. Rabinovitch, R. Ni, and J. Capecelatro. Experimental and numerical investigation of inertial particles in underexpanded jets. *J. Fluid Mech.*, 1000:A60, 2024.

[99] C. Peng, B. Kong, J. Zhou, B. Sun, A. Passalacqua, S. Subramaniam, and R. O. Fox. Implementation of pseudo-turbulence closures in an eulerian–eulerian two-fluid model for non-isothermal gas–solid flow. *Chem. Eng. Sci.*, 207:663–671, 2019.

[100] P. Pepiot and O. Desjardins. Numerical analysis of the dynamics of two-and three-dimensional fluidized bed reactors using an euler–lagrange approach. *Powder Technol.*, 220:104–121, 2012.

[101] C. S. Peskin. Flow patterns around heart valves: a numerical method. *J. Comput. Phys.*, 10(2):252–271, 1972.

[102] S. Pirozzoli. Stabilized non-dissipative approximations of Euler equations in generalized curvilinear coordinates. *J. Comput. Phys.*, 230(8):2997–3014, 2011.

[103] D. H. Plemmons, M. Mehta, B. C. Clark, S. P. Kounaves, L. L. Peach, N. O. Renno, L. Tamppari, and S. M. M. Young. Effects of the Phoenix Lander descent thruster plume on the Martian surface. *J. Geophys. Res. Planets*, 114, 2009.

[104] S. B. Pope. *Turbulent Flows*. Cambridge University Press, 2000.

[105] J. D. Regele, J. Rabinovitch, T. Colonius, and G. Blanquart. Unsteady effects in dense, high speed, particle laden flows. *Int. J. Multiph. Flow*, 61:1–13, 2014.

[106] J. D. Regele, J. Rabinovitch, T. Colonius, and G. Blanquart. Unsteady effects in dense, high speed, particle laden flows. *Int. J. Multiph. Flow*, 61:1–13, 2014.

[107] Y. Ren, Y. Shen, P. Wang, and H. Ding. Simulation of interaction between shocks and particle cloud using a second-order conservative sharp interface method. *J. Comput. Phys.*, 439, 2021.

[108] O. Reynolds. Xxix. an experimental investigation of the circumstances which determine whether the motion of water shall be direct or sinuous, and of the law of resistance in parallel channels. *Philos. Trans. R. Soc. Lond*, (174):935–982, 1883.

[109] Osborne Reynolds. Iv. on the dynamical theory of incompressible viscous fluids and the determination of the criterion. *Philosophical transactions of the royal society of london.(a.)*, (186):123–164, 1895.

[110] L. F. Richardson. *Weather prediction by numerical process*. Franklin Classics, 1922.

[111] F. Risso. Agitation, Mixing, and Transfers Induced by Bubbles. *Annu. Rev. Fluid Mech.*, 50(1):25–48, 2018.

[112] X. Rogue, G. Rodriguez, J. F. Haas, and R. Saurel. Experimental and numerical investigation of the shock-induced fluidization of a particles bed. *Shock waves*, 8(1):29–45, 1998.

[113] G. D. Roy, S. M. Frolov, A. A. Borisov, and D. W. Netzer. Pulse detonation propulsion: challenges, current status, and future perspective. *Prog. Energy Combust. Sci.*, 30(6):545–672, 2004.

[114] P. Sagaut and C. Cambon. *Homogeneous turbulence dynamics*, volume 15. Springer, 2008.

[115] O. San and R. Maulik. Stratified Kelvin–Helmholtz turbulence of compressible shear flows. *Nonlinear Processes in Geophysics*, 25(2):457–476, June 2018.

[116] M. J. Sapko, E. S. Weiss, K. L. Cashdollar, and I. A. Zlochower. Experimental mine and laboratory dust explosion research at NIOSH. *J. of Loss Prev. Process Ind.*, 13(3-5), 2000.

[117] S. Sarkar. The stabilizing effect of compressibility in turbulent shear flow. *J. Fluid Mech.*, 282:163–186, January 1995.

[118] S. Sarkar, G. Erlebacher, M. Y. Hussaini, and H. O. Kreiss. The analysis and modelling of dilatational terms in compressible turbulence. *J. Fluid Mech.*, 227:473–493, 1991.

[119] S. Sarkar, S. H. L. Kriebitzsch, M. A. van der Hoef, and J. A. M. Kuipers. Gas–solid interaction force from direct numerical simulation (DNS) of binary systems with extreme diameter ratios. *Particuology*, 7(4), 2009.

[120] G. S. Shallcross and J. Capecelatro. An explicit characteristic-based immersed boundary method for compressible flows. *J. Comput. Phys.*, 449, 2022.

[121] G. S. Shallcross, R. O. Fox, and J. Capecelatro. A volume-filtered description of compressible particle-laden flows. *Int. J. Multiph. Flow*, 122:103138, 2020.

[122] O. Simonin. Continuum modelling of dispersed two-phase flows. *Lecture series-van Kareman Inst. fluid dyn.*, 2:K1–K47, 1996.

[123] M. Sommerfeld. The structure of particle-laden, underexpanded free jets. *Shock waves*, 3(4):299–311, 1994.

[124] M. Soo, S. Goroshin, J. M. Bergthorson, and D. L. Frost. Reaction of a particle suspension in a rapidly-heated oxidizing gas. *Propellants Explos. Pyrotech.*, 40(4):604–612, 2015.

[125] A. Sridhar and J. Capecelatro. High-fidelity modeling of shock-induced flow through a bidisperse particle mixture using an IBM/Euler-Lagrange framework. In *AIAA SCITECH 2025 Forum*, page 1878, 2025.

[126] A. Sridhar and J. Capecelatro. Shock-induced size segregation of bidisperse particles. *AIAA J.*, pages 1–9, 2025.

[127] A. Sridhar and J. Capecelatro. A coupled ibm/euler-lagrange framework for simulating shock-induced particle size segregation. *Acta Mech. Sin.*, 42(1):1–14, 2026.

[128] A. Sridhar, R. O. Fox, and J. Capecelatro. Turbulence transport in moderately dense gas–particle compressible flows. *arXiv preprint arXiv:2504.03061*, 2025.

[129] B. Strand. Summation by parts for finite difference approximations for d/dx. *J. Comput. Phys.*, 110, 1994.

[130] S. Subramaniam and S. Balachandar. *Modeling approaches and computational methods for particle-laden turbulent flows*. Academic Press, 2022.

[131] B. Sun, S. Tenneti, S. Subramaniam, and D. L. Koch. Pseudo-turbulent heat flux and average gas–phase conduction during gas–solid heat transfer: flow past random fixed particle assemblies. *J. Fluid Mech.*, 798:299–349, 2016.

[132] M. Svärd, M. H. Carpenter, and J. Nordström. A stable high-order finite difference scheme for the compressible Navier–Stokes equations, far-field boundary conditions. *J. Comput. Phys.*, 225(1):1020–1038, 2007.

[133] M. Svärd and J. Nordström. A stable high-order finite difference scheme for the compressible Navier–Stokes equations: no-slip wall boundary conditions. *J. Comput. Phys.*, 227(10):4805–4824, 2008.

[134] S. Tenneti and S. Subramaniam. Particle-resolved direct numerical simulation for gas-solid flow model development. *Annu. Rev. Fluid Mech.*, 46(1):199–230, 2014.

[135] T. G. Theofanous, V. Mitkin, and C. H. Chang. The dynamics of dense particle clouds subjected to shock waves. part 1. experiments and scaling laws. *J. Fluid Mech.*, 792:658–681, 2016.

[136] T. G. Theofanous, V. Mitkin, and C. H. Chang. Shock dispersal of dilute particle clouds. *J. Fluid Mech.*, 841:732–745, 2018.

[137] E. F. Toro, M. Spruce, and W. Speares. Restoration of the contact surface in the HLL-Riemann solver. *Shock Waves*, 4:25–34, 1994.

[138] A. A. Troshko and Y. A. Hassan. A two-equation turbulence model of turbulent bubbly flows. *Int. J. Multiph. Flow*, 27(11):1965–2000, 2001.

[139] H. S. Udaykumar, R. Mittal, P. Rampunggoon, and A. Khanna. A sharp interface cartesian grid method for simulating flows with complex moving boundaries. *J. Comput. Phys.*, 174(1):345–380, 2001.

[140] D. H. Uhle, G. Lube, E. C. P. Breard, E. Meiburg, J. Dufek, J. Ardo, J. R. Jones, E. Brosch, L. R. P. Corna, and S. F. Jenkins. Turbulent particle-gas feedback exacerbates the hazard impacts of pyroclastic density currents. *Comm. Earth Environ.*, 5(1):245, 2024.

[141] M. Vartdal and A. N. Osnes. Using particle-resolved LES to improve Eulerian-Lagrangian modeling of shock wave particle cloud interaction. In *Proceedings of the Summer Program*, pages 25–34, 2018.

[142] R. Vishnampet. *An exact and consistent adjoint method for high-fidelity discretization of the compressible flow equations*. PhD thesis, University of Illinois at Urbana-Champaign, 2015.

[143] A. W. Vreman, N. D. Sandham, and K. H. Luo. Compressible mixing layer growth rate and turbulence characteristics. *J. Fluid Mech.*, 320:235–258, 1996.

[144] J. L. Wagner, S. J. Beresh, S. P. Kearney, W. M. Trott, J. N. Castaneda, B. O. Pruett, and M. R. Baer. A multiphase shock tube for shock wave interactions with dense particle fields. *Exp. Fluids*, 52:1507–1517, 2012.

[145] J. L. Wagner, S. P. Kearney, S. J. Beresh, E. P. DeMauro, and B. O. Pruett. Flash x-ray measurements on the shock-induced dispersal of a dense particle curtain. *Exp. Fluids*, 56(12):213, 2015.

[146] J. Wang, Y. Shi, L. Wang, Z. Xiao, X. He, and S. Chen. Effect of shocklets on the velocity gradients in highly compressible isotropic turbulence. *Phys. Fluids*, 23(12), 2011.

[147] J. Wang, Y. Shi, L. Wang, Z. Xiao, X. T. He, and S. Chen. Effect of compressibility on the small-scale structures in isotropic turbulence. *J. Fluid Mech.*, 713:588–631, 2012.

[148] Z. Warhaft. Passive scalars in turbulent flows. *Annu. Rev. Fluid Mech.*, 32(1):203–240, 2000.

[149] M. Yu, C. Xu, and S. Pirozzoli. Genuine compressibility effects in wall-bounded turbulence. *Physical Review Fluids*, 4(12):123402, December 2019.

[150] O. Zeman. Dilatation dissipation: The concept and application in modeling compressible mixing layers. *Phys. Fluids*, 2(2):178–188, 1990.

[151] F. Zhang, D. L. Frost, P. A. Thibault, and S. B. Murray. Explosive dispersal of solid particles. *Shock Waves*, 10(6), 2001.

[152] Y. P. Zheng, C. G. Feng, G. X. Jing, X. M. Qian, X. J. Li, Z. Y. Liu, and P. Huang. A statistical analysis of coal mine accidents caused by coal dust explosions in China. *J. of Loss Prev. Process Ind.*, 22(4), 2009.